

**EXTRACTION OF PHYSICALLY-REALISTIC PORE NETWORK  
PROPERTIES FROM THREE-DIMENSIONAL SYNCHROTRON  
MICROTOMOGRAPHY IMAGES OF UNCONSOLIDATED POROUS MEDIA**

A Dissertation

Submitted to the Graduate Faculty of the  
Louisiana State University and  
Agricultural and Mechanical College  
in partial fulfillment of  
the requirement for the degree of  
Doctor of Philosophy

In

The Department of Civil and Environmental Engineering

By

Riyadh I. Al-Raoush

B.S., Jordan University of Science and Technology, Jordan, 1994

M.S., Jordan University of Science and Technology, Jordan, 1997

December, 2002

## **Dedication**

**To my parents**

## **Acknowledgments**

First, I thank God for giving me the ability to finish this work.

This research was motivated and strongly supported by my advisor Clinton S. Willson. His insight, encouragement, dedication, and great personality helped me throughout this research. I am greatly thankful for him.

Additional faculty who contributed to this research are Karsten E. Thompson, Christopher D. White, Leslie G. Butler, and Emir J. Macari I appreciate their fruitful discussions.

Two close friends provided me with unlimited support: Carla Willaims and Hammad Hussien. Their friendship is a great help.

I thank my parents, brothers, and sister for their love and support.

Financial support for this research was provided by the department of Civil and Environmental Engineering and Louisiana Board of Regents. This support is gratefully acknowledged.

# TABLE OF CONTENTS

<b>DEDICATION.....</b>	<b>ii</b>
<b>ACKNOWLEDGEMENTS.....</b>	<b>iii</b>
<b>LIST OF TABLES.....</b>	<b>vii</b>
<b>LIST OF FIGURES.....</b>	<b>viii</b>
<b>ABSTRACT.....</b>	<b>xii</b>
<b>1. INTRODUCTION.....</b>	<b>1</b>
<b>2. BACKGROUND AND LITERATURE REVIEW.....</b>	<b>6</b>
2.1 INTRODUCTION TO NETWORK MODELS.....	6
2.2 APPLICATION OF NETWORK MODELS.....	6
2.3 SINGLE AND MULTIPHASE FLOW PROPERTIES.....	7
2.3.1 Interfacial Tension and Wettability.....	7
2.3.2 Capillary Pressure.....	9
2.3.3 Drainage and Imbibition.....	10
2.3.4 Relative Permeability.....	14
2.3.5 Interfacial Area and Mass Transfer.....	14
2.4 DESCRIPTION OF THE PORE SPACE.....	15
2.5 INFLUENCE OF PORE-NETWORK PARAMETERS ON SINGLE- AND MULTI-PHASE PROPERTIES.....	18
2.5.1 Spatial Correlation.....	18
2.5.2 Connectivity.....	21
2.5.3 Pore-Body Size Distribution.....	21
2.6 OBTAINING PORE-NETWORK STRUCTURE FROM POROUS MEDIA SYSTEMS.....	22
2.6.1 Simulation of Random Close Packing of Porous Media.....	23
2.6.2 Three-Dimensional Reconstruction of the Pore Space Based on its Statistical Properties.....	23
2.7 METHODS TO OBTAIN PORE-NETWORK STRUCTURE FROM THREE-DIMENSIONAL IMAGES.....	25
2.7.1 Binary Representation of the Pore Space.....	25
2.7.2 Multiorientation Scanning Algorithm.....	26
2.7.3 Morphological Thinning Algorithm.....	26
2.7.4 Medial-Axis Skeletonization.....	27
2.7.5 Quantitative Morphology.....	27
2.8 APPLICATIONS OF IMAGING TECHNIQUES ON POROUS MEDIA SYSTEMS STUDIES.....	28
2.9 MICROTOMOGRAPHY.....	30

2.10	MOTIVATIONS AND OBJECTIVES OF THIS WORK .....	31
<b>3.</b>	<b>MATERIALS AND METHODOLOGY.....</b>	<b>33</b>
3.1	SYNCHROTRON MICROTOMOGRAPHY INSTRUMENT DESCRIPTION.....	33
3.2	PRE-PROCESSING AND DATA COLLECTION .....	34
3.3	DATA PROCESSING AND RECONSTRUCTION .....	36
3.3.1	Collection of the Raw Images .....	36
3.3.2	Correction for Dark and White Fields.....	37
3.3.3	Absorption.....	37
3.3.4	Creation of Sinograms.....	38
3.3.5	Centering the Sinogram.....	38
3.3.6	Vertical Streak(s) Removal .....	39
3.4	CROSS-SECTION RECONSTRUCTION USING THE FILTERED-BACK PROJECTION ALGORITHM .....	40
3.5	IMAGE PROCESSING.....	44
3.5.1	Scaling the Data .....	45
3.5.2	Filtering the Data.....	45
3.5.2.1	Mean Filter .....	46
3.5.2.2	Median Filter .....	47
3.6	IMAGE SEGMENTATION .....	47
3.7	POROSITY AND SPECIFIC SURFACE AREA .....	50
3.8	REPRESENTATIVE ELEMENTARY VOLUME (REV).....	53
3.9	EXTRACTION OF PHYSICALLY-REALISTIC PORE NETWORK STRUCTURE.....	54
3.9.1	Generating the Medial Axis .....	54
3.9.2	Inscribed Pore Radius Calculations.....	57
3.9.3	Inscribed Throat Radius Calculations .....	59
3.9.4	Connectivity of the Pore Space .....	60
3.9.5	Validation of the Algorithm.....	60
3.9.6	Pore Network Structure Correlation.....	62
3.9.6.1	Semivariograms.....	62
3.9.6.2	Integral Range .....	63
3.9.7	Materials and Data Sets.....	64
<b>4.</b>	<b>RESULTS AND DISCUSSION.....</b>	<b>66</b>
4.1	TWO-DIMENSIONAL AND THREE-DIMENSIONAL IMAGES OF THE EXPERIMENTS ....	66
4.2	TWO-POINT CORRELATION FUNCTION (POROSITY AND SPECIFIC SURFACE AREA) .....	70
4.3	REPRESENTATIVE ELEMENTARY VOLUME ANALYSIS (REV).....	76
4.4	EXTRACTION OF PORE-NETWORK STRUCTURE .....	81
4.4.1	Validation of the Algorithms .....	81
4.4.2	Pore-Network Structure Properties .....	89
4.5	IMPACT OF IMAGE RESOLUTION ON PORE-NETWORK STRUCTURE PROPERTIES .....	96
4.6	SPATIAL CORRELATION OF PORE-NETWORK STRUCTURE .....	102

<b>5. CONCLUSIONS AND RECOMMENDATIONS.....</b>	<b>109</b>
<b>REFERENCES.....</b>	<b>114</b>
<b>APPENDIX: CODES .....</b>	<b>125</b>
<b>VITA .....</b>	<b>160</b>

## List of Tables

Table 2.1: Application of imaging techniques for porous media systems .....	29
Table 3.1: Materials and data sets .....	65
Table 4.1: Comparison between medial axis (MA) and Delaney tessellation (DT) based approaches on theoretical packings.....	84
Table 4.2: Comparison between medial axis (MA) and modified Delaney tessellation (MDT) based approaches on random packing .....	85

## List of Figures

Figure 2.1: Interfacial tensions between a solid surface, C, a wetting phase, A, and a nonwetting phase, B .....	8
Figure 2.2: Different saturation states in a water-wet porous media system (wetting phase saturation for left to right) .....	9
Figure 2.3: Capillary-pressure saturation curve for two-phase flow.....	11
Figure 2.4: Haines jump through adjoining pore-body (if neighboring pore-body is filled with wetting phase) .....	12
Figure 2.5: Imbibition mechanisms.....	13
Figure 2.6: Theoretical attenuation coefficients vs. photon energy for different systems	31
Figure 3.1: Top view of a tomography beamline .....	33
Figure 3.2: Dependency of image quality on the angular increment .....	36
Figure 3.3: White field image .....	37
Figure 3.4: Sinogram of a glass bead system .....	38
Figure 3.5: Reconstructed image from non-centered sinogram (left), centered sinogram (right).....	39
Figure 3.6: A sinogram with vertical streak (left), ring artifact in the reconstructed image (center), and filtered ring artifact (right) .....	40
Figure 3.7: Fourier slice theorem: the relation between the image space, Radon space, and the Fourier space .....	41
Figure 3.8: Reconstructed images from different interpolation methods.....	44
Figure 3.9: Example of simple and Kriging indicator segmentation algorithms .....	49
Figure 3.10: Example of segmentation of an image that contains more than two phase ..	50
Figure 3.11: A Typical two-point correlation function for glass bead system.....	52
Figure 3.12: The REV concept for porosity.....	54
Figure 3.13: Medial axis in a simple two-dimensional system.....	55

Figure 3.14: (a) Burning algorithm and creation of the medial axis in 2D image, (b) A voxel is considered a medial-axis voxel if the burn algorithm enters the voxel from indicated directions .....	57
Figure 3.15: The inscribed pore body located on the local maxima on the medial axis on a cross section .....	58
Figure 3.16: Merging of two pore bodies that occupy the same void space. If there is any overlap, the larger pore is chosen.....	58
Figure 3.17: The inscribed pore throat located on the local minima on the medial axis on a cross section.....	59
Figure 3.18: (a) Small random packing, (b) medial axis, and (c) location of pore-bodies on the media axis.....	60
Figure 3.19 : A typical semivariogram .....	63
Figure 4.1: Cross-sectional and three-dimensional images of the X_L_B system .....	66
Figure 4.2: Cross-sectional and three-dimensional images of the L_B system .....	67
Figure 4.3: Cross-sectional and three-dimensional images of the M_B system .....	67
Figure 4.4: Cross-sectional and three-dimensional images of the S_B system .....	68
Figure 4.5: Cross-sectional and three-dimensional images of the P_B_1 system .....	68
Figure 4.6: Cross-sectional and three-dimensional images of the P_B_2 system .....	69
Figure 4.7: Cross-sectional and three-dimensional images of the O_S_1 system .....	69
Figure 4.8: Cross-sectional and three-dimensional images of the O_S_2 system .....	70
Figure 4.9 : A uniform 100-sphere random packing used to verify calculations of specific surface area.....	71
Figure 4.10: Two-point correlation function of the X_L_B system .....	72
Figure 4.11: Two-point correlation function of the L_B system .....	73
Figure 4.12: Two-point correlation function of the M_B system .....	73
Figure 4.13: Two-point correlation function of the S_B system.....	74
Figure 4.14: Two-point correlation function of the P_B_1 system.....	74

Figure 4.15: Two-point correlation function of the P_B_2 system.....	75
Figure 4.16: Two-point correlation function of the O_S_1 system .....	75
Figure 4.17: Two-point correlation function of the O_S_2 system .....	76
Figure 4.18: REV analysis of X_L_B system.....	77
Figure 4.19: REV analysis of the L_B system.....	78
Figure 4.20: REV analysis of M_B system.....	78
Figure 4.21: REV analysis of S_B system .....	79
Figure 4.22: REV analysis of P_B_1 system .....	79
Figure 4.23: REV analysis of P_B_2 system.....	80
Figure 4.24: REV analysis of O_S_1 system.....	80
Figure 4.25: REV analysis of O_S_2 system.....	81
Figure 4.26: (a) 512–sphere cube packing, (b) location of the pores in the cubic packing, (c) 512-sphere rhombohedral packing, and (d) locations of the the pores in the rhombohedral packing.....	82
Figure 4.27: Uniform random packing and the locations of pore bodies from both methods .....	82
Figure 4.28: Distance distribution for the Rhombohedral packing, upper figure (diameter of spheres = 25 pixels), lower figure (diameter of spheres = 45 pixels).....	86
Figure 4.29: A case of match between pore bodies from MA and MDT methods .....	87
Figure 4.30: A case where there is no match between pore bodies from MA and MDT..	88
Figure 4.31: Distribution of the distance between the centers of matched pore bodies....	88
Figure 4.32: Three-dimensional and cross-sectional images show pore-body locations in P_B_1 system.....	89
Figure 4.33: An example of three-dimensional pore-network structure obtained from....	90
Figure 4.34: Pore-body properties of X_L_B system .....	92
Figure 4.35: Pore-throat properties of X_L_B system.....	92

Figure 4.36: Pore-body properties of L_B system .....	93
Figure 4.37: Pore-throat properties of L_B system.....	93
Figure 4.38: Pore-body properties of M_B system.....	94
Figure 4.39: Pore-throat properties of M_B.....	94
Figure 4.40: Pore-body properties of S_B system .....	95
Figure 4.41: Pore-throat properties of S_B system.....	95
Figure 4.42: Pore-body properties of P_B_1 system .....	98
Figure 4.43: Pore-throat properties of P_B_1 system.....	99
Figure 4.44: Pore-body properties of P_B_2 system .....	99
Figure 4.45: Pore-throat properties of P_B_2 system.....	100
Figure 4.46: Pore-body properties of O_S_1 system.....	100
Figure 4.47: Pore-throat properties of O_S_1 system.....	101
Figure 4.48: Pore-body properties of O_S_2 system .....	101
Figure 4.49: pore-throat properties of O_S_2 system.....	102
Figure 4.50: Indicator semivariogram of X_L_B system .....	104
Figure 4.51: Indicator semivariogram of L_B system .....	105
Figure 4.52: Indicator semivariogram of M_B system.....	105
Figure 4.53: Indicator semivariogram of S_B system.....	106
Figure 4.54: Indicator semivariogram of P_B_1 system.....	106
Figure 4.55: Indicator semivariogram of P_B_2 system.....	107
Figure 4.56: Indicator semivariogram of O_S_1 system .....	107
Figure 4.57: Indicator semivariogram of O_S_2 system .....	108

## **Abstract**

Algorithms were implemented to obtain high resolution three-dimensional images using synchrotron microtomography. Morphological algorithms were developed to extract physically-realistic pore-network structure from unconsolidated porous media systems imaged using synchrotron microtomography. The structure can be used to correlate pore-scale phenomena with the pore structure and can also be incorporated into a pore-network model to verify existing models, understand, or predict transport and flow processes and phenomena in complex porous media systems.

The algorithms are based on the three-dimensional skeletonization of the pore space in the form of nodes connected to paths. Dilation algorithms were developed to generate inscribed spheres on the nodes and paths of the medial axis to represent pore-bodies and pore-throats of the network, respectively. Pore-network structure is captured by three-dimensional spatial distribution of pore-bodies and pore-throats, pore-body and pore-throat size distributions, and the connectivity. Theoretical packings were used to verify the algorithms. Systems of glass bead and natural sand were used in this study to investigate the applicability of the algorithms. Additionally, porosity, specific surface area, and representative elementary volume (REV) analysis of porosity were calculated. The impact of resolution was investigated using perfect glass bead and natural sand systems. Finally, semivariograms and integral scale concepts were used as a tool to investigate the spatial correlation of the network.

Results showed that microtomography is an effective tool to provide quantitative analysis of three-dimensional systems. The quality of the datasets depends on photon

energy, photon flux, size and type of the sample, and the number of projections. The resolution has a significant impact on the construction of the medial axis and extraction of pore network parameters. This impact varies in its significance based on the system and the properties being calculated. Results highlighted the difficulty of creating a unique network from a complex, continuum pore space. Results showed that the algorithms developed are general in use and can be applied to any three-dimensional unconsolidated porous media system. Spatial correlation results showed that systems have different correlation behavior; therefore, it might be not correct if a correlation model is assigned a priori into a pore-network model.

## 1. Introduction

Water and solute transport and the distribution of phases in subsurface systems are directly related to the geometry and the topology of the pore space and can have a strong influence on continuum scale properties. While many processes related to site assessment and remediation are usually studied using a continuum approach, pore-scale modeling is considered a powerful tool to better understand the physical processes involved and to determine macroscale constitutive relationships that can be difficult to obtain experimentally. Network models have been used to study a wide range of single and multiphase flow processes including: relative permeability (Blunt and King, 1990; Rajaram et al., 1997; Fischer and Celia, 1999), the effect of pore structure on relative permeability and capillary pressure hysteresis in two phase systems (Jerauld and Salter, 1990), prediction of permeability and hydraulic conductivity (Bryant et al., 1993a), investigation of the functional relationship between capillary pressure, saturation and interfacial areas (Reeves and Celia, 1996), prediction of permeabilities and residence time distributions for mechanical dispersion in packed beds (Thompson and Fogler, 1997), drainage and imbibition (Lowery and Miller, 1995, Hilpert and Miller, 2001), and phase distributions, interfacial areas and mass transfer (Dillard and Blunt, 2000) .

The first network models idealized the pore space as collection of capillary tubes and provided simple analytical solutions to predict continuum-scale properties such as permeability. However, these models failed to incorporate the interconnectivity of the pore space. The idea of representing the pore space as a two- or three-dimensional network started with the work of Fatt (1956a, b, and c). Due to the complexity of the pore

space morphology, pore bodies and throats are usually represented by simplified shapes. Pore bodies and throats have been represented as spheres and cylinders or cubes and cylinders, respectively. Although network models can be two- or three- dimensional, two-dimensional networks cannot provide a good representation of three-dimensional systems because of their inability to provide a complete representation of the interconnectivity (Chatzis and Dullien, 1977). Common three-dimensional networks are random (e.g., Lowry and Miller, 1995) or cubic lattices with connectivity of six or smaller (e.g., Reeves and Celia, 1996). In actual porous media systems, however, the connectivity can be larger than six and follows nonuniform distributions (Kwiecien et al., 1990).

The most critical aspect of network model construction is identification of the pore-structure (Celia et. al., 1995). Two general approaches are commonly used. The first attempts to create an equivalent network using distributions and correlations of basic morphologic parameters such as pore body and throat sizes. The second attempts to directly map a specific porous medium onto a network structure. The fundamental difference between the two methods is that direct mapping will provide a one-to-one spatial correspondence between the porous medium structure and the network structure, whereas the second type of network is equivalent only in a statistical sense.

Typical parameters used for in the creation of an equivalent network include pore-body and pore-throat size distributions, throat length distribution, coordination number, spatial correlation within the system which includes size correlation between adjacent pore bodies (body-body correlation) and size correlation between neighboring pore throats and pore bodies (body-throat correlation), and pore-body to pore-throat aspect ratio. There are different approaches used to identify the pore structure including the use

of inverse methods to fit model parameters to an experimentally measured pressure-saturation relation and the use of mercury porosimetry or nitrogen adsorption to obtain the pore size distribution of the system.

Direct mapping methods require some method of obtaining the pore structure, prior to construction of the network. Imaging techniques include the analysis of serial thin sections (Cousin, et al., 1996, Vogel and Roth, 2001) and non-destructive techniques such as X-ray microtomography (Rintoul et al, 1996, Lindquist et al., 2000). Non-destructive direct imaging approaches are attractive because they provide a detailed and unique description of the pore space geometry. As important is the fact that the connectivity and spatial variation in pore body and throat sizes are retained. Recent advances in microtomography techniques now allow researchers to non-destructively obtain three-dimensional images of porous media systems on the order of a few microns. Resolutions on this order allow for unprecedented characterization of the pore-scale structure.

The overall objective of this research is to develop, verify and apply a novel suite of techniques and algorithms to extract the physically-representative pore network structure of unconsolidated porous media systems imaged using synchrotron x-ray microtomography. This objective is achieved through the following tasks:

1. Implementation of x-ray microtomography reconstruction algorithms to obtain high-resolution cross-sectional images of the samples imaged using synchrotron x-ray microtomography.
2. Implementation of image processing and visualization algorithms to obtain high-resolution three-dimensional images of the systems.

3. Development of novel algorithms to extract the physically-representative pore network structure from the three-dimensional images. This includes three-dimensional spatial mapping and size distribution of pore bodies and pore throats and their connectivity.
4. Utilization of geostatistics to model the spatial correlation of the developed pore network structure.
5. Verification of the algorithms using regular and random computer-generated three-dimensional sphere packings.
6. A study of the effect of resolution on different pore network parameters using the regular and random computer-generated sphere packings and images of “perfect” glass beads.
7. A series of experiments using synchrotron x-ray microtomography to image various glass bead systems and actual sediment cores.
8. Application of all the algorithms to process, visualize, and extract the physically-representative pore network structure from the images collected in step 7.

The techniques, algorithms and results from this work will allow for the extraction of physically-realistic pore-network structures from unconsolidated porous media systems imaged using synchrotron x-ray microtomography. The data and information obtained will provide much-needed information to researchers in their efforts to better represent and simulate pore-scale processes and phenomena using network or Lattice Boltzmann models. Improvements in pore-scale models will lead to a better understanding and calculation of macroscopic phenomena such as pressure-saturation relations, permeability, relative permeability, formation and characterization of nonaqueous phase

liquids (NAPL) residual, dispersion, and interphase mass transfer. The techniques and results from this study will also provide a tool to validate the currently used networks generated randomly or based on simple arrangements.

## **2. Background and Literature Review**

### **2.1 Introduction to Network Models**

Pore-network models are effective tools used to investigate or predict macroscopic properties from fundamental pore scale behavior of processes and phenomena based on geometric volume averaging. This is mainly due to the fact that explicit solutions to describe the behavior of fluids in porous media system are impractical because of the complexity of these systems. Pore-network models are of two types: quasi-static and dynamic models. Quasi-static models apply a capillary pressure on the network and calculate the positions of fluid-fluid interfaces ignoring the dynamics of pressure and the interfaces. Dynamic models apply inflow rate for each one of the components of the system and calculate the corresponding pressure and the interface positions.

Pore-networks models are mechanistic models that idealize the complex pore space geometry of the porous media by representing the pore space by pore elements having simple geometric shapes. The most critical part in constructing a pore-network model is defining its structure and geometry, i.e., the locations of pore bodies (and hence pore-throat length distribution), pore-body size distributions, throat-body size distribution, connectivity, and the spatial correlation between pore bodies and pore throats (Celia et. al., 1995).

### **2.2 Application of Network Models**

Network models have been used in the fields of chemical engineering, petroleum engineering and hydrology to study a wide range of single and multiphase flow

processes. Applications include relative permeability (Fischer and Celia, 1999), hydraulic conductivity (Bryant et al., 1993a), investigation of the functional relationship between capillary pressure, saturation and interfacial areas (Reeves and Celia, 1996), prediction of permeabilities and residence time distributions for mechanical dispersion in packed beds (Thompson and Fogler, 1997), prediction of drainage and imbibition (Hilpert and Miller, 2001), phase distributions, interfacial areas and mass transfer (Dillard and Blunt, 2000), ganglion formation and mobilization (Dias and Payatakes, 1986; Li and Wardlaw, 1986a,b), and pore scale evaporation processes (Nowicki et. al., 1992).

The following sections provide discussion about single and multiphase processes and phenomena and how they are related to the pore-network structure.

### **2.3 Single and Multiphase Flow Properties**

When the pore space of a porous media is occupied by two or more fluids, two types of flow are possible, miscible displacement and immiscible displacement. In miscible displacement, the two fluids can completely dissolve in each other and there is no fluid-fluid interface. In the case where a fluid-fluid interface exists due to the interfacial tension between fluids, an immiscible displacement occurs as a form of simultaneous flow of the phases that exist in the system (e.g., oil, water, and gas).

#### **2.3.1 Interfacial Tension and Wettability**

The interfacial tension is defined as the work necessary to separate a unit area of two substances from each other (Adamson, 1982). The interfacial tension between a substance and a vapor is called the surface tension. Figure 2.1 shows two immiscible

fluids in contact with a solid surface, the angle between the interface and the solid surface,  $\theta$ , and the interfacial tensions between three phases  $\sigma_{ij}$  (where  $i,j$  is A, B, or C).

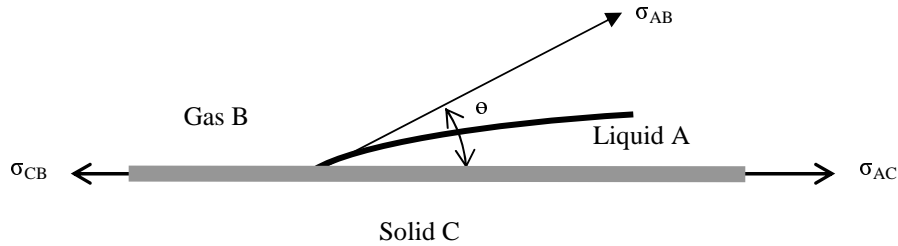


Figure 2.1: Interfacial tensions between a solid surface, C, a wetting phase, A, and a nonwetting phase, B

The relationship between the contact angle and tension of the interfaces is given by Young's equation as (Bear, 1972):

$$\cos \theta = \frac{\sigma_{CB} - \sigma_{AC}}{\sigma_{AB}} \quad (2.1)$$

$\theta$  is called the contact angle and it determines which fluid will preferentially wet the solid (i.e., the wettability of a solid by a liquid). If  $\theta$  is less than  $90^\circ$ , then fluid (A) preferentially wets the surface and is called the wetting fluid. If  $\theta$  is more than  $90^\circ$ , then fluid (B) preferentially wets the surface and fluid (A) would be the nonwetting phase.

Saturation ratio of a fluid, or simply saturation, is the fraction of the void space filled by that fluid. In a water-wet porous media system, three types of fluid saturation can be identified (Bear, 1972). At very low water saturation, water forms a thin film around the solid surface and isolated water-rings around the solid contact angle called pendular rings. These pendular rings become continuous as the wetting phase saturation increases. If the wetting phase saturation increases any further, the saturation is called

funicular and the flow becomes possible due to the continuity of the wetting phase. As the saturation of the wetting phase increases, the nonwetting phase loses its continuity and form isolated droplets. This state is called insular saturation; Figure 2.2 shows these saturation states. The same concept can be applied to oil-wet porous media systems.

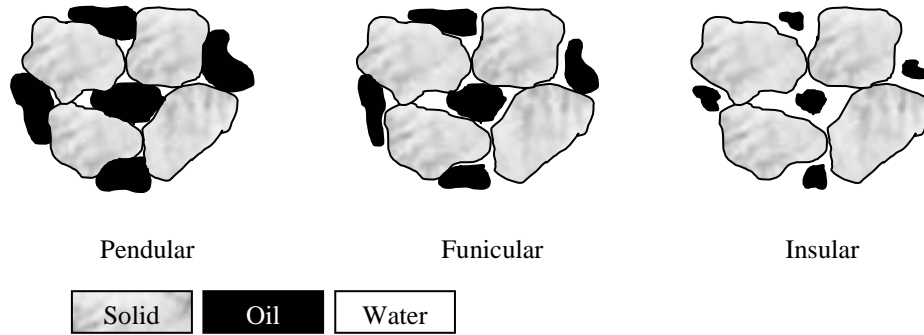


Figure 2.2: Different saturation states in a water-wet porous media system (wetting phase saturation for left to right)

### 2.3.2 Capillary Pressure

The existence of immiscible fluids in the pore space causes a curved meniscus between the fluids which causes a pressure difference between the fluids related to the curvature across the interface. This pressure is called the capillary pressure  $P_c$  (Adamson, 1982), and is defined as:

$$P_c = P_{nw} - P_w \quad (2.2)$$

where  $P_{nw}$  is the pressure of the nonwetting phase and  $P_w$  is the pressure of the wetting phase. The capillary pressure is given by Laplace equation as:

$$P_c = \frac{2\sigma_{ij} \cos \theta}{r^*} \quad (2.3)$$

where  $\sigma_{ij}$  is the interfacial tension between fluids  $i$  and  $j$  and  $r^*$  is the mean radius of curvature ( $2/r^* = 1/r' + 1/r''$ ),  $r'$  and  $r''$  are the principle radii of curvature in the two orthogonal planes.

The capillary pressure depends on the pore geometry (pore radius), on the interaction between fluids,  $\sigma_{ij}$  and on the amount and location of each phase in the pore space. Due to the complexity of natural porous media systems, it is difficult to obtain these parameters analytically. Therefore, the pore space is usually idealized (e.g., capillary tube or uniform spheres) to predict the capillary pressure as a function of the saturation or determined experimentally. In addition, there is no unique relationship between capillary pressure and saturation because of the hysteresis of the capillary pressure.

### **2.3.3 Drainage and Imbibition**

When the system is initially saturated with a wetting phase and displaced by a nonwetting phase, the process is called primary drainage. When the nonwetting is displaced by a wetting phase, the process is called imbibition. Figure 2.3 shows a typical pressure- saturation curves.

As pressure increases, drainage of the system continues until it reaches a point where further drainage is not possible. The amount of the wetting fluid that remains in the system is called irreducible saturation of the wetting phase. There will be no flow of the wetting phase until this level of saturation is exceeded. If we start from this point and follow the imbibition curve by decreasing the pressure and displacing the nonwetting phase by wetting phase, we reach to a point where a certain amount of the nonwetting

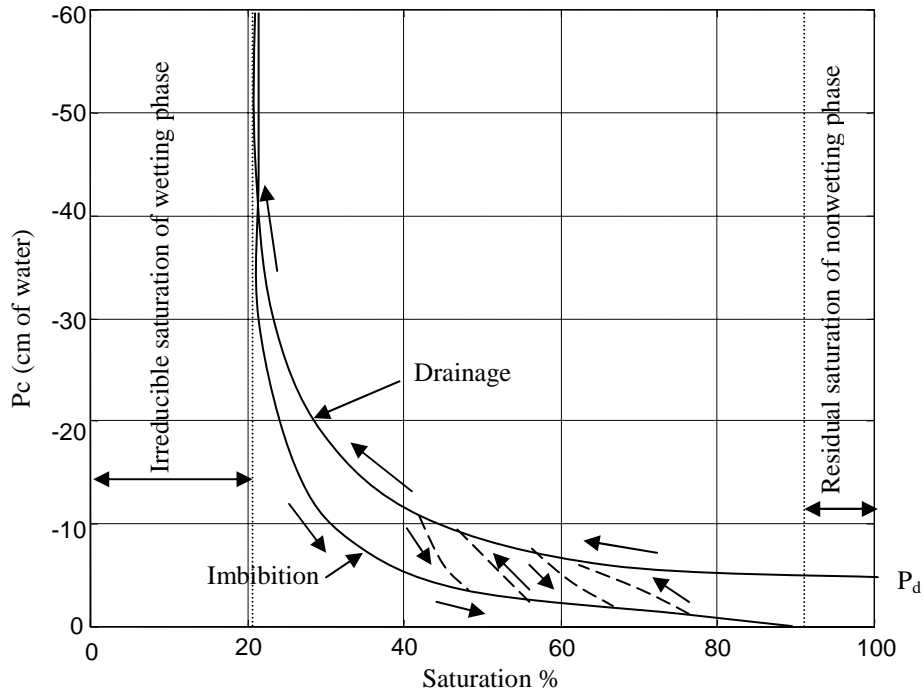


Figure 2.3: Capillary-pressure saturation curve for two-phase flow

phase remains in the system at zero capillary pressure. This amount is called the residual saturation of the nonwetting phase. The imbibition process can be started at any point on the drainage curve and the drainage process can be started at any point on the imbibition curve. These curves are called scanning curves, depicted by the dashed curves in figure 2.3. Point  $P_d$  on the drainage curve (Figure 2.3) shows the minimum amount of pressure required for the nonwetting phase to penetrate a sample saturated with the wetting phase. This pressure that is required to initiate the displacement is called the threshold pressure (or bubbling pressure or nonwetting fluid entry value). This value is controlled by pore-throat size (the maximum radius).

In drainage, the process of the displacement of a wetting fluid by nonwetting fluid occurs through rapid advances of the interfaces called Haines jumps (Figure 2.4), (Jerald

and Salter, 1990). The non-wetting fluid saturation increases as the capillary pressure increases. From the definition of capillary pressure in equation 2.3, the invasion of the nonwetting phase through a pore-throat occurs if the capillary pressure satisfies:

$$P_c \geq \frac{2\sigma \cos \theta}{r_t} \quad (2.4)$$

where  $r_t$  is the pore-throat radius.

Note that drainage process is controlled by the radius of the largest throat. At the end of drainage processes, most of the pore-throats and pore-bodies are filled with nonwetting fluid except a very thin film along the pore-walls occupied by the wetting phase at irreducible saturation (Roof, 1970; Lenormand *et al.*, 1983; Mohanty *et al.*, 1987).

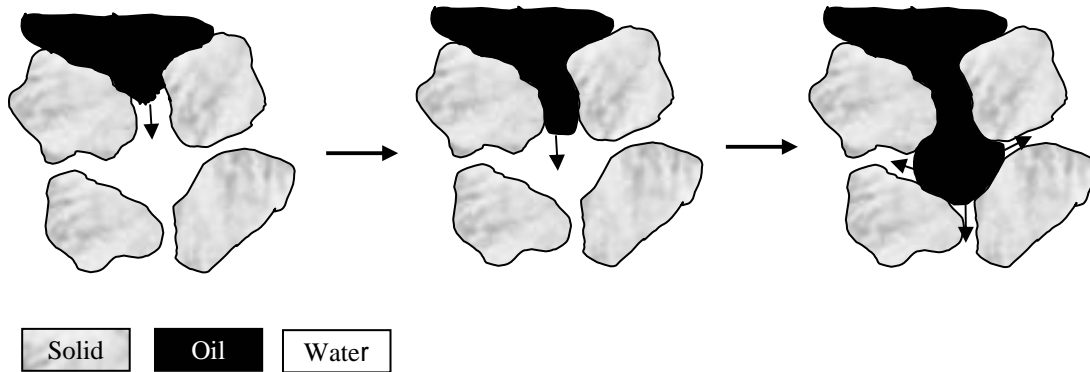


Figure 2.4: Haines jump through adjoining pore-body (if neighboring pore-body is filled with wetting phase)

Imbibition, displacement of non-wetting phase by wetting phase, process takes place via two mechanisms: choke-off (or snap-off) and retraction displacement. In choke-off, the nonwetting phase is displaced from small throats due to wetting phase film flow,

and in retraction, a piston displacement from small pore-bodies takes place (Figure 2.5). Choke-off is controlled by the aspect ratio of the system (the ratio of pore-body size to pore-throat size), as this ratio increases choke-off becomes more dominant (Li and Wardlaw, 1986a, b). In choke-off, the interface in a pore-throat breaks if:

$$P_c \leq \frac{\sigma \cos \theta}{r_t} \quad (2.5)$$

In retraction, the head meniscus within a pore-body leaves the pore-body and moves into the adjacent pore-throats. This event takes place if the capillary pressure satisfies:

$$P_c \leq \frac{2\sigma \cos \theta}{r_b z_{nw}} \quad (2.6)$$

where  $z_{nw}$  is the number of adjacent pore-throats filled with nonwetting phase (Lenormand *et al.*, 1983; Mohanty *et al.*, 1987; Jerauld and Salter, 1990).

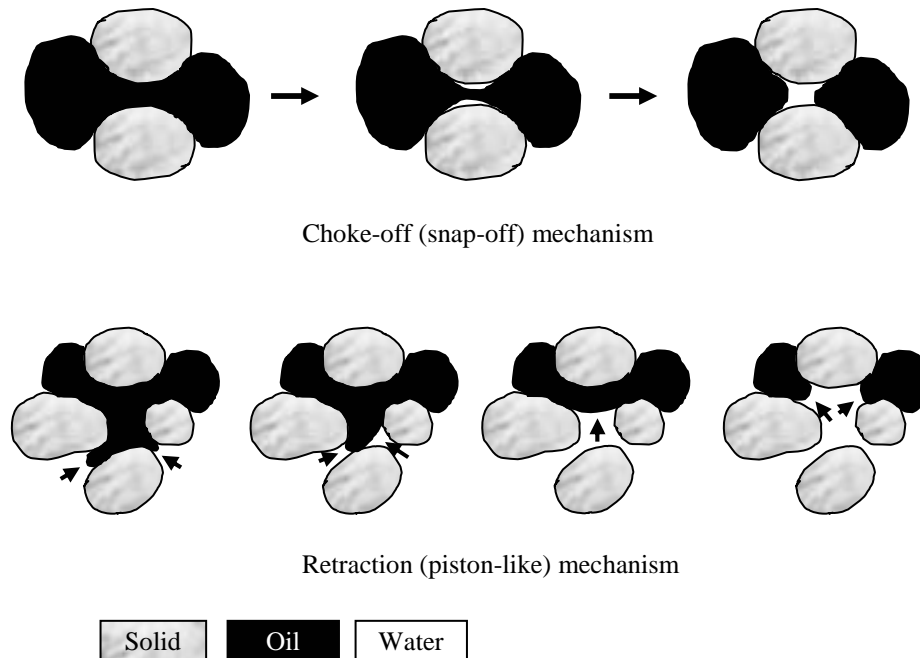


Figure 2.5: Imbibition mechanisms

From the above discussion it is obvious that processes such as drainage and imbibition and hence the distribution of fluid phases in porous media systems depend upon the geometry and the topology of the pore space (pore-body sizes, pore-throat sizes, aspect ratio and the interconnectivity of the pore space). Therefore, characterization and proper representation of the pore space is important to better understand such processes.

### **2.3.4 Relative Permeability**

When two or more immiscible fluids are present in porous media systems, the pore space is partitioned among fluids that exist in the system. As a result, the cross sectional area available for the flow of each fluid is less than the total cross sectional area of the pore space. This condition leads to the concept of relative permeability. Where relative permeability of a fluid at given saturation can be defined as ratio of the intrinsic permeability of the fluid to the total intrinsic permeability of the porous media. As with the pressure-saturation, the location and saturation of the phases is dependent on the morphology of the pore space (Bear, 1972).

### **2.3.5 Interfacial Area and Mass Transfer**

There are models that describe mass transfer among species in multiphase systems. A general form of the mass transfer relationship is given by (Miller *et al.*, 1990):

$$J = K_a (C_s - C_a) \quad (2.7)$$

where  $J$  is the mass flux of the contaminant into the aqueous phase,  $K_a$  is the mass transfer coefficient,  $C_s$  is the solubility limit of the nonaqueous phase liquid (NAPL) in the aqueous phase, and  $C_a$  is the bulk aqueous phase concentration. Environmental researchers usually use a lumped description to describe the mass transfer coefficient as:

$$K_a = k_a a_{na} \quad (2.8)$$

where  $k_a$  is mass transfer rate coefficient and is a function of the porous media properties (Powers *et al.*, 1992); molecular diffusion coefficient of the NAPL species; aqueous phase properties (Miller *et al.*, 1990; Powers *et al.*, 1992; Imhoff *et al.*, 1994) and the initial NAPL volume fraction (Powers *et al.*, 1994).  $a_{na}$  is NAPL/water interfacial area and depends upon the geometry of the pore space and the capillary pressure and it is very difficult to measure due to the complexity and the irregularity of the pore space.

## **2.4 Description of the Pore Space**

The first network models idealized the pore space as a collection of capillary tubes and provided simple analytical solutions to predict continuum-scale properties such as permeability. These simplified models fail to incorporate the interconnectivity of the pore space. Therefore, two- or three- dimensional networks were developed to provide more realistic representation of the pore space (Fatt 1956a, b, and c).

Due to the complexity of the pore space morphology, pore bodies and throats are usually represented by simplified shapes. Pore bodies have been represented as spheres, cubes, or prisms. Pore throats have been represented as circular, rectangular, or triangular cross-section. Although network models can be two- or three- dimensional, two-dimensional networks cannot provide a good representation of three-dimensional systems because of their inability to provide a complete representation of the interconnectivity (Chatzis and Dullien, 1977). Most common network models are cubic lattice with a coordination number of six or less (Dixit *et. al.*, 1998; Fenwick and Blunt 1998; and Dixit *et. al.*, 1999). However, in real porous media systems; the interconnectivity can be larger than six and follows non-uniform distributions (Kwiecien *et al.*, 1990). To overcome this problem, different representations of pore-network models have been suggested to

provide more realistic description of the connectivity. Examples of methods that provide pore-network representation include Delaunay triangulations, Voronoi networks (Blunt and King, 1990; Blunt and King, 1991), and random networks (Lowry and Miller, 1995).

Blunt and King (1990, 1991) generated two- and three-dimensional random networks of interconnected voids to identify the physical properties that affect relative permeability. In 2D networks, random points are placed independently and connected by a network of triangles (Delaunay triangulation). Three-dimensional networks are generated using Voronoi tessellation polyhedra surrounding each point placed randomly in the space. The pores are represented by the vertices of the polyhedra and the connection represented by the edges.

Jerauld and Salter (1990) generated a pore-network model to investigate the effect of pore-structure on relative permeability and capillary pressure in porous media systems. The model consists of spherical pore-bodies connected to cylindrical tubes based on specific pore-body and pore-throat size distributions to match the porosity of the system. Coordination number ranged from 3 to 12 with an average of 6. Regular networks and random Voronoi networks were used in the study. Pore-body and throats were assigned based on probability density functions.

Lowry and Miller (1995) generated a random network model to investigate the factors that affect residual non-aqueous phase liquids (NAPL) in wet, capillary dominated porous media systems. The pore-network model consists of distributed random pore bodies in nonoverlapping pattern. Neighbor pore bodies are connected through cylindrical throats according to a distribution of coordination numbers. Throat radii are

assigned according to a specific probability distribution. Results showed that pore scale geometry significantly affect NAPL characterization.

Reeves and Celia (1996) developed a pore-network model to investigate the functional relationship between capillary pressure, saturation and fluid-fluid interfacial areas and to simulate drainage and imbibition. The model consists of a cubic lattice with constant node spacing and fixed coordination number. The radii of the lattice elements are determined using a beta probability function. The elements of the pore network are pore bodies represented by spheres and pore throats represented by biconical tubes with a fixed radius at the point of contact with the pore bodies. Due to the simplified geometry of the pore-network element, the pore-network model was unable to simulate a pendular wetting fluid. Therefore, the investigation of the impact of wetting pendular fluid on saturation and interfacial areas is not possible. Fischer and Celia (1999) used the same model generated by Reeves and Celia (1996) with modified probability distribution function to predict relative and absolute permeabilities for gas and water.

Fenwick and Blunt (1998) developed a three-dimensional pore-network model to model capillary pressure, relative permeability, drainage and imbibition of a three-phase system. The elements of the network are cubic pore-bodies connected to cubic pore-throats with a coordination number of six. Pore-body and pore-throat sizes were sampled from Weibull distribution.

Dillard and Blunt (2000) developed a pore network model to investigate the physics of nonequilibrium nonaqueous phase liquid (NAPL) dissolution, prediction of relative permeability and hydraulic conductivity. The model consisted of a set of cubic pore bodies connected to rectangular pore throats. A constant coordination number of six

is assumed throughout the entire network. Pore throat length and radius were assigned from a van Genuchten-type cumulative distribution function as:

$$F(l) = 1 - [1 + (\lambda l)^\eta]^{1/\eta - 1} \quad (2.9)$$

where  $l$  is the value of radius or length  $\eta$  is the fitting parameter related to the pore size distribution and  $\lambda$  is a constant,  $F(l)$  is obtained from a random generator. Pore radii were assumed to be equal to the greater of either the largest neighboring tube radius.

## **2.5 Influence of Pore-Network Parameters on Single- and Multi-Phase Properties**

### **2.5.1 Spatial Correlation**

Spatial correlation within a pore-network structure is determined by body-body size correlation, body-throat size correlation, and the aspect ratio which is the average pore-body radius to the average pore-throat radius in the system.

Ioannidis et. al., (1991) and Vizika and Payatakes (1989) conducted micromodel studies and their findings demonstrated the importance of the snap-off mechanism. In conditions of no trapping of wetting phase, the aspect ratio is an important factor in determining the hysteric behavior of the fluid systems (Jerald and Salter, 1990). In a comprehensive investigation to study the effect of spatial correlation in a network model ,Jerald and Salter, 1999, found that throat-throat and body-throat size correlations are significant.

Tsakiroglou and Payatakes (1991) studied the effect of spatial correlation on simulations of mercury porosimetry curves. They found that throat-throat correlations are significant and affect the shape of the pressure saturation curve where it becomes more gradual. Three types of networks were used: uncorrelated, body-throat correlated, and

body-body and body-throat correlated. They found that body-body and body-throat correlated networks strongly affect mercury intrusion curves and these curves become wider. Also, for this type of correlation, the residual mercury saturation is smaller than for uncorrelated networks. These findings agreed with the study of Ioannidis et. al., (1993) in which the general accessibility characteristics of networks were investigated. Spatial correlation among pore-bodies was incorporated according to exponential or Gaussian autocovariance functions. They found that spatial correlation among pore-bodies produces more gradual drainage capillary pressure curves and reduces the residual saturation of the wetting phase.

Bryant et. al., (1993) showed the importance of the spatial correlation between pore sizes in a network constructed from simulated random close packing with uniform spheres. They examined the effect of correlation on permeability by comparing predictions of correlated and randomly distributed networks. They found that incorrect permeability predictions were obtained when the pore size distribution is assigned randomly to throats in the network.

Lymberopoulos and Payatakes (1992) developed a method for the determination of topological and geometrical properties of porous media systems using serial section data coupled with mercury porosimetry where the resolution is low. Correlational behavior of the system was analyzed as follows: to determine body-throat correlation, the diameter and length of every throat is plotted against the average of neighboring pore-bodies. The body-body correlation was determined by plotting the diameter of each pore-body against the average of its neighboring pore-bodies.

Rajaram et. al, (1997) generated a network model consisted of three-dimensional lattice of spherical pore bodies connected to cylindrical pore throats where the sizes are assigned from a lognormal distribution with specific mean and standard deviation. The model was used to predict the relative permeability for unconsolidated soils. They investigated spatial and cross correlations between pore-throat radii in the network. Spatial correlation is the correlation among pore-throats at the same direction and cross correlation is the correlation among pore-throats that connect a site and are oriented in different directions. They observed that increasing spatial correlation leads to more gradual pressure saturation curves and low residual saturation and increasing cross correlation leads to more gradual pressure saturation and increase residual saturation.

Mani and Mohanty (1999) developed a pore-network model to simulate drainage and imbibition in spatially correlated porous media systems. They studied the influence of correlation of the pore space on capillary pressure and permeability. Spherical and Brownian models were used to incorporate correlation in the system. Results showed that drainage and imbibition capillary curves depend upon the type of correlation used. They also found that snap-off mechanism in imbibition becomes more dominant as the spatial correlation increases in the system

Spatial correlation of the pore space in systems at residual NAPL saturations level increases the residual NAPL saturations and causes NAPL blobs to have smaller distributions. Also fluid-fluid interfacial areas decrease in systems with high aspect ratio causing more difficult remediation due to the slow dissolution (Chatzis et al. 1983; Li and Wardlaw, 1986a, b; Lowry and Miller, 1995).

### **2.5.2 Connectivity**

Connectivity is the number of nonredundant closed-loop paths by which all regions inside the shape can be inspected (Dullien, 1992). In the pore-network structure, connectivity is the number of paths connected to a pore body (i.e., the coordination number). Connectivity is an important parameter of the pore-network structure and has a significant influence on many single and multi-phase parameters such as pressure-saturation curves, phase distributions, and interfacial areas (Lowry and Miller, 1995).

Jerauld and Salter (1990) found that relative permeability predictions depend upon the coordination number of the system (the coordination number is the number of paths attached to a pore body). As the coordination number increases within the pore structure, the trapped residual phase decreases as a result of higher probability of maintaining phase continuity. Therefore, the fluid-fluid interfacial areas are expected to decrease and hence the mass transfer rate in the system. Also, in high connectivity systems, the ratio of the total pore-throat volume to the total pore-body volume is larger which decreases the non-wetting phase fraction that is preferentially located in larger pore-bodies which consequently decreases the interfacial areas and mass transfer rates (Dullien, 1992; Wong, 1999). Given this impact of connectivity, it is essential for a pore-network model to incorporate an accurate description of the connectivity of the system.

### **2.5.3 Pore-Body Size Distribution**

The morphology of NAPL blobs at the residual level is influenced by the geometry of the pore space. As pore-body size distribution variability increases, the residual saturation increases and shifts the ganglia volume distributions to larger blobs and the interfacial areas decreases (Lowry and Miller, 1995).

## 2.6 Obtaining Pore-Network Structure from Porous Media Systems

Several methods have been used to obtain pore-network properties from porous media systems, these methods include:

- Estimation of pore sizes from measured capillary pressure-saturation curves (e.g., D'Hollander, 1979, Mishra and Sharma, 1988),
- Fitting generated pressure-saturation curves to the measured curves (e.g., Fischer and Celia, 1999),
- Obtaining the statistics of the network from three dimensional characterization of the pore space (e.g., Liang, et. al., 1999).

The problem with using the first two approaches is the non uniqueness of the solution obtained due the dependency of the retention curves on both the topology of the pore space and pore size distribution (Vogel 2000). Also, no information about the pore space (such as connectivity) is obtained using these methods.

Several approaches have been used to obtain three-dimensional characterization of the pore-space. These approaches include:

- Simulation of random close packing of porous media (Bryant et. al., 1993; Thompson and Fogler, 1997; Hilpert et. al., 2001),
- Three-dimensional reconstruction of the pore space based on the measured porosity and two-correlation function or serial cross sections (Vogel, 1997; Liang et. al, 1999; Ioannidis and Chatzis, 2000; Hidajat et. al., 2001; Vogel and Roth, 2001)
- Direct non-destructive three-dimensional imaging using microtomography or magnetic resonance (Hazlett, 1995; Coker et. al., 1996; Rintoul et al, 1996; Baldwin 1996; Lindquist et al., 2000; Spanne et. al., 2001).

### **2.6.1 Simulation of Random Close Packing of Porous Media**

Bryant et al. (1993) constructed a network from tessellation of random close packing into tetrahedral cells. The cells represent pore-bodies and the pore-throats are represented by the link between cells that have common face.

Thompson and Fogler (1997) generated a network model based on the Delauney tessellation algorithm. Based on the position and the size of each sphere, the pore space is discretized into tetrahedral elements represents pores and interconnectivity of the system.

Hilpert, et. al., (2001) presented a method to calibrate a pore-network model based on pore size distribution obtained using morphological opening. A random packing was simulated and pore bodies were modeled as cubes connected to a maximum number of six throats. Several assumptions were made in their calibration approach based on the measured and simulated pressure saturation curves of the system. These assumptions include: pore-body and pore-throat size distributions follow normal distribution, constant pore-body to pore-throat ratio (aspect ratio) of two, and strong correlation between pore-body and pore throat size.

Network models developed from these studies were based on ideal packings, which restricts the applicability of algorithms applied to obtain the network to media consisting spherical grains. Therefore, the need to obtain a more realistic porous media and hence a network is obvious.

### **2.6.2 Three-Dimensional Reconstruction of the Pore Space Based on its Statistical Properties**

Imaging techniques such as serial cross sections are tools used widely to provide more realistic representation of the porous media and hence the pore space. In this technique, three-dimensional images are reconstructed based on the porosity and the two-

point correlation function measured from the cross-sectional slices. One of the problems of this method is the need for detailed thin cross section to obtain good characterization of the system. This can be impractical or difficult to achieve.

Vogel (1997) used serial cross-sectional images of soil samples to reconstruct a three-dimensional representation of the pore space. They obtained morphological pore-size distributions and connectivity functions for different classes of pore sizes. Discrepancy was found in results obtained from this method and those obtained from water retention measurements.

Liang et. al., (1999) constructed three-dimensional porous media structure based statistics of two-dimensional binary images obtained from serial cross-sections. A thinning algorithm is applied to obtain the skeleton of the pore space and used to predict permeability.

Hidajat et. al., (2001) reconstructed three-dimensional images from its thin cross section using statistics-based methods to simulate transport properties. A skeletonization algorithm was applied to obtain the pore network structure. A three dimensional representation of the system was obtained using serial sections through impregnated samples. The pore-network elements are pore-throats with cylindrical shapes connected to nodes with coordination number of 12. Pore-bodies were assumed to have no volume. The pore-network model was used to simulate drainage, hydraulic conductivity, and solute transport. Simulation results for each property vary as the representative volume of the structure changed.

Although the serial cross sections approach has been widely used to reconstruct three-dimensional systems, problems associated with this method include its laborious

fashion in terms of slicing and digitizing, its destructive nature, and the resolution dependency of thickness of the slices.

## **2.7 Methods to Obtain Pore-Network Structure form Three-Dimensional Images**

Non-destructive direct imaging approaches (i.e., microtomography or nuclear magnetic resonance) are attractive because they provide a detailed and unique description of the pore space geometry. As important is the fact that the connectivity and spatial variation in pore body and throat sizes are retained. Recent advances in microtomography have allowed researchers to obtain three-dimensional images of porous media systems on the order of 10 microns. The next section discusses some studies related to these methods and approaches used to partition pore space into network elements.

Once the three-dimensional images are reconstructed, it is necessary to partition the void space into its constituents of pore and throats. Several approaches, detailed in subsequent sections, utilize the three-dimensional images to obtain the topology and the geometry of the pore space.

### **2.7.1 Binary Representation of the Pore Space**

Hazlett (1995) used three-dimensional images of Berea sandstone obtained using microtomography. These images were used as input in a network model to simulate drainage, imbibition, and fluid spatial distributions. In their work, the pore-space was not partitioned into network elements in the form of pore-bodies connected to pore-throats. The pixellization of the pore space was used instead. The model consisted of a map of inscribed spheres where each pixel in the pore space is assigned a number corresponding to the radius of the largest sphere centered in that pixel without intersecting the solid phase. This inscribed sphere map provides the framework for equilibrium saturation

distributions based on a cut-off radius corresponding to capillary pressure. A drawback of using this approach is overestimating the phase volumes at high capillary pressure during imbibition because the mean curvature of convex shapes is not extracted due to the use of a map of spheres with concave curvatures.

### **2.7.2 Multiorientation Scanning Algorithm**

Zhao et al., (1994) developed a multiorientation scanning algorithm to partition the pore space to pores and throats. This algorithm was then adopted by Ioannidis and Chatzis, (2000). In this algorithm, the throats are identified by finding local minima along the pore space pathways by scanning the microstructure from nine different orientations, three orthogonal and six diagonal orientations. Scanning from different orientation produces overlapping of identification of the local minima and then the smallest is considered to be the throat. To identify pore-bodies, throats and solid voxels are clustered in one phase and the remaining void space is clustered to represent the pore bodies. A problem with this approach is its inability to define inscribed pore bodies.

### **2.7.3 Morphological Thinning Algorithm**

Baldwin et al., (1996) developed a morphological thinning algorithm to obtain a representation of the skeleton (medial axis) of the pore space and partition the void space into corresponding pores and throats. No attempt was made to use the medial axis itself as tool to characterize pores and throats; the thinned images were used instead. In their work, the pores are identified by summation of the voxels bounded by the solid matrix and the locations corresponding to local minima are defined as pore necks. A limitation of this approach is that the thinning algorithm is based on a simple segmentation algorithm that leads to misidentification or less accurate partitioning of the void space.

#### **2.7.4 Medial-Axis Skeletonization**

Lindquist et al. (2000) developed algorithms to calculate effective pore body and pore throat radii and other geometric properties such as interconnectivity based on the medial axis of the pore space. Their algorithms primarily have been applied to consolidated systems, and it is not clear whether they are applicable to higher porosity materials (e.g., unconsolidated media).

#### **2.7.5 Quantitative Morphology**

Vogel and Roth (2001) generated a pore-network model based on pore-size distribution and connectivity function obtained by calculating three-dimensional Euler number. Pore size distribution is obtained by a series of erosion dilation algorithms. In order to determine the proportions of the pores with a radius smaller than a given radius  $r$ , a sphere of a radius  $r$  is placed in every location in the pore space. Then erosion is performed to enclose all pore voxels where the sphere fits completely into the pore space. This step is followed by dilation to remove all pores smaller than  $r$ . The connectivity within and between different classes of pore sizes is determined by a specific Euler number which is a function of number of vertices, edges, faces, and volumes of the binary image which represent the pore space. A limitation of this algorithm is that the range of the pore sizes should be known a priori.

Coles et. al., (1998) utilized high resolution (30 microns) three-dimensional images of sandstone samples to study fluid saturations. No attempts were made to partition the void space to a realistic pore-network as a collection of pore-bodies connected to pore-throats. The binary images were used as input to lattice Boltzmann

simulations and pore-network mode developed by Hazelett (1995) discussed previously to compare the simulated and measured saturations.

## **2.8 Applications of Imaging Techniques on Porous Media Systems Studies**

Direct mapping methods require a method of obtaining the pore morphology, prior to reconstruction of the network. Imaging techniques include the analysis of serial thin sections (Cousin, et al., 1996, Vogel and Roth, 2001) and non-destructive techniques such as X-ray microtomography (Rintoul et al, 1996, Lindquist et al., 2000). Non-destructive direct imaging approaches (i.e., tomography) are attractive because they provide a detailed and unique description of the pore space geometry. Equally important is the fact that the connectivity and spatial variation in pore body and throat sizes are retained.

Recent advances in microtomography have allowed researchers to obtain three-dimensional images of porous media systems on the order of 5 microns (Lindquist et al., 1996). Table 2.1 presents studies that have been conducted to investigate porous media systems using different imaging techniques. The acquisition of these extremely rich data sets has motivated the development of algorithms designed to extract the pore network parameters.

Table 2.1: Application of imaging techniques for porous media systems

Reference	System	Resolution	Porous media	Measured properties
Petrovic et al., 1982	x-ray scanner	*	Soil, glass beads	Soil bulk density
Crestana et al., 1985	x-ray computed tomography	*	Sandy and fine sandy loam	Water content variations
Crestana et al., 1986	x-ray miniscanner	*	Fine sandy loam	Water content and soil bulk density
Harold et al., 1987	x-ray computed tomography	*	Bera sandstone	Volume fractions
Hunt et al., 1988	x-ray computed tomography	*	Natural soil	Fractures, mud invasion, and litologic characterization
Warner et al., 1989	x-ray computed tomography	*	Natural soil	Air-filled porosity and pore size distribution
Cassel et al., 1990	x-ray computed tomography	*	Natural soil	Variation in water content
Spanne et al., 1994	Synchrotron computed tomography	10 $\mu\text{m}$	Fontainebleau sandstone	Topology and connectivity
Auzerais et al., 1996	x-ray computed tomography	7.5 $\mu\text{m}$	Fontainebleau sandstone	Porosity, volume fractions, permeability and connectivity
Coker et al., 1996	Synchrotron tomography	7.5 $\mu\text{m}$	Fontainebleau sandstone	Porosity, specific surface area and pore size distribution
Lindquist et al., 1996	x-ray computed tomography	5 $\mu\text{m}$	Bera sanstone, glass bead	Porosity , tortouisity, connectivity and specific surface area
Klobes et al., 1997	x-ray computed tomography with mercury porosimetry	400 $\mu\text{m}$	Rock samples	porosity
Coles et al., 1998	Synchrotron tomography	30 $\mu\text{m}$	sandstone	Porosity and water content
Hsieh et al., 1998	Gamma-ray computed tomography	*	dolomite	Porosity and volume fractions
Clausuitzer at al., 1999	x-ray computed tomography	*	Glass beads	Volume fractions
Lindquist and Venkatarangan, 1999	Synchrotron tomography	6 $\mu\text{m}$	Fontainebleau sandstone	Geometrical analysis
Khalili et al., 1998	Positron emission tomography	*	Sandy sediment soil	Visualizaton of fluid transport through the sample
Baldwin et al., 1996	Magnetic Resonance Imaging	*	Uniform glass beads	Pore size distribution, coordination, and specific surface area
Pauli et al., 1997	Magnetic Resonance Imaging	*	Glass filter system	Pore size distribution
Solymer et al., 1999	Scanning Electron Microscopy	1.6 $\mu\text{m}$	Silty and clayey quartz	Porosity ,permeability, and specific surface area
Montemagno and Gray, 1995	Photoluminescence volumetric imaging	1 $\mu\text{m}$	Random soil samples	Porosity, volume fractions, and specific surface area

\* Resolution is on the order of mm or not provided by the author

## 2.9 Microtomography

X-ray Computed Tomography (X-ray CT) provides nondestructive and noninvasive three-dimensional images of the interior of the object by mapping the x-ray absorption through the sample. X-ray CT is based on the reconstruction of the cross-section of an object from its projection data by passing a series of rays through an object, and measuring the attenuation of these rays using detectors placed on the downstream side of the object. Projections are obtained by measuring the x-ray attenuation coefficients of the sample at different angles. These attenuation values are represented in images as discrete elements (pixels in two-dimensional images and voxels in three-dimensional images).

The amount of attenuation depends on the chemical composition of the material (attenuation increases as the atomic mass increases) and the energy of X-ray. The attenuation of X-rays through a homogenous material is calculated based on Beer's law as:

$$\frac{I}{I_o} = e^{-\mu x} \quad (2.10)$$

where  $I/I_o$  is the attenuation of x-ray intensity per unit length of a given material,  $x$  is the thickness of the material, and  $\mu$  is the attenuation coefficient. Figure 2.6 shows theoretical attenuation coefficients for several systems as a function of photon energy for different materials (Hubbell, 1969; NIST, 1995).

Two concepts are important in image analysis: spatial resolution and contrast resolution. Spatial resolution is the ability to resolve close and high contrast features in the image. Two objects will not be separable in an image if the spatial resolution of the

image is larger than the distance between them. Contrast resolution is the ability to distinguish between objects that have a small contrast difference (attenuation coefficient). Synchrotron radiation has several advantages over traditional X-ray sources that make obtaining high-resolution datasets possible, including high intensity (number of photons per second), high degree of collimation (source divergence leads to image blur), and the ability to tune the photon energy over a wide range using an appropriate monochromator for obtaining specific-element measurements (Kinney and Nichols, 1992).

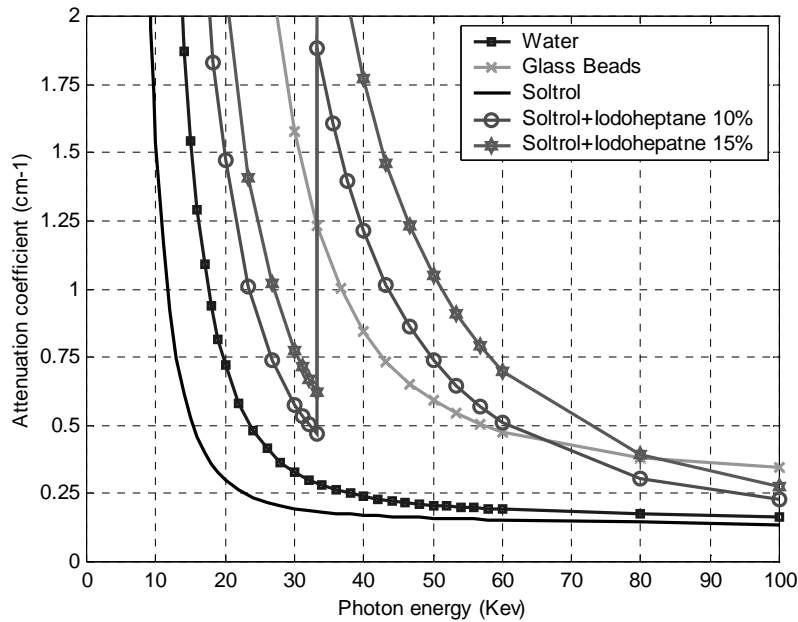


Figure 2.6: Theoretical attenuation coefficients vs. photon energy for different systems

## 2.10 Motivations and Objectives of this Work

Most common network models are either cubic lattices with restricted connectivity, or random pore-network models with variable connectivity generated to provide more realistic representation of the pore space of the porous media. In this study a realistic and representative pore-network structure and geometry is obtained by

capturing the morphology of the pore space using high resolution three-dimensional images obtained using synchrotron X-ray microtomography.

Advantage of using synchrotron microtomography over other imaging techniques is its ability to provide high-resolution three-dimensional images in a nondestructive and noninvasive fashion. This mainly is due to the properties of the synchrotron radiation (i.e., high intensity and degree of collimation).

Most of the previous studies using synchrotron X-ray microtomography have focused on consolidated materials such as sandstone. While this is a typical porous media for petroleum engineering applications, most contamination scenarios in natural systems are better represented by unconsolidated materials with higher porosity.

Methods available to partition the pore space into a pore-network are limited by being two-dimensional or by their limited applicability to certain types of systems. Also, most of these methods don't provide networks valuable for multiphase flow problems where the inscribed radius of pore-throats and pore-bodies is needed. None of these methods have used geostatistics to model the spatial correlation of the pore-network.

The goal of this research is to utilize synchrotron microtomography to extract physically representative pore network structures of different unconsolidated porous media systems. The techniques and results from this work will allow for the extraction of physically-realistic pore-network structure. This pore-network structure can be used to correlate pore-scale phenomena with the pore structure and can also be incorporated into a pore-network model to verify existing models, understand, or predict transport and flow processes and phenomena in complex porous media systems such as pressure saturation curves, permeability, interfacial areas, and mass transfer rates.

### 3. Materials and Methodology

#### 3.1 Synchrotron Microtomography Instrument Description

Figure 3.1 shows a top view of schematic illustration of the microtomography beamline at the Center for Advanced Microstructures and Devices (CAMD). X-rays pass through and around the sample and then hit a thin high resolution CsI (T1) scintillator placed behind the sample to convert the x-ray attenuation map to a visible image. The image is magnified by a microscope objective with x1 or x4 magnification. The front surface, 45° mirror is used to protect the cooled charge-coupled device (CCD) camera from the direct exposure of X-rays. A CCD with 1536x1024 pixels of 9 micron size, Kodak-1600E chip is used to capture each projection during the scan. Defects in the chip (such as point, cluster, or column defects) lead to noisy reconstructed images, but can be suppressed by correcting for white and dark fields. CCD interface is provided with LabVIEW code running on Linux which writes data files with name and path as directed by user and responds to parameter changes coming via interprocess communication (Ham et. al., 2001).

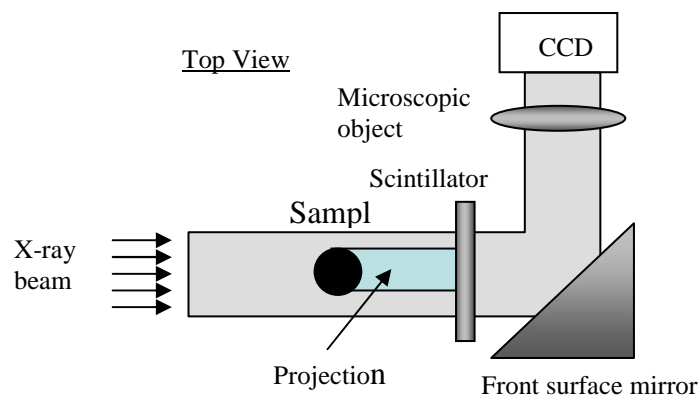


Figure 3.1: Top view of a tomography beamline

Minimizing pitch and roll errors is necessary to obtain good quality microtomography data. In addition, adjustment of the rotation axis of the sample to be coincident with the center column of the CCD is important. The pitch axis is defined with respect to X-ray beam and the roll axis is defined with respect to the CCD rows. Failure to correct pitch and roll error leads to image blurring, and non-centering with respect to the CCD camera leads to ring artifacts in the reconstructed image. The tomography beamline at CAMD consists of a number of automated stages. These stages are controlled via a LABVIEW program running on a Macintosh computer.

Experiments were also conducted at the Advanced Photon Source (APS) at Argonne National Laboratory (Table 3.1). The GeoSoilEnviroCARS (GSECARS) bending magnet beam-line 13-BM-D (sector 13) provides a fan beam of high brilliance radiation which is collimated to a parallel beam with a vertical size of about 5 mm. When used with a monochromator (channel-cut Si 220 and 311 used), energies in the range from 8 to 45 KeV can be obtained with a beam size of 50 mm width and 5 mm height (Rivers, 1999) The sample can be translated and rotated automatically in the beam. A synthetic garnet (Ce:YAG) scintillator is used to convert the transmitted x-rays to visible light. The visible light from the scintillator is imaged with a 5X Mitutoyo microscope objective onto a 12-bit CCD camera (Roper Scientific MicroMAX 5MHz) 1300x1100 pixels, each 6.7 x 6.7 micron in size. Slices were reconstructed using a fast Fourier transform algorithm (Rivers, 2002).

### **3.2 Pre-Processing and Data Collection**

The following is a summary of the steps undertaken to obtain raw X-ray images at the Center for Advanced Microstructures and Devices (CAMD):

1. The sample is mounted on the stage of the microtomography station.
2. Before the experiment starts, Helium gas is run through the system for at least one hour to prevent oxidizing of some components of the system.
3. The alignment of the sample is checked to ensure proper positioning and centering.
4. The optic type and the degree of binning are chosen based on the desired resolution (i. e., x1 optic is used if 9 micron resolution is required and x4 optic is used if the 2.5 micron resolution is required).
5. The CCD temperature is set to -10 °C.
6. Upon activating the x-ray beam and closing the hutch door, images are taken with a given time of exposure to ensure that the CCD is not overexposed. Counts in the field of view should be in the order of 80% of those outside the field of view. This can be checked by inspection of several pixel values inside and outside the field of view. This step may take several trials to obtain the proper exposure time that corresponds to reasonable counts.
7. The image is cropped to remove any extra data outside the region of interest.
8. The beamline is closed and five dark field images are taken. These will be used to correct the raw images.
9. Experimental parameters are set, including: initial angle, final angle, angular increment, and frequency of obtaining white fields.
10. The beamline is opened and images are taken starting from the initial angle to the final angle with the specified angular increment.

### 3.3 Data Processing and Reconstruction

The tomography process and data reconstruction is performed through the following steps:

#### 3.3.1 Collection of the Raw Images

Raw images are collected at constant angular increments from  $0^\circ$  to  $180^\circ$ . There is a trade off between the angular increment and the size of the datasets and consequently, the time of processing and quality of the image. Figure 3.2 shows cross-sectional images from a simulated uniform random packing used in this research reconstructed with different angular increments.

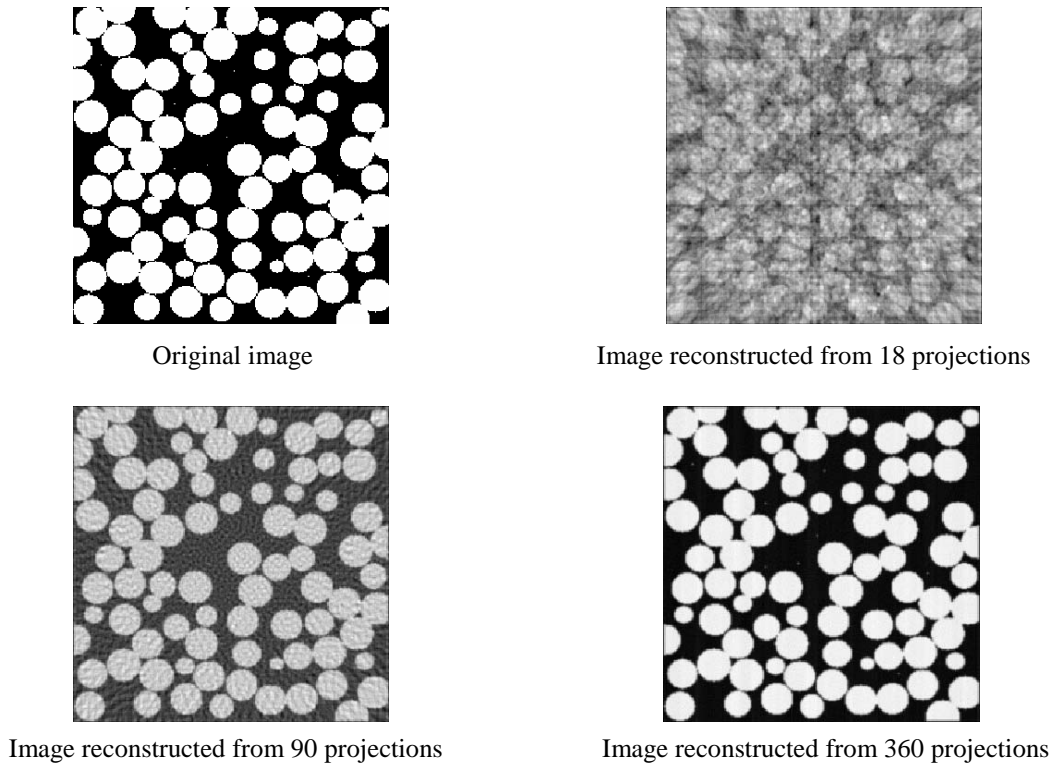


Figure 3.2: Dependency of image quality on the angular increment

### 3.3.2 Correction for Dark and White Fields

The raw images are first corrected using the dark field; i.e., the image of the sample without x-ray. This is achieved by taking the average of the dark images collected at the beginning of the experiment. The raw images are also corrected for white field, which is the image where the sample is moved away from the beam. Correction for the white field is necessary to account for the non-uniformities in the x-ray beam, non-uniform response of the scintillator, and the non-uniform response of the CCD detector. The white field correction is achieved by periodically taking white images and correcting the raw image. Figure 3.3 is an example of a white image.

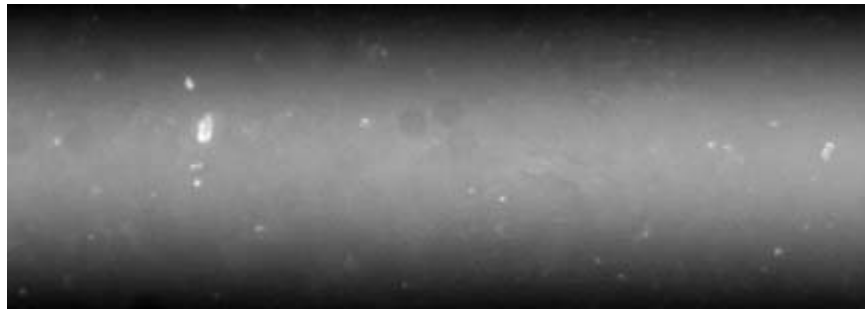


Figure 3.3: White field image

### 3.3.3 Absorption

Logarithmation is performed to obtain the absorption data at each angular increment as follows:

$$\text{Absorption} = \log_{10} (\text{white-dark})/(\text{raw-dark}) \quad (3.1)$$

where, white is the image of the sample when it is moved away from the beam, dark is the image of the sample without x-ray, and raw is the image of the sample at a specific angular increment.

### 3.3.4 Creation of Sinograms

The corrected absorption data are used to create sinograms. A sinogram is a two-dimensional image in which one axis represents the position of view and the other axis represents the same row of the sample at a different rotation angle (see Figure 3.4).

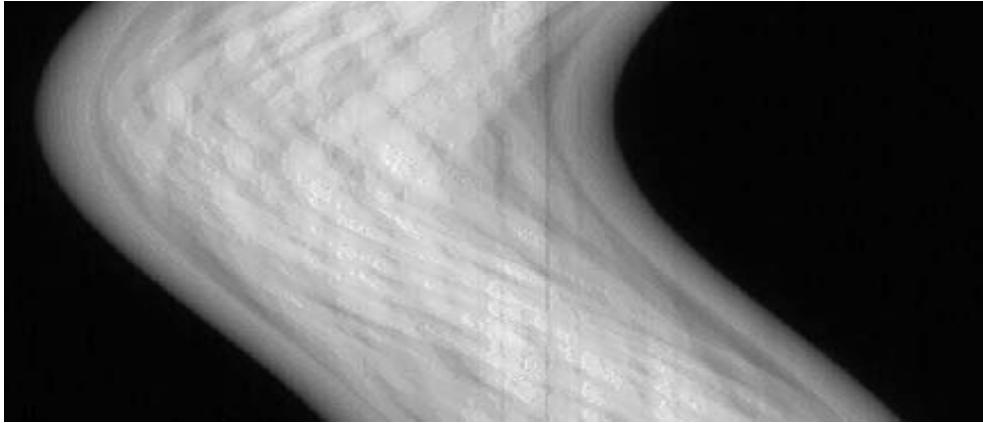


Figure 3.4: Sinogram of a glass bead system

Two main corrections are performed on the sinogram: centering of the sinogram to its rotational axis and vertical streak(s) removal.

### 3.3.5 Centering the Sinogram

The sinogram is centered by first calculating the center of gravity of each of its row and then fitting the center to a sine wave in the form of (Rivers, 1998):

$$y = a + b \sin(x + c) \quad (3.2)$$

where  $a$  is the rotation axis,  $b$  is the amplitude, and  $c$  is the phase.

The sinogram is then adjusted so that its center column matches the rotation axis (i.e., the symmetry axis of the fitted sin wave). This usually requires adding or deleting air values in either side of the sinogram. A quick check of sinogram-centering can be

done before any reconstruction by subtracting the absorption image at  $0^\circ$  from the flipped absorption image at  $180^\circ$ . Figure 3.5 shows reconstructed images from centered and non-centered sinograms of the same glass bead system. Figure 3.6 shows the impact of proper centering of the sinogram. The cross-sectional image on the left was reconstructed without centering, while the cross-sectional image on the right (the identical slice) was centered. As can be seen from the figure, failure to center the sinogram leads to artifacts in the form of half-circles around features in the reconstructed image.

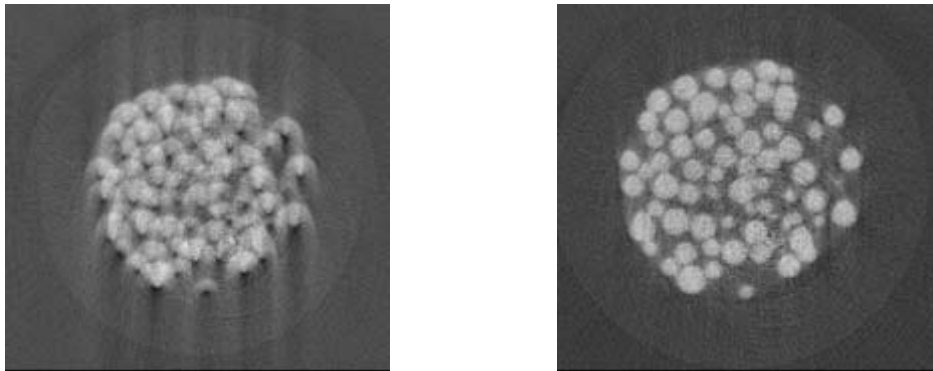


Figure 3.5: Reconstructed image from non-centered sinogram (left), centered sinogram (right)

### 3.3.6 Vertical Streak(s) Removal

Vertical streak artifacts in the sinogram lead to ring artifacts in the reconstructed image. The left image in Figure 3.6 shows a sinogram with a vertical streak, while the center image shows the ring artifact generated when the vertical streak is not removed. Vertical streaks can be caused by a number of factors including, the existence of detective element (i.e., dead pixels in the CCD) with nonlinear responses to incoming intensity; and drifts in the detector element sensitivity in between white-field calibrations.

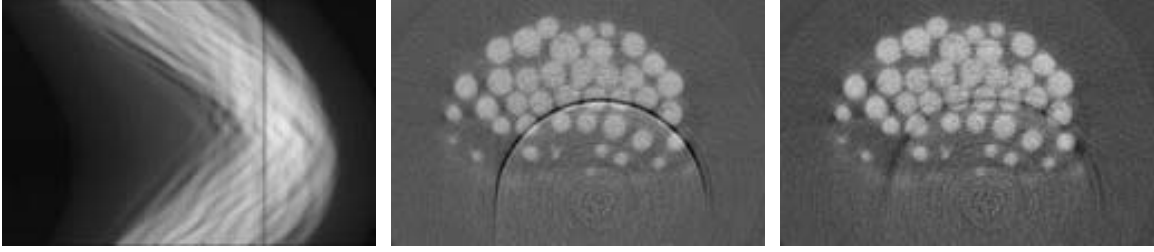


Figure 3.6: A sinogram with vertical streak (left), ring artifact in the reconstructed image (center), and filtered ring artifact (right)

It is very difficult to avoid these artifacts experimentally; however, there are several algorithms that can be applied to the sinogram before the reconstruction to suppress the ring artifacts in the reconstructed image. The following algorithm is adopted and applied for each sinogram separately (Rivers, 1998):

- 1- The average row of the sinogram is found by summing the pixel values of each column and divide by the number of rows.
- 2- Two-dimensional averaging filter is applied on the average row,
- 3- Result from step 2 is subtracted from result from step 1,
- 4- Result from step 3 is subtracted from each row of the sinogram.

### 3.4 Cross-Section Reconstruction Using the Filtered-Back Projection Algorithm

After centering and correcting the sinograms, a filtered-back projection algorithm is applied for each sinogram to create a cross sectional image. Tomographic images are usually reconstructed by taking the inverse of the Radon transform of the projections. The radon transform is given by (Kak and Slaney, 1988):

$$m(t, \theta) = \int_{-\infty}^{\infty} \int_{-\infty}^{\infty} f(x, y) \delta(x \cos \theta + y \sin \theta - t) dx dy \quad (3.3)$$

where  $f(x,y)$  is the image to be reconstructed at angle  $0 \leq \theta < \pi$  from its measured set of line of integrals  $m(t, \theta)$  (see Figure 3.7).

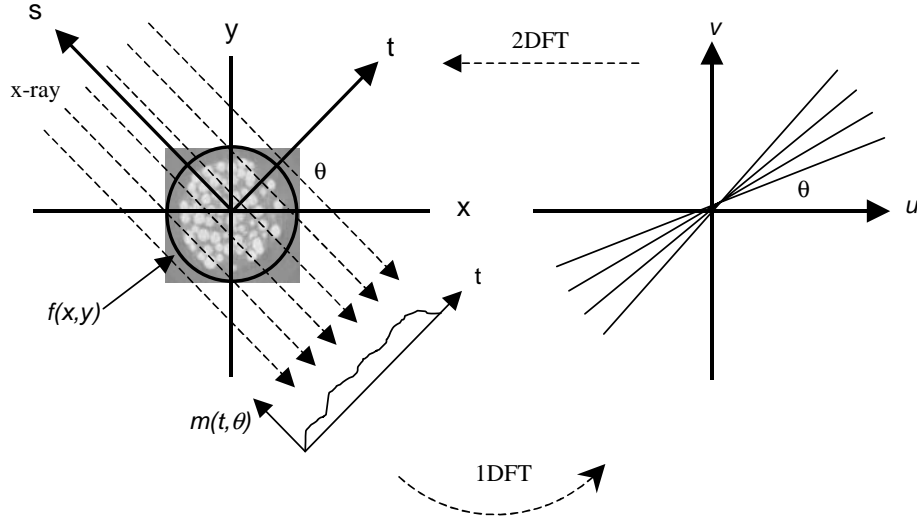


Figure 3.7: Fourier slice theorem: the relation between the image space, Radon space, and the Fourier space

The Radon inverse can be computed based on the Fourier slice theorem where the 1D Fourier transform of a projection taken at angle  $\theta$  equals the central radial slice at angle  $\theta$  of the 2D Fourier transform of the original image. Consider the following equation which describes a projection profile using rotated coordinate system  $(t, s)$ , (Figure 3.7):

$$\begin{bmatrix} t \\ s \end{bmatrix} = \begin{bmatrix} \cos \theta & \sin \theta \\ -\sin \theta & \cos \theta \end{bmatrix} \begin{bmatrix} x \\ y \end{bmatrix}, \quad \begin{bmatrix} x \\ y \end{bmatrix} = \begin{bmatrix} \cos \theta & -\sin \theta \\ \sin \theta & \cos \theta \end{bmatrix} \begin{bmatrix} t \\ s \end{bmatrix} \quad (3.4)$$

equation 3.3 can be rewritten as:

$$m(t, \theta) = \int_{-\infty}^{\infty} f(t \cos \theta - s \sin \theta, t \sin \theta + s \cos \theta) ds \quad (3.5)$$

the one-dimensional Fourier transform (1D-FT) of  $m(t, \theta)$  is given by:

$$\begin{aligned}
F_1\{m(t, \theta)\} &= M(w, \theta) = \int_{-\infty}^{\infty} m(t, \theta) e^{-j2\pi w t} dt \\
&= \int_{-\infty}^{\infty} \int_{-\infty}^{\infty} f(t \cos \theta - s \sin \theta, t \sin \theta + s \cos \theta) e^{-j2\pi w t} ds \\
&= \int_{-\infty}^{\infty} \int_{-\infty}^{\infty} f(x, y) e^{-j2\pi w(x \cos \theta + y \sin \theta)} \begin{vmatrix} \frac{\partial t}{\partial x} & \frac{\partial t}{\partial y} \\ \frac{\partial s}{\partial x} & \frac{\partial s}{\partial y} \end{vmatrix} \\
&= F(w \cos \theta, w \sin \theta)
\end{aligned} \tag{3.6}$$

where  $F(u, v) = F_2\{f(x, y)\}$ ,  $w$  is the frequency variable of the 1D-FT, and  $F_2 = \{f(x, y)\}$  is the two-dimensional Fourier transform 2D-FT. According to the Fourier slice theorem, the original object can be obtained from the inverse 2D-FT. Equation 3.7 gives the 2D-FT along the line ( $u=w \cos \theta$ ,  $v=w \sin \theta$ ) in the  $u, v$  space. Interpolation is implemented in Fourier transforms (FFT) to obtain a discrete implementation of equation 3.7. The inverse 2D-FT expressed in the frequency space using polar coordinates  $w$  and  $\theta$  is given by:

$$\begin{aligned}
f(x, y) &= F_2^{-1}\{F(u, v)\} = \int_{-\infty}^{\infty} \int_{-\infty}^{\infty} F(u, v) e^{j2\pi(xu+yv)} dudv \\
&= \int_0^{2\pi} \int_0^{\infty} F(w \cos \theta, w \sin \theta) e^{j2\pi w(x \cos \theta + y \sin \theta)} \begin{vmatrix} \frac{\partial u}{\partial w} & \frac{\partial u}{\partial \theta} \\ \frac{\partial v}{\partial w} & \frac{\partial v}{\partial \theta} \end{vmatrix} dw d\theta \\
&= \int_0^{2\pi} \left[ \int_{-\infty}^{\infty} M(w, \theta) |w| e^{j2\pi w(x \cos \theta + y \sin \theta)} dw \right] d\theta \\
&= \int_0^{\pi} \hat{m}(x \cos \theta + y \sin \theta, \theta) d\theta = B\{\hat{m}(t, \theta)\},
\end{aligned} \tag{3.7}$$

where  $B\{\hat{m}(t, \theta)\}$  is the back projection of  $\hat{m}$  and  $|w|$  is a filter applied to each projection profile in the frequency space. The most common filters are Ram-Lak, Shepp-Logan, cosin, Hann, or Hamming (Gonzalez and Wintz, 1987). While equation 3.8 gives the continuous back projection operator, the real data consists of a finite number of projections and therefore a discrete implementation of equation 3.7 is performed as follows:

$$B\{\hat{m}(t, \theta)\} = \sum_{\theta=0}^{180} \hat{m}(x \cos \Delta\theta + y \sin \Delta\theta, \Delta\theta) d\theta \quad (3.7)$$

Because of the discrete implementation and change in coordinate systems (see Figure 3.7), an interpolation is required to sum all rays that pass through a particular pixel.

Three types of interpolation can be used (Parker, et al., 1983; Zolzer and Boltze, 1994):

1. Nearest neighbor interpolation: This is the easiest method of interpolation where an intermediate value is found by assigning the new value to the value of the nearest point.
2. Linear interpolation: In this method, two values are used to calculate the intermediate value based on their relative distances.
3. Cubic Spline interpolation: Cubic spline is a special case of spline interpolation.

The cubic spline interpolation function is give by:

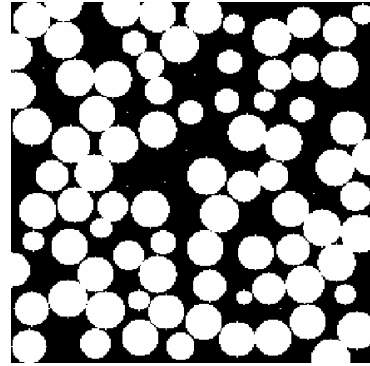
$$r(x) = \left\{ \begin{array}{ll} (a+2)x^3 - (a+3)x^2 + 1 & 0 \leq |x| \leq 1 \\ ax^3 - 5ax^2 + 8ax - 4a & 1 \leq |x| \leq 2 \\ 0 & otherwise \end{array} \right\} \quad (3.8)$$

In the case of image resampling  $a = -0.5$  gives more accurate results (Parker, et al., 1983).

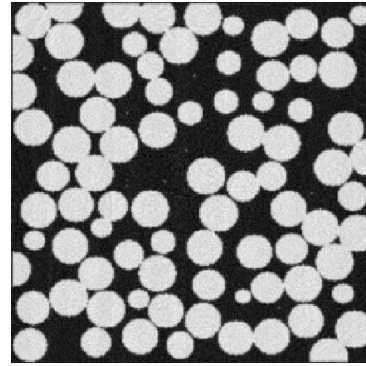
The intermediate pixel value is calculated based on four pixel values as:

$$P_{\text{int}} = P_1r(m-2) + P_2r(m-1) + P_3r(m) + P_4r(m+1) \quad (3.9)$$

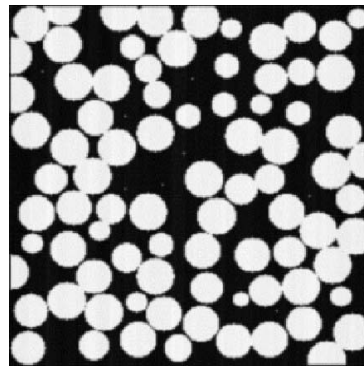
Figure 3.8 shows different reconstructed images using the three interpolation methods.



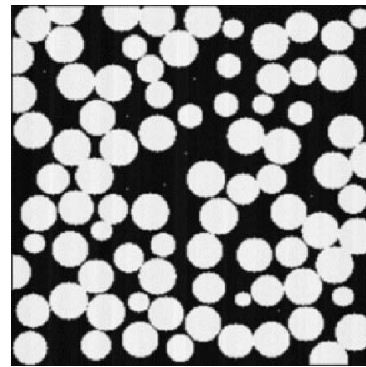
Original image



Nearest interpolation, Shepp-logan filter



Linear interpolation, Shepp-logan filter



Spline interpolation, Shepp-logan filter

Figure 3.8: Reconstructed images from different interpolation methods

### 3.5 Image Processing

After the cross-sectional images have been reconstructed and before any analysis can be performed, two additional steps must be performed: scaling of the cross-sectional images

to be stacked in one volumetric data set, and filtering (smoothing or enhancing the image) of the three-dimensional data set.

### 3.5.1 Scaling the Data

Scaling the data is an image enhancement technique used to improve the contrast in an image by adjusting the range of intensity values of the image. In microtomography images, absorption data are scaled to produce images with gray scale level (intensity values range from 0 to 255). Each pixel in the image is scaled according:

$$P_{out} = (P_{in} - P_{min}) \left( \frac{Scale_{max} - Scale_{min}}{P_{max} - P_{min}} \right) + Scale_{min} \quad (3.10)$$

where  $P_{out}$  is the output value of the pixel after scaling,  $P_{in}$  is the input value,  $P_{min}$  and  $P_{max}$  are the minimum and the maximum intensity values of the original image,  $Scale_{min}$  and  $Scale_{max}$  are the minimum and the maximum intensity values of the scale used, In the case of gray scale, these values are 0 and 255 respectively.

Using the absolute minimum and maximum values for scaling can dramatically affect the output if these values are outliers. To avoid this problem, the 5th and 95th percentile are used to represent the minimum and maximum pixel values. These values are determined based on the histogram of the image, where the 5th percentile means that 5% of the pixels in the image have values less than this value and 95th means that 5% of the pixels in the image have values larger than this value.

### 3.5.2 Filtering the Data

Filters are used in image processing to smooth the image by suppressing either high frequency data values. Filtering can be performed in the frequency or the spatial

domain. Filtering is performed by convoluting the original image with a specific filter function as:

$$g(i, j) = h(i, j) \otimes f(i, j) \quad (3.11)$$

where  $g(i, j)$  is the filtered image,  $h(i, j)$  is the filter, and  $f(i, j)$  is the original image.

Since the digital images are just a discrete representation as set of pixels, a discrete convolution can be performed as the multiplication of a discrete moving mask (kernel) over the image. If a squared kernel with size  $m \times m$  is used, the filtered image can be calculated as (Fisher et. al., 1997):

$$g(i, j) = \sum_{m=-\frac{m}{2}}^{\frac{m}{2}} \sum_{n=-\frac{m}{2}}^{\frac{m}{2}} h(m, n) f(i - m, j - n) \quad (3.12)$$

Kernels vary based on the application of interest. The size and the form of the kernel define the type of the operation. Detailed description of kernels can be found in any image processing textbook (e.g., Fisher et. al., 1997; Russ, 1999). The following discussion illustrates the two types of filters used in this research: mean and median filters.

### 3.5.2.1 Mean Filter

A mean filter is used to reduce the intensity variation between neighboring pixels. Each pixel in the image is replaced by the average value of its neighbors. For example, if a kernel of size  $3 \times 3$  is used, the center of the kernel is placed on each pixel of the original image and its value is replaced by the average value of the 9-neighbor pixels. Two main problems are encountered when using a mean filter: its sensitivity to unrepresentative values which will severely affect the mean value of all pixels in its neighborhood; and the blurring effect at the boundaries due to interpolation of values

outside the boundaries of the image (Fisher et. al., 1997). These problems can usually be avoided by the use of a median filter.

### **3.5.2.2 Median Filter**

The median filter is used to reduce the noise in the image in a way that preserves the details of the image. The idea of the median filter is to replace each pixel in the image by the median value of the neighboring pixels. The median is calculated based on the size of the kernel used where pixels values are sorted into numerical order and then replacing the considered pixel by the middle pixel value(s). The median filter is more robust than the mean filter in that a single outlier will not affect the median value. Also, the median filter is considered more realistic because it doesn't create a new value; the value of the pixel of interest is picked up from the neighboring pixels.

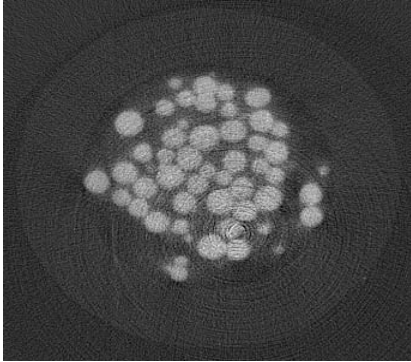
## **3.6 Image Segmentation**

In order to obtain a morphological representation of the porous media system and quantify pore scale parameters such as porosity, specific surface area, tortuosity, and pore network structure, a binarization or segmentation process must be implemented to “divide” the images into two phases. Segmentation is the process of converting a gray-scale or color image to a binary image by identifying two populations in the image based on their intensity values. The simplest segmentation techniques employ global thresholding, where the spatial dependency of phases is ignored (Fisher et. al., 1997). One threshold value is used for the entire system, with values below this value assigned to phase one and values above the threshold value assigned to phase two. Usually the threshold value is chosen based on the histogram of the image. This type of algorithm often leads to phase misidentification due to finite resolution effects or noise in real three-

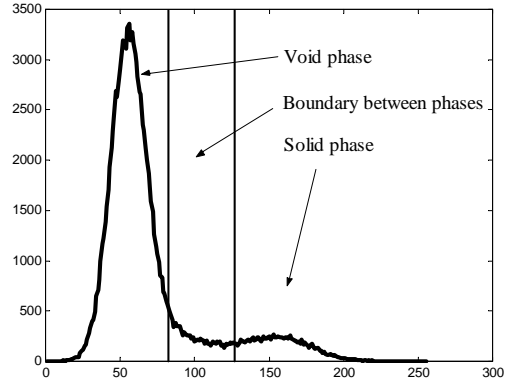
dimensional images. Another approach for segmentation is to use local thresholding criteria based on indicator kriging as described by Oh and Lindquist (1999). In this approach, the segmentation is based on two threshold values, T1 and T2; intensity values below the lower threshold value are identified as phase one and intensity values larger than the higher threshold value are identified as phase two. Values between the two threshold values are assigned to either phase using the maximum likelihood estimate of each phase based on the two-point correlation function. Local thresholding is an important aspect of segmentation, particularly for three-dimensional images such as ones generated by x-ray microtomography.

Figure 3.9 shows a representative cross-section image, the resulting histogram, and threshold values applied in each segmentation technique.

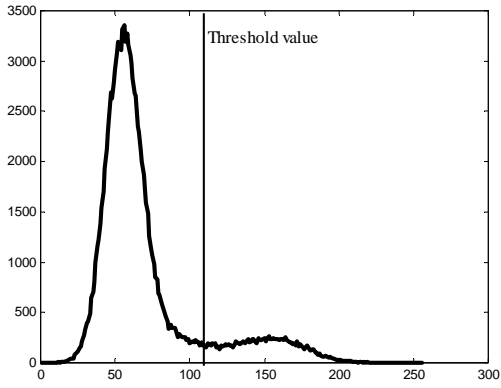
Figure 3.10 is used to illustrate the concept of segmentation when the image contains more than two phases. Raw image is a synchrotron microtomography image of a mixture containing high-impact polystyrene (HIPS) and a two-component flame retardant, a brominated phthalimide dimer (BT-93) and antimony oxide (Ham et al., 2002). Three discrete phases are observed in the image: black phase, yellow phase, and red phase. Figure 3.10, b, c, and d show the segmented (separated phase) from the original image. These calculations were calculated based on indicator kriging where the threshold values for each case were obtained from observation of the discrete pixel values for each phase. In each segmented image (b, c, and d), the white color represents the separated phase (the phase of interest).



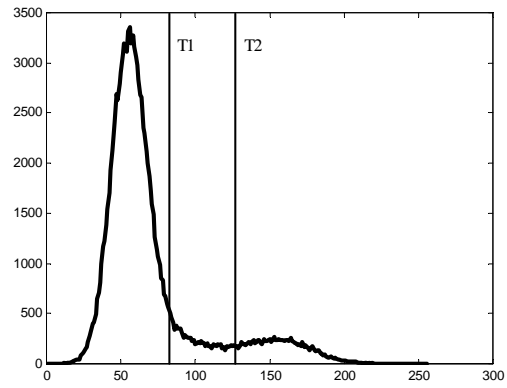
(a) Original image



(b) Histogram of the image



(c) Simple segmentation



(d) Kriging indicator segmentation

Figure 3.9: Example of simple and Kriging indicator segmentation algorithms

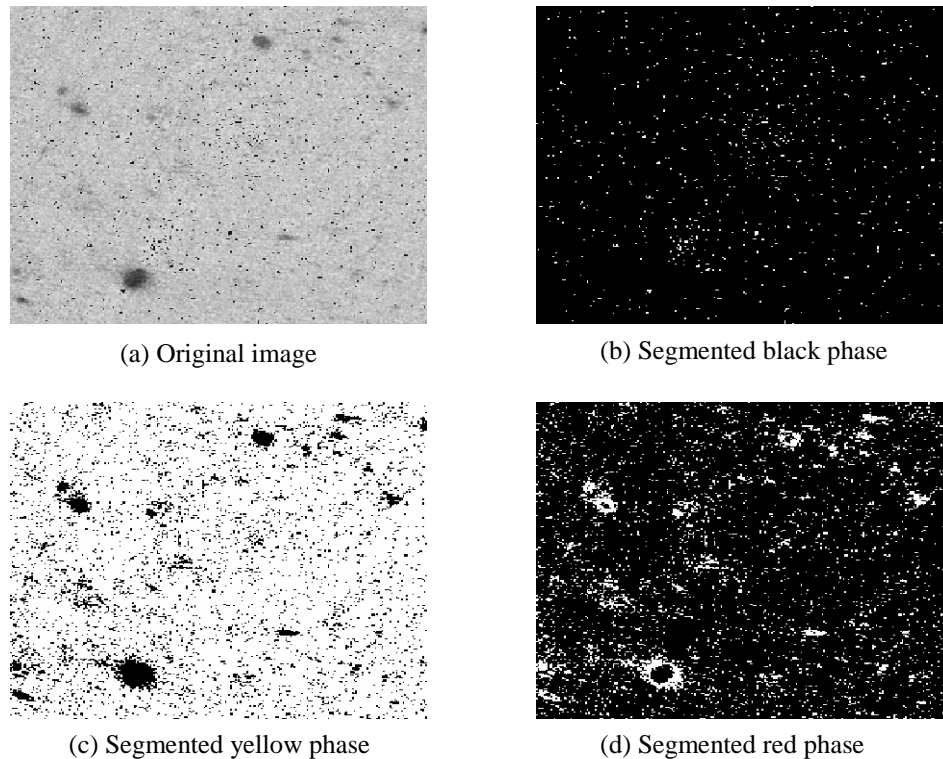


Figure 3.10: Example of segmentation of an image that contains more than two phase

### 3.7 Porosity and Specific Surface Area

Porosity and specific surface area (specific surface area is the interstitial surface area of the void space per bulk volume) can be trivially calculated from binary segmented images by simple count of the voxels of the pore space to calculate the porosity and count voxel interfaces between the void and the solid phases to calculate the specific surface area. Porosity and specific surface area can also be calculated using the two-point correlation function. In general, an  $n$ -point correlation function is a measure of the probability of finding  $n$  points in the region of space occupied by one phase. When computing correlation functions from digital images, it is important to take into account issues such as converting to polar coordinates, and to consider the limitation of digital images (Berryman, 1985; Berryman and Blair, 1986, 1987; Coker and Torquato, 1996).

For isotropic media, the algorithm can be applied to each two-dimensional slice in the data and the results averaged for the three-dimensional volume. Preliminary analysis of the systems analyzed in this work showed that the two-point correlation functions in x-direction, y-direction, and z-direction are the same.

For a two-phase porous media, a characteristic function  $f(x) = 0$  or  $1$  can be defined where the void phase has a value  $f(x) = 1$  and the solid phase has a value  $f(x) = 0$ . The one-point and two-point correlation functions are given by (Berryman et. al., 1986):

$$\hat{S}_1 = \langle f(x) \rangle = \phi \quad (3.13)$$

and

$$\hat{S}_2(r_1, r_2) = \langle f(x+r_1)f(x+r_2) \rangle \quad (3.14)$$

where  $S_1$  is one-point correlation function,  $S_2$  is two-point correlation function,  $\phi$  is the porosity,  $r_i$  is a distance in the pore space, and the brackets  $\langle \cdot \rangle$  indicate a volume average over the spatial coordinate  $x$ . The two-point correlation function can be given as:

$$S_2(r) = \frac{1}{V} \int_V d^3x f(x)f(x+r) \quad (3.15)$$

where  $V$  is the total volume of integration.

For a random media, there are two given facts about the two-point correlation function:

$$S_2 = (0) = \phi \quad (3.16)$$

and

$$A_2'(0) = -\frac{s}{4} \quad (3.17)$$

where  $s$  is the specific surface area and  $A_2'(r)$  is the angular average of  $S_2(r)$  and given by:

$$A_2 = \frac{1}{4\pi} \int d\varphi d\theta \sin \theta S_2(r \hat{r}) \quad (3.18)$$

where  $\hat{r} = \hat{r}(\theta, \varphi)$  is a radial unit vector.

Figure 3.11 shows a typical two-point correlation function obtained from a three-dimensional microtomography image of glass beads. From equations 3.18 the porosity is the value of covariance at lag zero and from equation 3.19, the specific surface area is the slope of the function at lag zero. Where the lag is a distance in the void (pore) space.

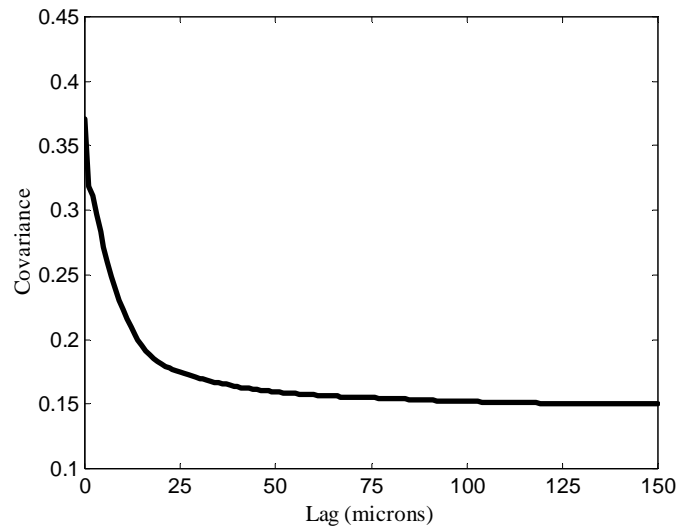


Figure 3.11: A Typical two-point correlation function for glass bead system

### 3.8 Representative Elementary Volume (REV)

The REV is the volume over which a statistical average can be performed (Bear, 1972). A REV should be small enough so that it can be treated as a mathematical point at the continuum and large enough to provide representation of the macroscopic properties of the media. REV's can be defined for different parameters ranging in complexity from porosity to residual nonaqueous phase liquids characteristics. Figure 3.12 illustrates the concept of the REV for porosity. The REV ranges from a minimum limit, which is the transition from the microscopic to the macroscopic level, to a maximum limit, which is the transition from homogenous to heterogeneous state.

REV analysis is performed to ensure that the sample of concern is homogenous and therefore representative. Different approaches are used to calculate the REV from tomography images (e.g., Clausnitzer and Hopmans 1999, Brown and Hsieh, 2000). In this research, the REV for porosity is calculated based on the definition by Bear (1972) as:

$$n_i = (\Delta U_v)_i / \Delta U_i \quad (3.19)$$

where  $n_i$  is the porosity of sub-volume  $i$  and  $(\Delta U_v)_i$  is the volume of the void space in the volume  $\Delta U_i$ .

This definition is implemented on the three-dimensional images by taking a sub-image in the center of the complete image and calculating the porosity. The sub-image is then expanded in all directions a given length (in a form of a sphere or a box) and the porosity is recalculated. This procedure is repeated until the entire image is covered. To avoid the wall effects, images are taken in the center of the imaged volume.

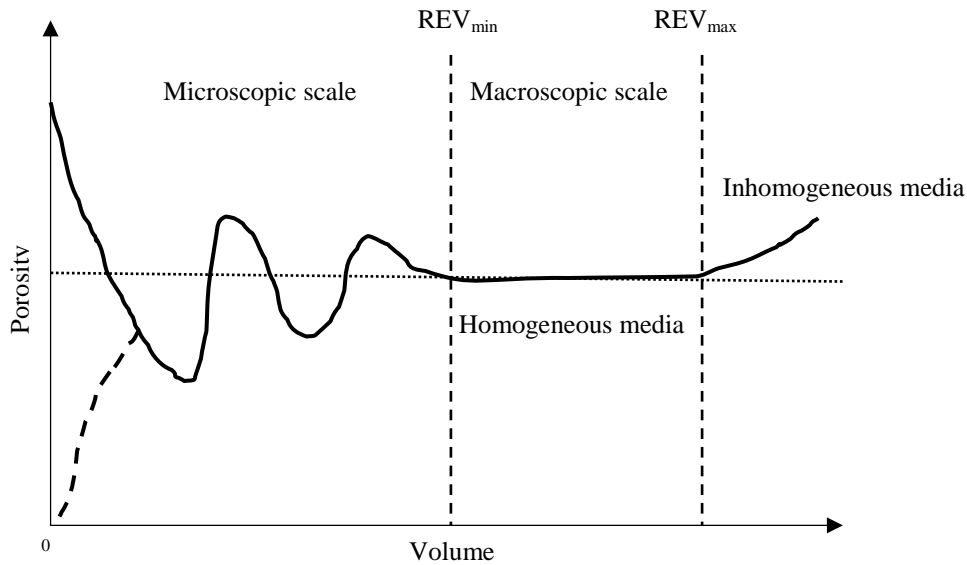


Figure 3.12: The REV concept for porosity

### 3.9 Extraction of Physically-Realistic Pore Network Structure

Extraction of pore network properties includes pore-body and pore-throat size distributions; coordination number; physical location of pore-bodies; spatial correlation within the system which includes size correlation between adjacent pore bodies (body-body correlation), and size correlation between neighboring pore throats and pore bodies (pore-throat correlation), and pore-body to pore-throat aspect ratio. These parameters are obtained based upon the medial axis of the pore space.

#### 3.9.1 Generating the Medial Axis

The medial axis of an object is the skeleton of the object running along its geometrical middle (Lindquist et. al., 1996). For a porous medium, it provides simple and compact information about the topology and geometry of the void space. The first step in defining the medial axis is to apply a segmentation algorithm to separate the phases of the image based on the intensity values. A discrete “burn” algorithm (Kwok, 1988; Sirjani

and Cross, 1991; Lindquist and Lee, 1996) is applied to the segmented binary image to obtain a discrete representation of the continuum pore space.

The medial axis skeleton is obtained by inverting the image so that the background becomes the new foreground and vice versa and then computing the distance transform of the inverted image. The local maximum of the resulting image will represent points on the object's skeleton. Each element of the skeleton is equally distant from at least two different points on the object border. The border points closest to an interior point are called the projection points of the interior point and can be obtained from distance transform (Goldak *et al.*, 1991; Brandt, 1992; Lohmann, 1998). Figure 3.13 shows the concept of the medial axis in a simple, two-dimensional cross-section where circles represent the solid phase and the dashed lines represent the medial axis.

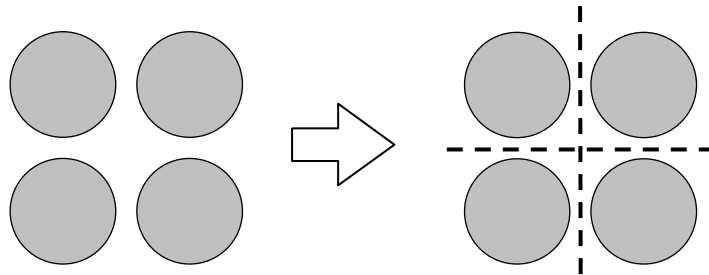
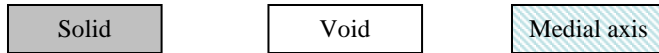
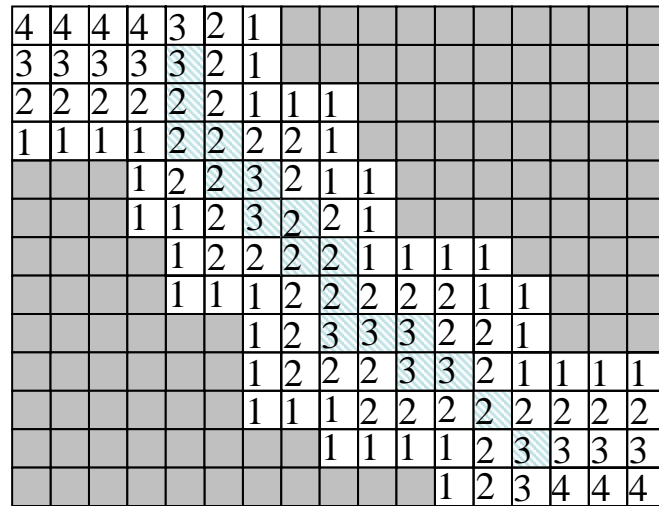


Figure 3.13: Medial axis in a simple two-dimensional system

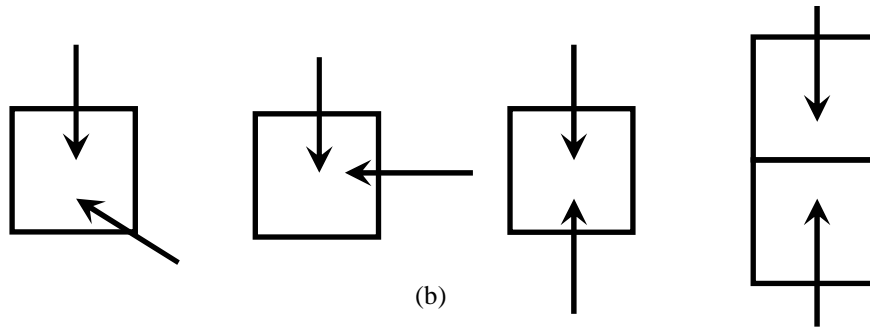
Once the image is segmented, the medial axis is constructed using a burning algorithm developed by Lee et al., (1994) and modified by Lindquist et al., (1996). The burning algorithm is applied as follows (Figure 3.14-a): each voxel in the solid phase is labeled with integer 0, voxels in the exterior region of the image are labeled with integer -1, and voxels in the void space are initially unlabeled. The algorithm proceeds by

simultaneously assigning unlabeled voxels in the void space with an integer  $n+1$  for each voxel neighboring a grain-phase voxel. This procedure continues at a rate of one layer per iteration until all voxels in the pore space are labeled. There are two methods to define the three-dimensional neighborhood of a voxel. The first is face touching, where each voxel can be neighbored by a maximum of 6 voxels. The second is boundary touching, where each voxel can be neighbored by a maximum of 26 voxels. For complex three-dimensional systems, the 26-connectivity approach is required because it provides more accurate description of the connectivity. The determination of the medial axis voxels depends upon the burning direction; if the burn enters a voxel from two different directions that are not perpendicular, the voxel is considered a medial-axis voxel. If the burn enters two neighboring voxels from different directions, both voxels are considered as medial axis voxels (Figure 3.14-b). The result of this burning algorithm is a set of medial axis voxels each with a unique burn number, which is related to its distance from the closest grain voxels. The medial axis in its initial form is made up of a network of one-dimensional paths and nodes at path intersections. The spatial location and the burn number of each voxel in the medial axis is recorded and is used as the base from which to calculate the locations and sizes of pore bodies and pore throats as well as the coordination numbers. It should be noted that the medial axis is very sensitive to the noise and the boundary of the solid phase.

The next sections describe new algorithms, based on the medial axis, to calculate the inscribed radius of pore bodies, pore body throat diameters, connectivity, and body-body correlations of unconsolidated porous media systems. We have chosen to focus on inscribed pore body radii given their critical role in multiphase transport in porous media.



(a)



(b)

Figure 3.14: (a) Burning algorithm and creation of the medial axis in 2D image, (b) A voxel is considered a medial-axis voxel if the burn algorithm enters the voxel from indicated directions

### 3.9.2 Inscribed Pore Radius Calculations

A node is defined as an intersection of three or more paths on the medial axis. Because of the complex, three-dimensional nature of the medial axis, a node might consist of more than one voxel having the same maximum burn number. In this case, one voxel is chosen randomly as the center of the node. A dilation algorithm is performed to find the radius of the pore as follows: (1) start from the chosen voxel on the node and

create a sphere with a radius of one voxel; (2) insert this sphere in the original segmented data and check if there is any overlap between the inscribed sphere and the surrounding grains. If there is an overlap, the procedure stops and this radius is considered as the radius of the pore. If there is no overlap, the algorithm proceeds by increasing the radius by one voxel, and repeats the previous step until an overlap between the grain-phase and sphere occurs. Figure 3.15 shows the location of the inscribed sphere on a cross section.

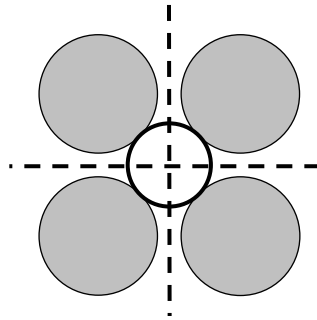


Figure 3.15: The inscribed pore body located on the local maxima on the medial axis on a cross section

In some cases, two or more nodes (and hence pore bodies) occupy what can be considered one void space. Physically, this might not be appropriate because the idea of the pore network is to provide a unique and simple representation of the void space. Therefore, a merging criterion is adopted where two pore bodies are merged if there is any overlap between them. When merging is implemented, the largest pore body is chosen to be the pore body of that void space (Figure 3.16).

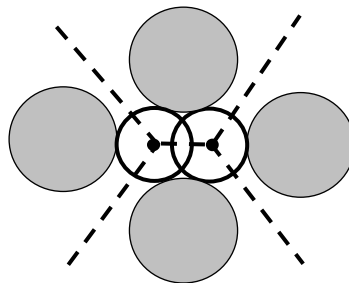


Figure 3.16: Merging of two pore bodies that occupy the same void space. If there is any overlap, the larger pore is chosen

### 3.9.3 Inscribed Throat Radius Calculations

The same dilation algorithm for calculating the pore radii is used to calculate the throat radius. The center of the inscribed-throat sphere is located at the voxel with the minimum burn number along the path connecting two nodes. Because a path is a set of medial-axis voxels that each have exactly two neighboring voxels (on the medial axis), and there might be multiple occurrences of the minimum burn number along the path, the dilation algorithm described above is applied to all the “minimum” voxels along the path. The smallest radius found is considered the inscribed radius. Figure 3.17 presents a schematic of this process.

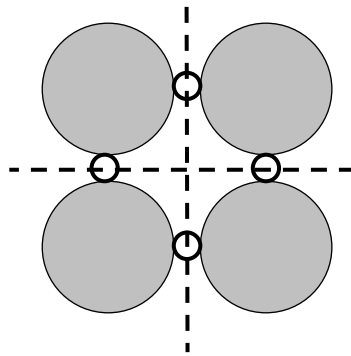


Figure 3.17: The inscribed pore throat located on the local minima on the medial axis on a cross section

Figure 3.18 graphically illustrates the overall process of creating pore body and throat data from the medial axis. Pore-throats are not shown in Figure 3.18.c, medial-axis paths are shown instead. After applying the merging algorithm discussed previously, each path corresponds to a pore-throat and its length is calculated as the length of the path connecting the centers of adjacent pore-bodies.

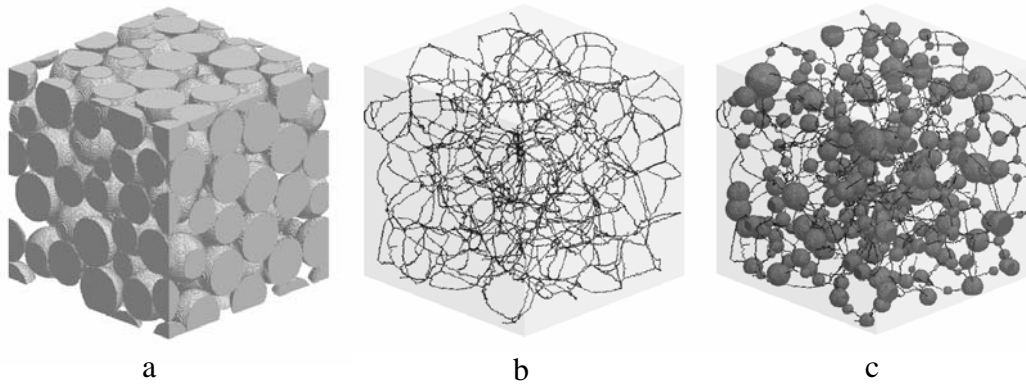


Figure 3.18: (a) Small random packing, (b) medial axis, and (c) location of pore-bodies on the media axis

### 3.9.4 Connectivity of the Pore Space

The connectivity of the pore space is a measure of the number of independent paths between two points and, hence of the degree of interconnectedness of the pore (Dullien, 1992). The connectivity has a critical influence on transport properties such as permeability and its quantification is important for understanding microstructure-transport property relationships (Wong, 1999). The connectivity is readily calculated from the medial axis as a form of coordination number of the system describing the average number of throats connected to each pore body.

### 3.9.5 Validation of the Algorithm

The algorithms of extraction pore-network structure are validated using three different theoretical systems, and results are compared to those obtained from the modified Delaunay Tessellation based approach (MDT). The MDT approach, an analytically-based method is described in Al-Raoush et al. (2002).

First, the algorithm is applied to a simple cubic packing that has uniform, equally-spaced pore bodies and throats. The second system is a rhombohedral packing that

produces two distinct pore body sizes (repeated throughout the regular structure). The third system is the same rhombohedral packing as before, but that is pixelized at a higher resolution. The fourth system is a theoretical random packing.

(1) The cubic packing consists of 512 spheres, digitized at 25 pixels per sphere diameter. The size of the three dimensional image is 200x200x200 pixels. The calculations are based on an interior volume of 175x175x175 pixels, where a sphere radius is cut out from each side to remove the boundary effects.

(2) The first rhombohedral packing consists of 512 spheres, digitized at 25 pixels per sphere diameter. The size of the three dimensional image is 200x173x163 pixels. The calculations are based on a volume of 175x148x138 where a sphere radius is cut out from each side to remove the boundary effects.

(3) The second rhombohedral packing consists of 512 spheres, digitized at 45 pixels per sphere diameter. The size of the three dimensional image is 364x315x297 pixels. The calculations are based on a volume of 319x270x252 where a sphere radius is cut out from each side to remove the boundary effects.

(4) The random packing consists of 1000 uniform spheres. For the medial-axis calculations, it is pixelized using a resolution of 25 pixels per sphere diameter. The original size of the 3D image is 250x250x250. After extracting pore network parameters, the domain is cropped from each side by an amount equal to a sphere radius to avoid the boundary effects. Thus, the network occupies a domain of size 200x200x200 pixels.

### 3.9.6 Pore Network Structure Correlation

#### 3.9.6.1 Semivariograms

Correlation aspects of the pore network structure include: body-body size correlation, body-throat size correlation, and average aspect ratio. Spatial correlation can be analyzed using variograms (or semivariograms). The semivariogram is used to find the rate at which a random function  $Z(x)$  changes along a specific direction. It shows how the dissimilarity between  $Z(x)$  and  $Z(x+h)$  evolves with a separation  $h$ .

The semivariogram is calculated as (Chiles and Delfiner. 1999):

$$\gamma(h) = \frac{\sum (Z(x) - Z(x+h))^2}{2n} \quad (3.20)$$

where  $n$  is the number of points separated by a lag  $h$ . For simplicity, the lag is assumed to be a jump between neighboring pores and the median throat length of the system is used as lag length. For a given lag, lag one for instance, the algorithm searches for all pore-bodies that are one throat apart (pore-bodies have to be connected by those throats) and equation 3.21 is calculated. For lag two, pore-bodies found in previous step(s) are removed from the list and the algorithm searches for all pore-bodies that are two throats apart (pore-bodies have to be connected by those throats), equation 3.21 is then recalculated. The algorithm progresses in the same way until it is stopped at a specified lag number or when all pore-bodies are removed from the list. A plot of  $\gamma(h)$  vs. the lag,  $h$ , is the semivariogram.

A sill and range characterize the semivariogram (Figure 3.19). The sill is a plateau in the semivariogram that corresponds to the variance of the sampled data. The range (the correlation length) is the distance at which a semivariogram reaches a plateau.

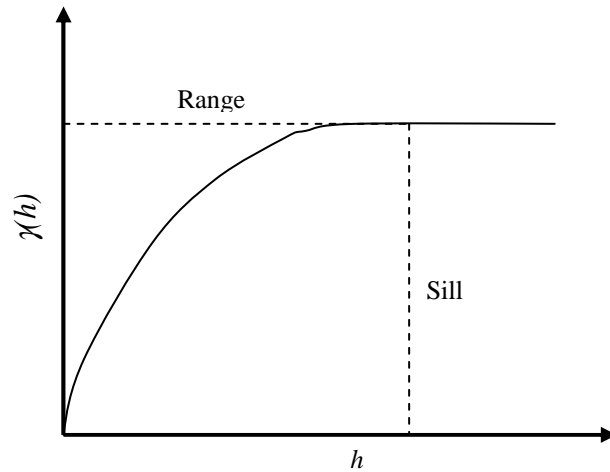


Figure 3.19 : A typical semivariogram

To minimize the effect of pixelization of pore body sizes (discrete sizes), a uniform distribution is assigned to each size class. In the pore network structure where the variation in neighboring pore-body sizes is large, the use of variogram can lead to a poor estimate of the regional correlation. Therefore, a robust variogram in which the variation between classes is reduced must be used. This is achieved by replacing the classes of the system (e.g. pore-body sizes) by two sets of classes, 0 and 1. The median is used as a threshold, where values above the median are set to 1 and values below the median are set to 0. Implementing this process in the variogram calculations is called indicator variogram (Chiles and Delfiner, 1999).

### 3.9.6.2 Integral Range

The correlation length and range are used to describe the same idea. However, they are not the same and each parameter is unique to the respective model (Jensen, 2000).

A quantity that also expresses the extent of correlation is the integral scale, defined as (Chiles and Delfiner, 1999):

$$I = \frac{\int_0^{\infty} [\sigma^2 - \gamma(h)] dh}{\sigma^2} \quad (3.21)$$

where  $\sigma^2$  is the variance.

In this research, integral scale is adopted as a tool to describe the correlation in the pore network.

### 3.9.7 Materials and Data Sets

Table 3.1 shows the materials and data sets used in this research. The glass beads of systems L\_B, M\_B, and S\_B were soaked in nitric acid (1 N) for approximately five hours, rinsed with deionized/distilled water, washed with acetone using a 2  $\mu\text{m}$  filter, rinsed again several times with deionized/distilled water in the filter, and then dried in an oven at 550  $^{\circ}\text{C}$  for 24 hours. The glass beads were packed into tubes using a funnel). O\_S\_1 and O\_S\_2 images are of a sediment sample collected in the Gulf of Mexico as part of a Naval Research Laboratory research project (Reed et. al., 2002). Each tube was filled in steps while tapping the side of the tube to ensure homogenous distribution of the particles. Three types of tubes were used in the glass beads scans, plastic tube for S\_B, plastic tube for P\_B\_1, and P\_B\_2 systems and plexiglass tube for X\_L\_B, L\_B, and M\_B systems. Table 3.1 shows the dimensions of these tubes.

Table 3.1: Materials and data sets

Sample Size (mm)	Name	Vendor (Source)	Location	Energy (Kev)	Column size (mm)	Image size (pixels)	Resolution (microns)
Glass bead D = 1.0	X_L_B	Jaygo, Incorporated	APS <sup>(1)</sup>	33.22	H=70.0 I.D=5.0 O.D=7.0	X=300 Y=300 Z =450	11.5
Glass bead D =0.4 – 0.6	L_B	Fisher Scientific	APS	33.22	H=70.0 I.D=5.0 O.D = 7.0	X=300 Y=300 Z =450	11.5
Glass bead D=0.30-0.25	M_B	McMaster- Carr Supply, Atlanta, GA	APS	33.22	H=70.0 I.D=5.0 O.D = 7.0	X=300 Y=300 Z =450	11.5
Glass bead D=0.25- 0.177	S_B	McMaster- Carr Supply, Atlanta, GA	CAMD <sup>(2)</sup>	13.0	H=30.0 I.D = 1.9 O.D = 2.5	X=250 Y=250 Z =114	9.0
Perfect glass bead D = 0.123	P_B_1	GlenMills Inc, Clifton, NJ	APS	22.0	H=100.0 I.D = 3.0 O.D=3.5	X=300 Y=300 Z =450	5.8
Perfect glass bead D = 0.123	P_B_2	GlenMills Inc, Clifton, NJ	APS	22.0	H=100 I.D =3.0 O.D=3.5	X=150 Y=150 Z =225	11.5
Ooid sand D <sub>50</sub> =0.325	O_S_1	Long Keys, Bahamas	APS	33.22	No sample holder	X=375 Y=400 Z =475	11.5
Ooid sand D <sub>50</sub> =0.325	O_S_2	Long Keys, Bahamas	APS	33.22	No sample holder	X=188 Y=200 Z =238	23.0

(1) Advanced Photon Source, Argonne National Laboratory, Chicago, IL

(2) Center for Advanced Microstructure and Devices, Louisiana State University, LA

## 4. Results and Discussion

### 4.1 Two-Dimensional and Three-Dimensional Images of the Experiments

This section shows cross-sectional and three-dimensional images of the systems described in Table 3.1 (Figures 4.1 – 4.8). The systems are gray scale images where the intensity values range from 0 to 255. Each three-dimensional image is shown with a cut-off from the corner to show the interior distribution of the sample. The quality of the image depends on factors such as the type of the material of the sample, the energy level, the sample size, and the resolution of the image. Figure 4.4 shows the system imaged at CAMD where the quality of the image is not as good as systems imaged at APS (Figures 4.1 - 4.3, 4.5 - 4.7). This is mainly due to low photon flux and energy of the beam available currently at CAMD (i.e., the energy is less than 13 KeV at CAMD compared to 33.2 KeV at APS).

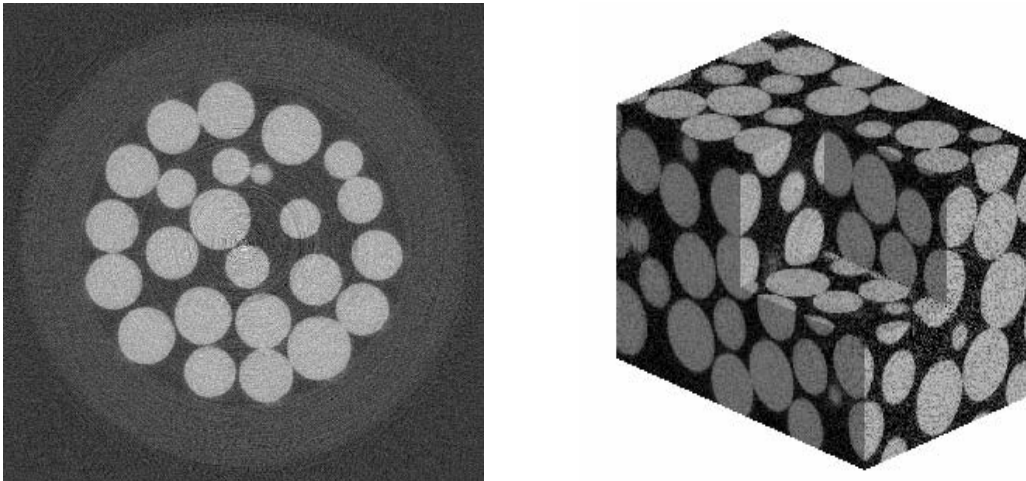


Figure 4.1: Cross-sectional and three-dimensional images of the X\_L\_B system

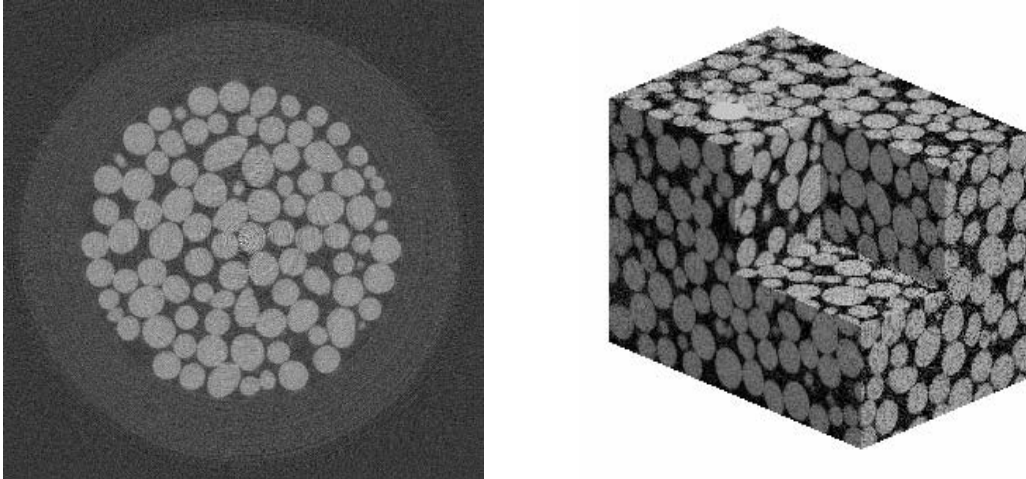


Figure 4.2: Cross-sectional and three-dimensional images of the L<sub>B</sub> system

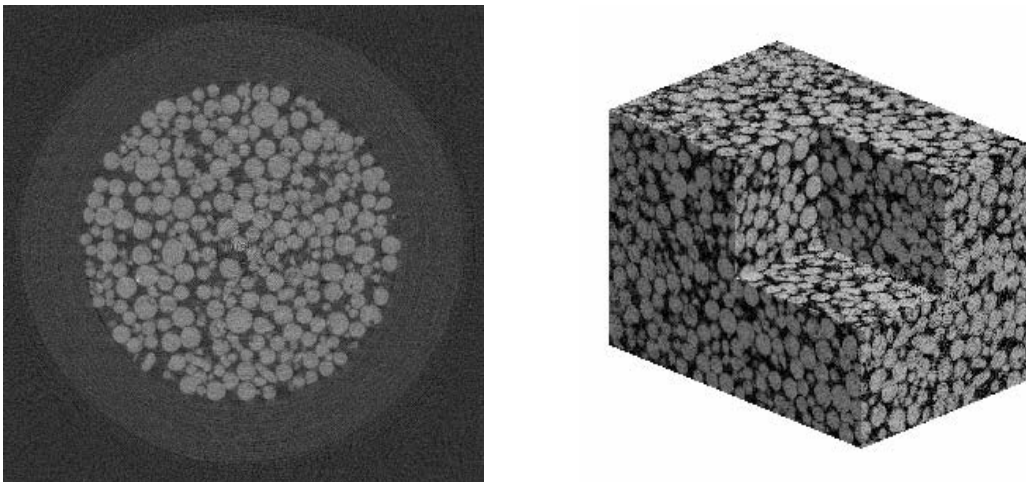


Figure 4.3: Cross-sectional and three-dimensional images of the M<sub>B</sub> system

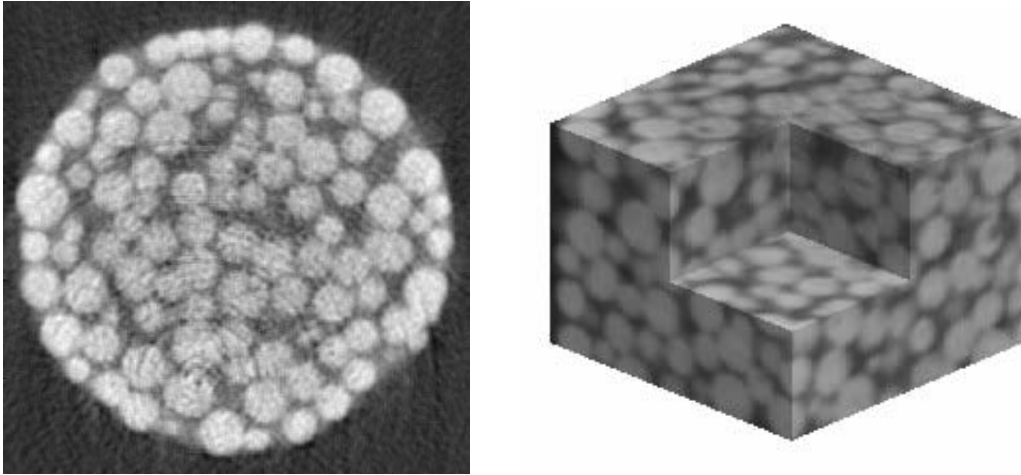


Figure 4.4: Cross-sectional and three-dimensional images of the S\_B system

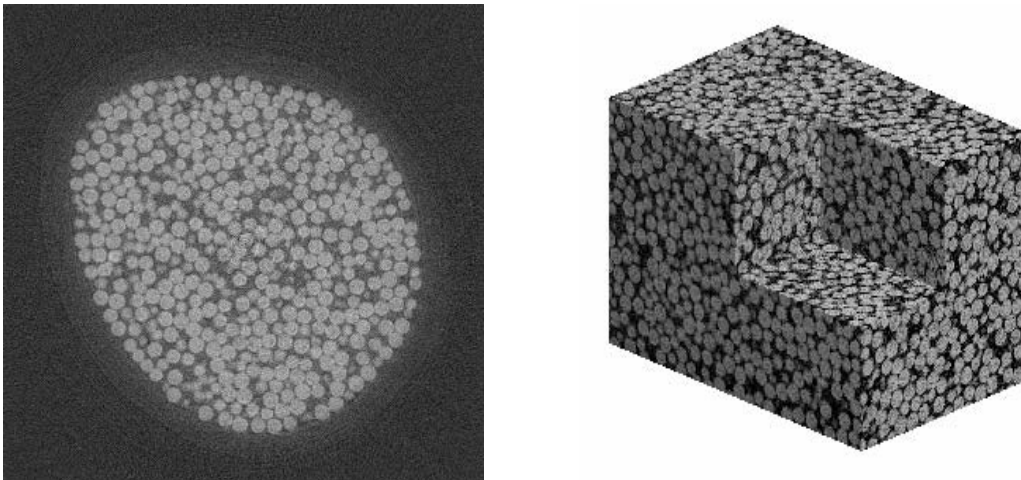


Figure 4.5: Cross-sectional and three-dimensional images of the P\_B\_1 system

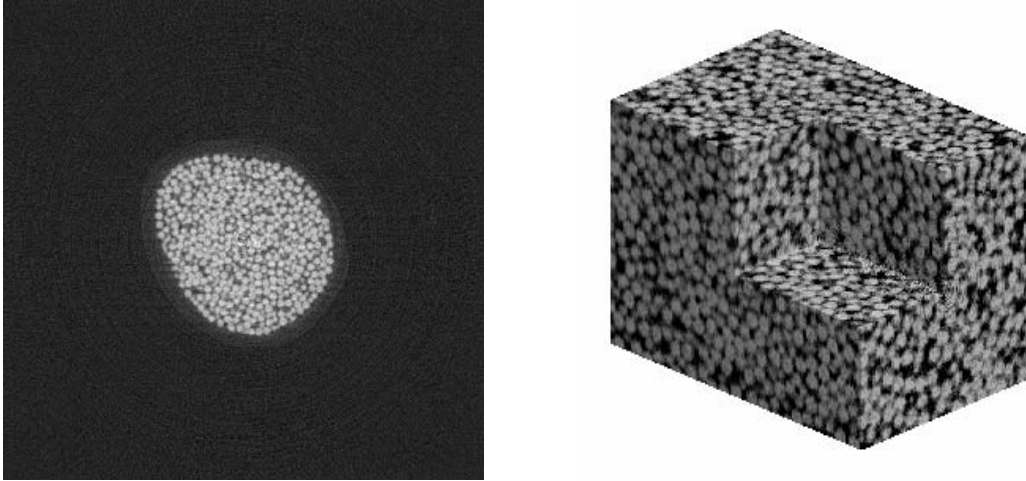


Figure 4.6: Cross-sectional and three-dimensional images of the P\_B\_2 system

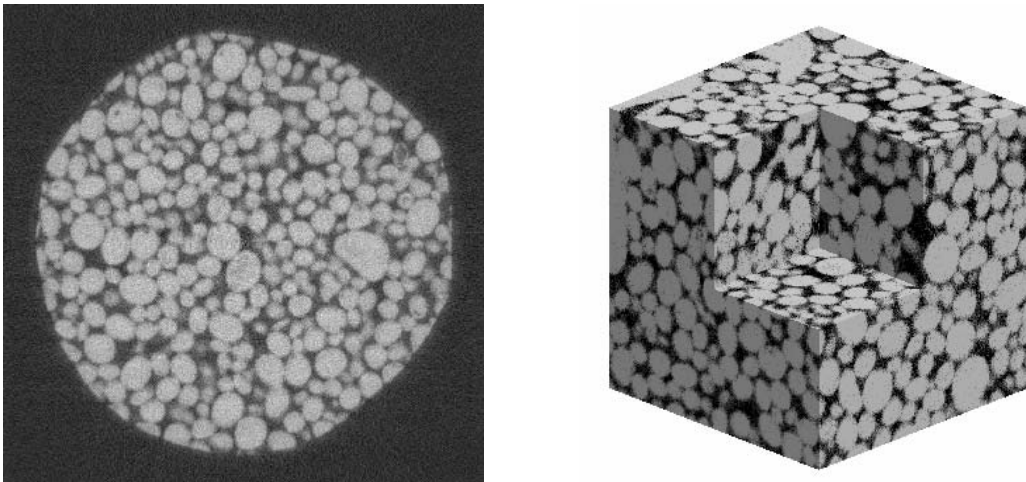


Figure 4.7: Cross-sectional and three-dimensional images of the O\_S\_1 system

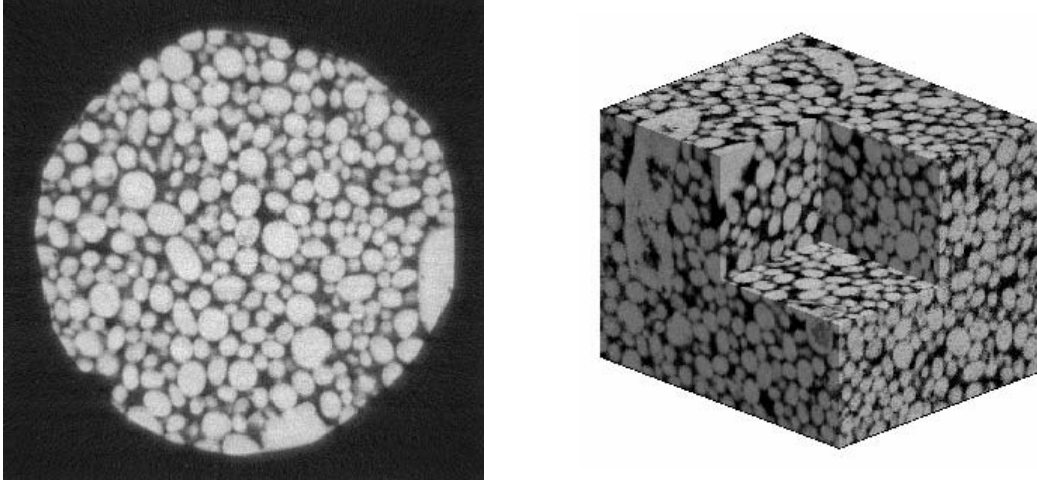


Figure 4.8: Cross-sectional and three-dimensional images of the O\_S\_2 system

#### 4.2 Two-Point Correlation Function (Porosity and Specific Surface Area)

This section provides two-point correlation function results (Figures 4.10 – 4.17). Calculations of porosity and specific surface areas are based on three-dimensional two-point correlation functions (section 3.8). To minimize wall effect on the packing and, consequently, the calculation of properties, an interior portion of the image was cut out and the calculations were based on this subvolume (given in Table 3.1). The wall effect becomes more profound if  $D_T / D_p > 10$ , where  $D_T$  is the diameter of container and  $D_p$  is the sphere diameter (Dullien,1992). Regions adjacent to the interior surface of the wall will have high porosity due to the discrepancy between the radii of the curvature between the wall and the particles. This effect is significant in X\_L\_B system where  $D_T / D_p = 10$ .

The algorithm was verified using regular packing (Table 4.1). Porosity for the close cubic packing obtained from this algorithm is 0.47 whereas the exact value is 0.4764. For the rhombohedral packing, the exact porosity is 0.2595 and the calculated

porosities are 0.196 and 0.271 for low and high resolution respectively. The difference between the exact and the calculated values is due to the pixelization of the spheres.

Calculations of specific surface area were verified by comparing the calculated and the exact values for a generated random 100-sphere pack (Figure 4.9). Each sphere has a diameter of 85 pixels and the size of the total domain is 375x375x375 pixels. The theoretical specific surface for this pack is  $0.043 \text{ pixel}^{-1}$  whereas the calculated one is  $0.0456 \text{ pixels}^{-1}$ . The slight difference can be attributed to pixelization of the spheres.

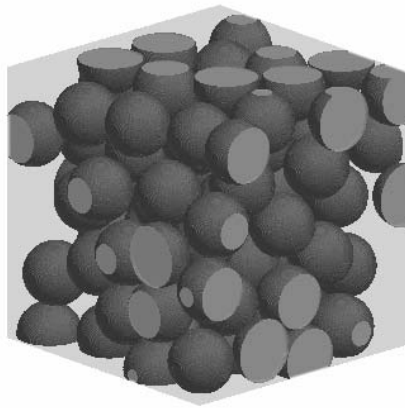


Figure 4.9 : A uniform 100-sphere random packing used to verify calculations of specific surface area

Porosity values for glass bead systems except P\_B\_2 ranges from 0.3708 to 0.4184. P\_B\_2 system was imaged at low resolution to investigate the impact of resolution on the calculated properties as will be discussed later. Based on these porosities, the packing of the systems can be divided to the following categories (Dullien, 1992):

(1) Close random packing (porosity range from 0.359 to 0.375): This packing is obtained when the system is shaken very well. The S\_B system ( $D = 0.25 - 0.177 \text{ mm}$ ) falls in this

category. Note that S\_B system doesn't have a REV, so categorizing this system under this type of packing is limited to this particular sample.

(2) Poured random packing (porosity range from 0.375 to 0.391): This packing is obtained when the beads are poured into container and shaken gently. System L\_B (D = 0.4 – 0.6 mm) falls in this category.

(3) Loose random packing (porosity range from 0.4 to values around 0.41): This type of packing is obtained by pacing the spheres so that they roll individually into a container. Systems X\_L\_B (D = 1.00 mm), M\_B (D = 0.3 - 0.25 mm), and P\_B\_1 (D = 123 micron) fall in this category. Note that X\_L\_B system doesn't have a REV, so categorizing this system under this type of packing is limited to this particular sample.

As expected, specific surface areas increase as the size of the spheres decrease. Errors in calculating specific surface areas from images include the noise of the image, the resolution of the image and the segmentation process.

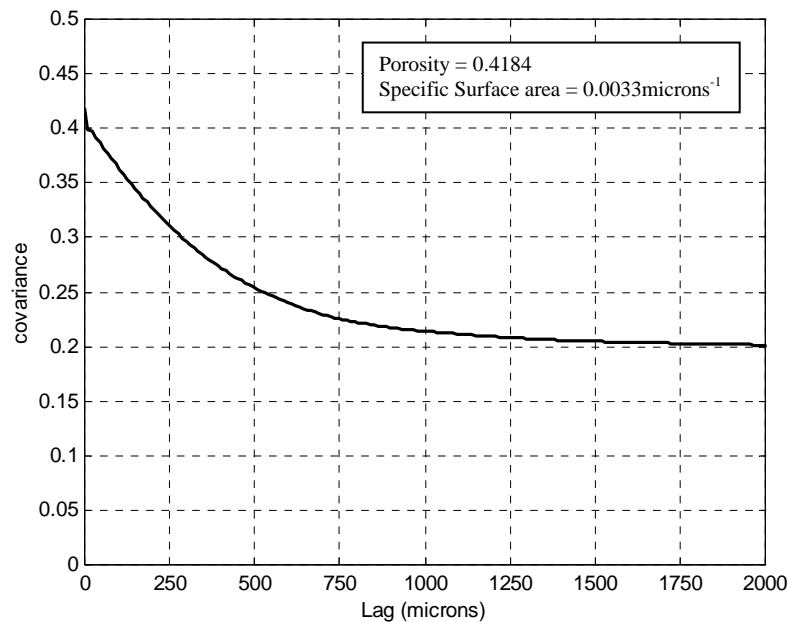


Figure 4.10: Two-point correlation function of the X\_L\_B system

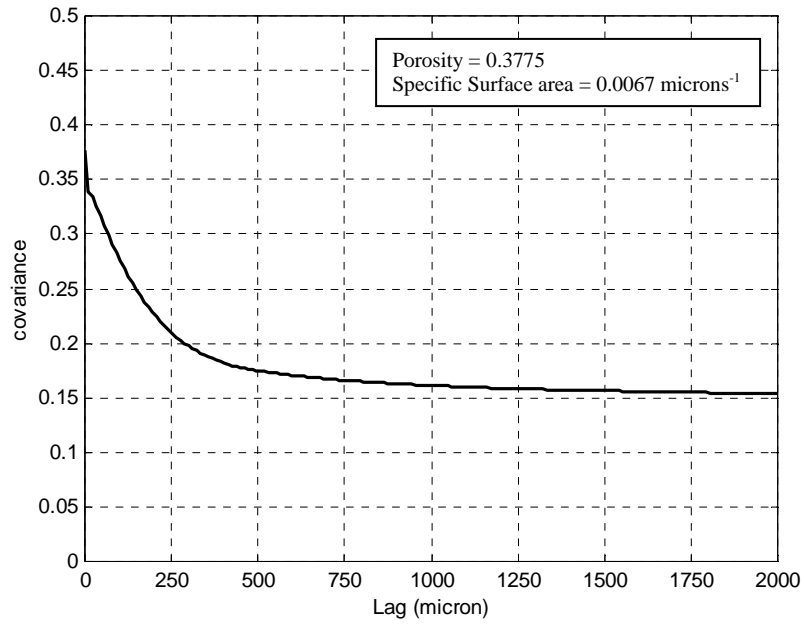


Figure 4.11: Two-point correlation function of the L\_B system

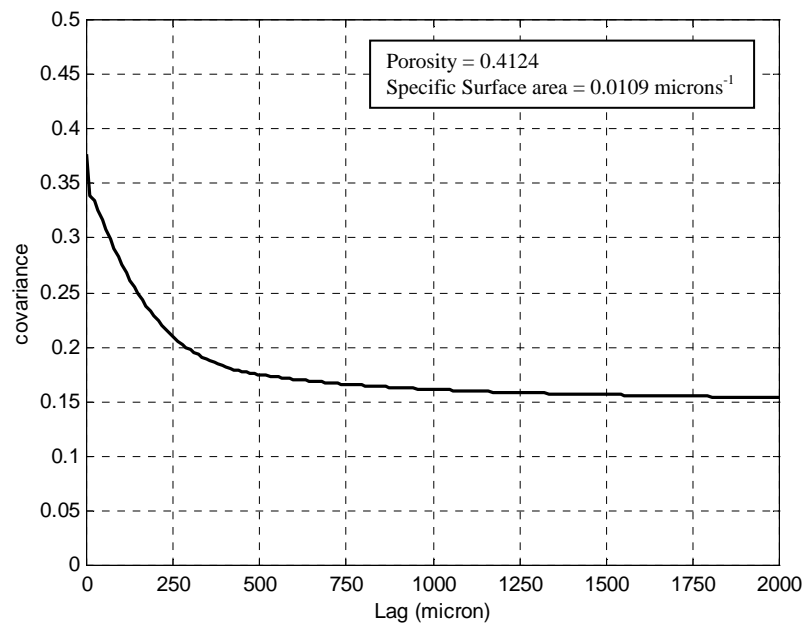


Figure 4.12: Two-point correlation function of the M\_B system

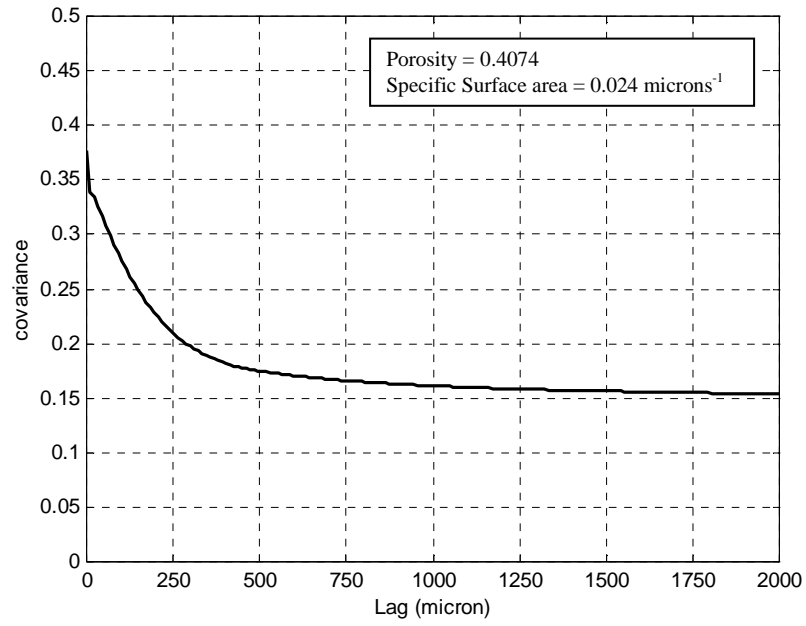


Figure 4.13: Two-point correlation function of the S\_B system

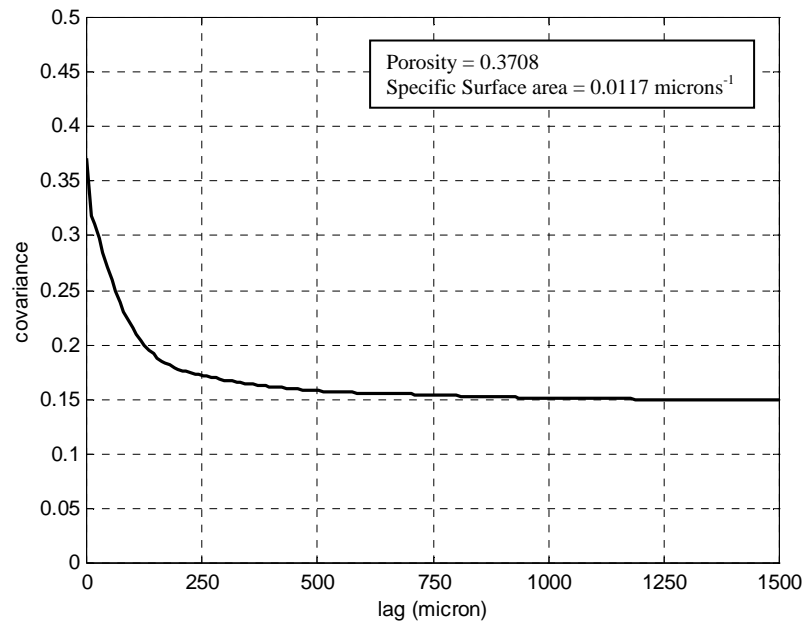


Figure 4.14: Two-point correlation function of the P\_B\_1 system

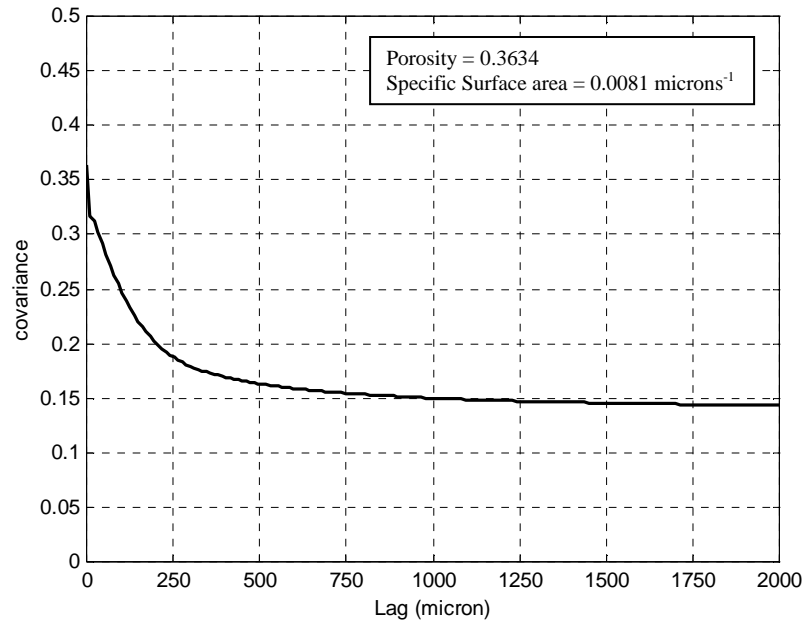


figure 4.15: Two-point correlation function of the P\_B\_2 system

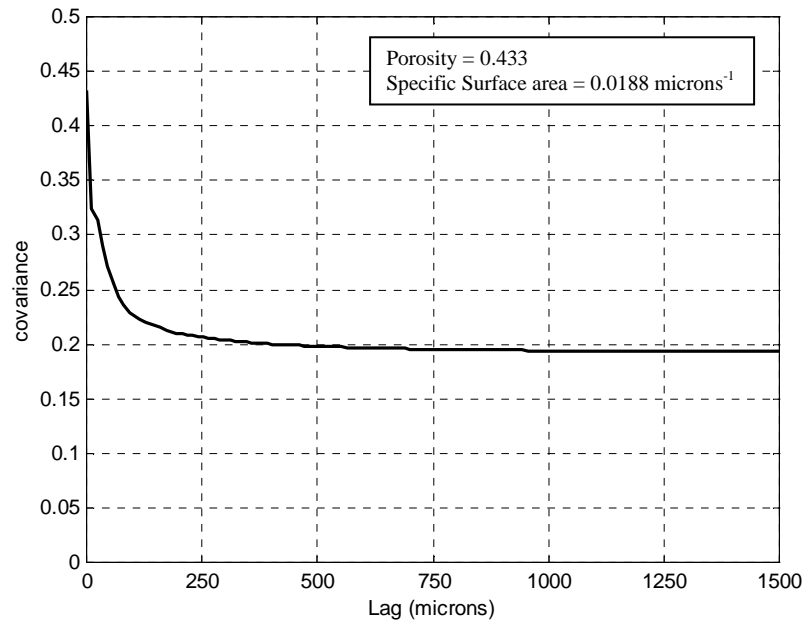


Figure 4.16: Two-point correlation function of the O\_S\_1 system

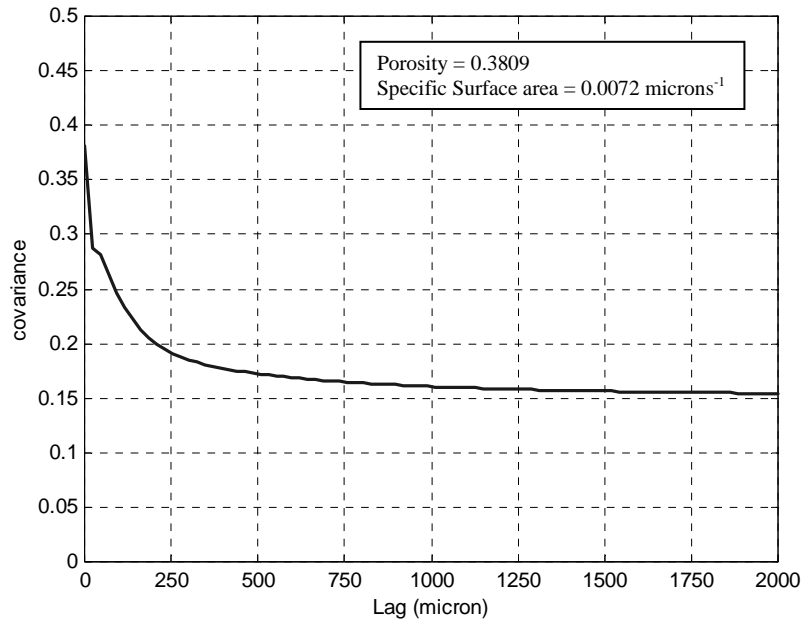


Figure 4.17: Two-point correlation function of the O\_S\_2 system

### 4.3 Representative Elementary Volume Analysis (REV)

Figures 4.18 – 4.25 show these results. All systems except X\_L\_B and S\_B systems (Figures 4.18 and 4.21) have REV for porosity within the imaged volume. A strong oscillation behavior is noticed in system X\_L\_B where the minimum REV is not approached for this system (Figure 4.18). Neither system has REV for porosity because the diameters of the particles are relatively large compared to the inside diameter of the column. REV findings agree with findings of Clausnitzer and Hopmans (1999) where they found that the side length of REV was approximately 5.15 times the bead diameter for a mono-size bead system. While the diameter of the glass bead in X\_L\_B system is 1.0 mm, the image size is 300x300x450 pixels, this is equivalent to a side length of 343.4 pixel and 3.95 mm at resolution of 11.5 micron. The ratio of the side length of the image obtained over the particle size is less than 5.15. For the S\_B system, the image size is

250x250x114 and the equivalent side length of 1.73 mm at 9 micron resolution. The system doesn't have an REV although the ratio of side length of the image over the particle diameter ( $d_{50}=0.214$  mm) is larger than 5.15. This is mainly due to the non-uniformity of the system (i.e., mixture of sizes). This agrees with the fact that a larger volume is required to obtain REV for non-uniform systems.

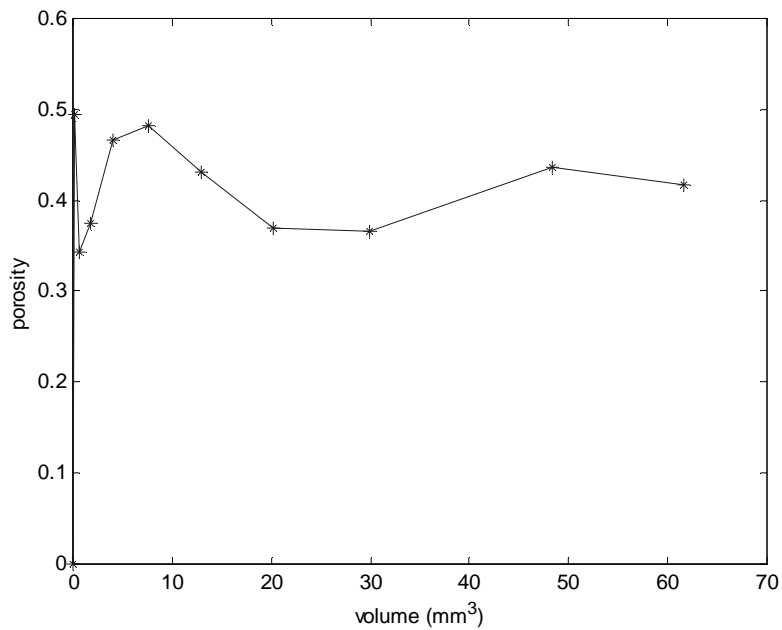


Figure 4.18: REV analysis of X\_L\_B system

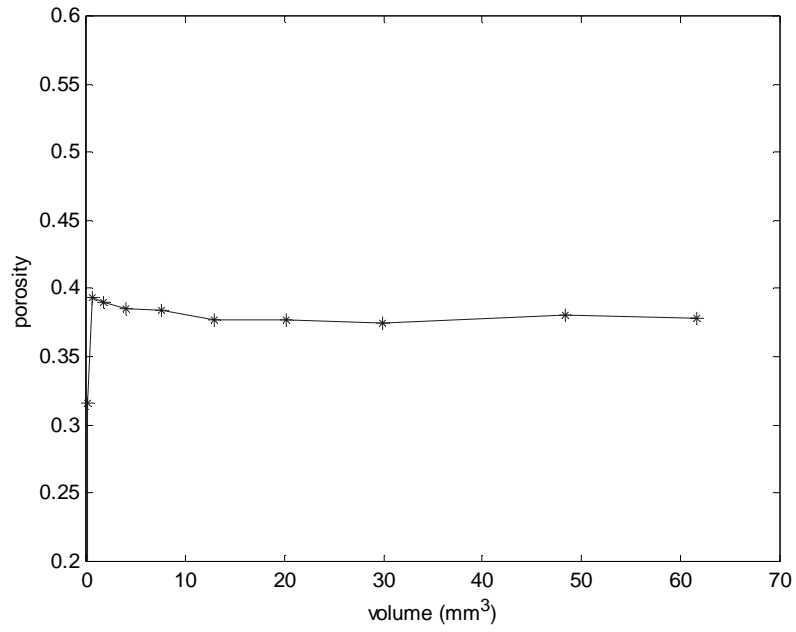


Figure 4.19: REV analysis of the L\_B system

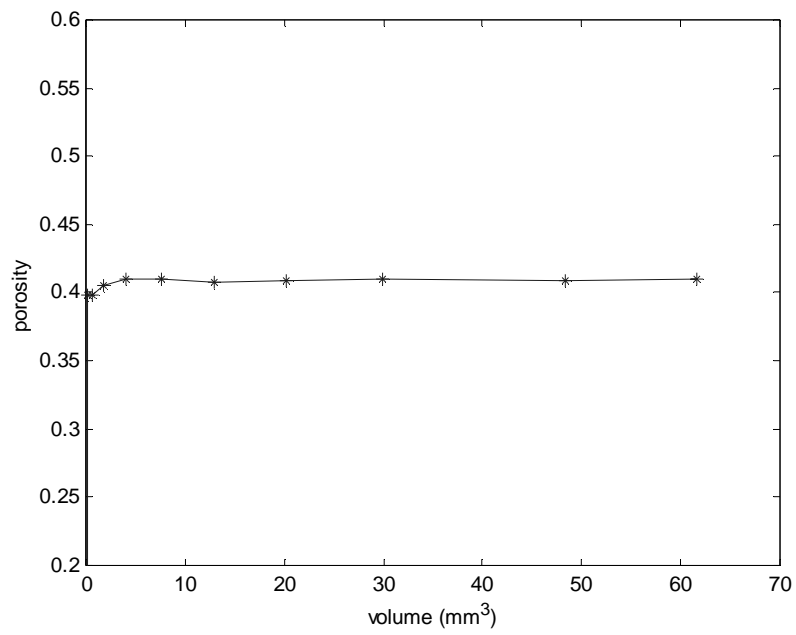


Figure 4.20: REV analysis of M\_B system

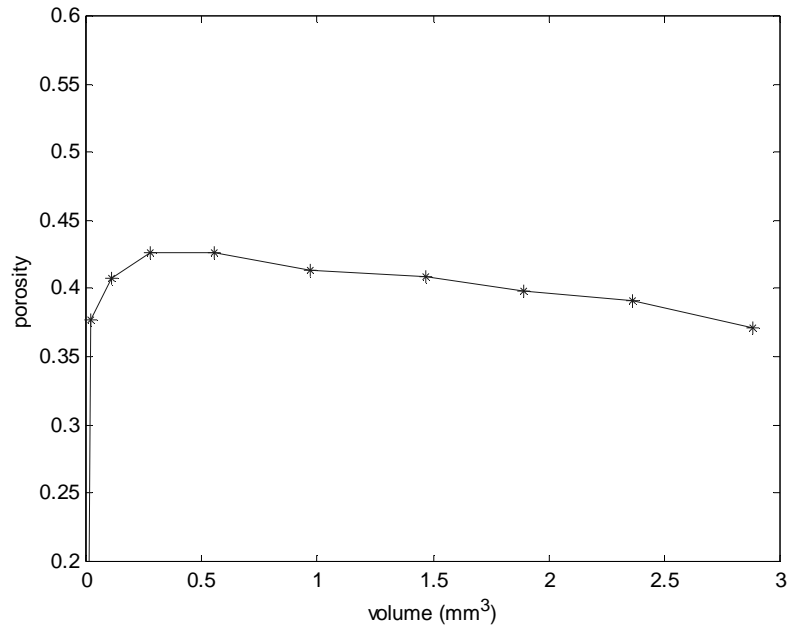


Figure 4.21: REV analysis of S\_B system

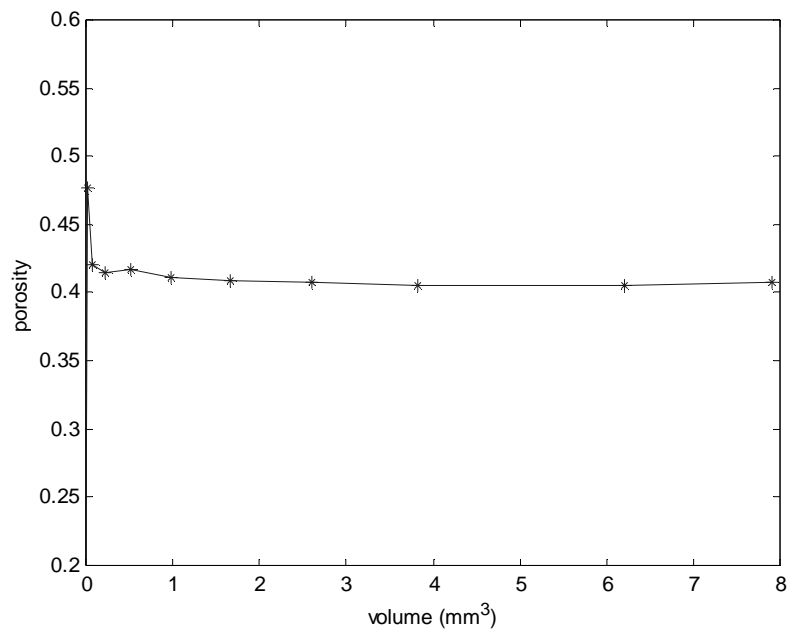


Figure 4.22: REV analysis of P\_B\_1 system

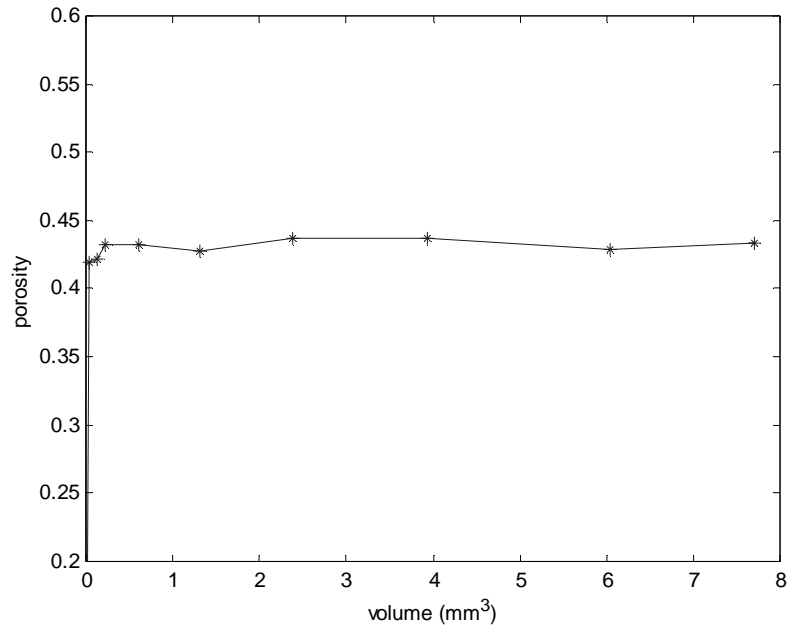


Figure 4.23: REV analysis of P\_B\_2 system

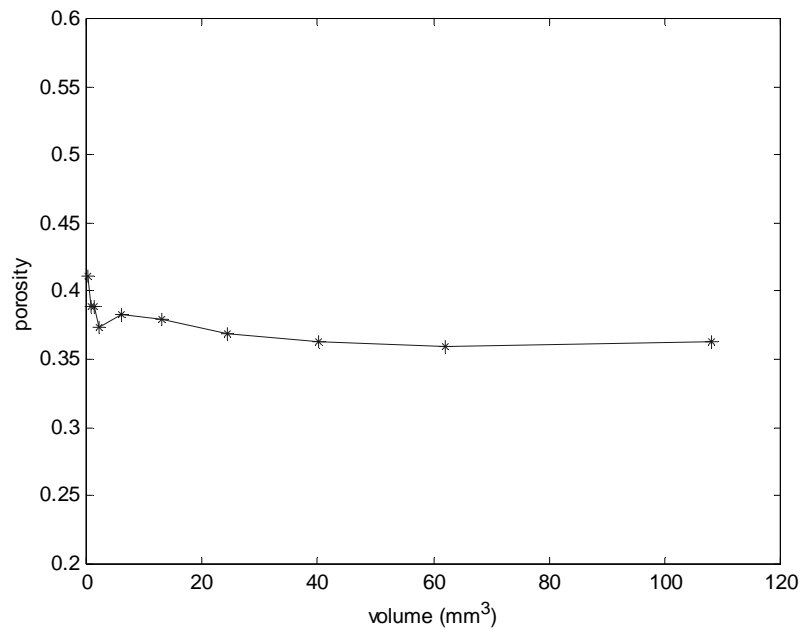


Figure 4.24: REV analysis of O\_S\_1 system

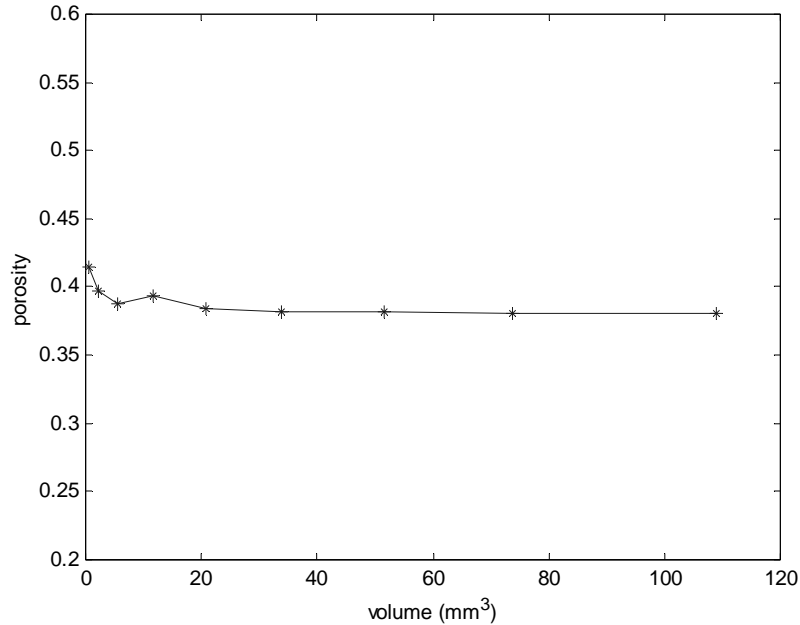


Figure 4.25: REV analysis of O\_S\_2 system

## 4.4 Extraction of Pore-Network Structure

### 4.4.1 Validation of the Algorithms

Figure 4.26 shows three-dimensional images of the cubic and rhombohedral packings described in section 3.9.5 and the location of the pores in these systems (The lighter spheres are the packing; darker spheres are the inscribed spheres denoting pore locations). Figure 4.27 shows three-dimensional cut-outs of the random packing and the pore bodies obtained from both network generation methods.

Table 4.1 shows the comparison between the two approaches (i.e., the medial-axis based (MA) and the MDT). Two pores from both methods are considered to be matched if they overlap. Note that this is the same criterion used for merging pores in both approaches. Table 4.2 shows the comparison between MA and MDT approaches based on a random packing. The merging criteria for merging pore bodies in the random packing is the same criteria used to test the matches in the regular packings.

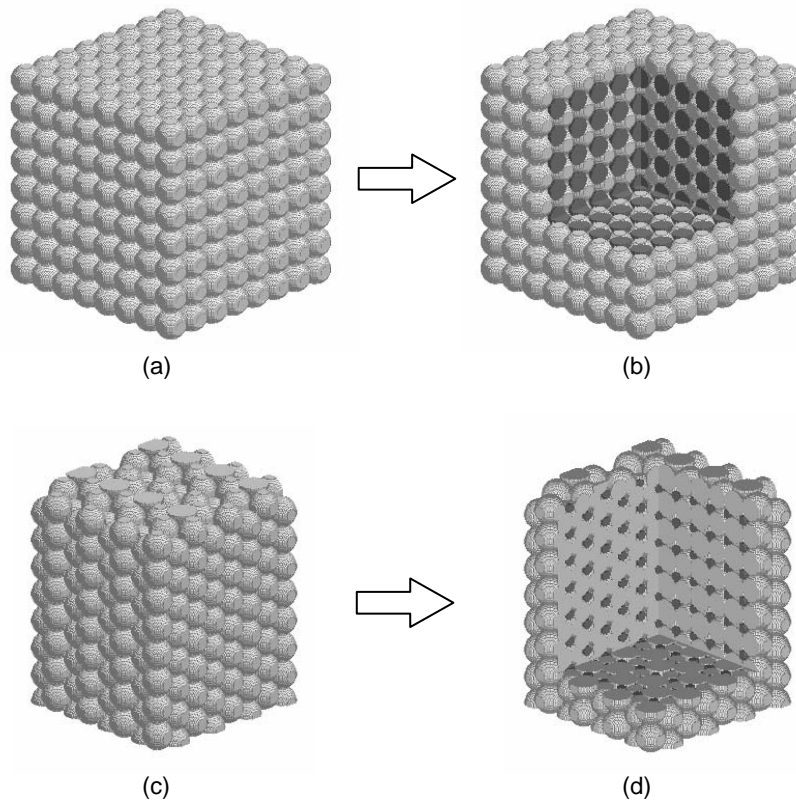


Figure 4.26: (a) 512–sphere cube packing, (b) location of the pores in the cubic packing, (c) 512-sphere rhombohedral packing, and (d) locations of the the pores in the rhombohedral packing.

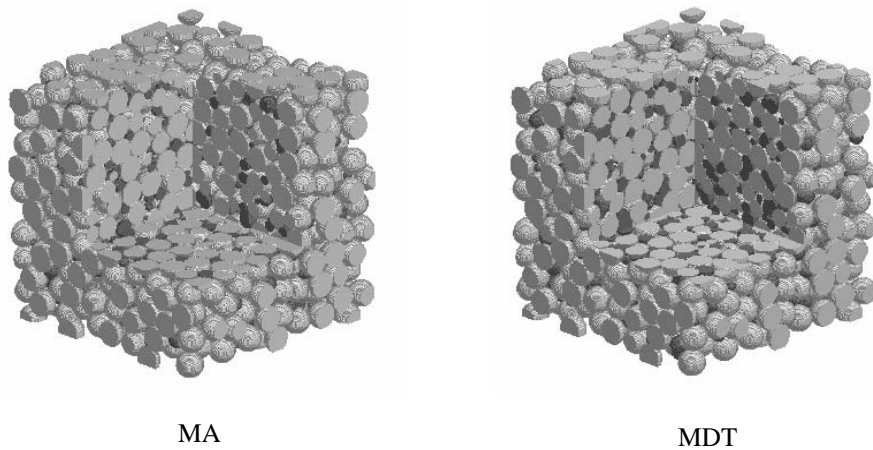


Figure 4.27: Uniform random packing and the locations of pore bodies from both methods

For the cubic packing, there is a good agreement between the two methods. The slight differences in the locations and radii of the pores from both methods are due to the fact that the MDT-based parameters are obtained directly from the actual locations of the “solid” spheres, while the MA-based parameters are obtained from a pixelized representation of the system. There is also a good agreement in the case of the rhombohedral packing for both high and low resolutions. Figure 4.28 shows the distribution of the distances between matched pores for the two resolutions. It is obvious that as the resolution increases, the distance between the centers of the matched pores decreases. In the medial axis based method, the radius of a pore is very sensitive to the calculated location of that pore because the radius is obtained by a dilation algorithm starting from the center of the pore (i.e., the node location) to the closest surrounding solid space. As mentioned earlier, a node in the medial axis can be made up of several voxels in which the same local maximum was identified. Therefore, the issue of which voxel to choose as the pore center can lead to errors in calculating the radius of the pore body at that location. It should be noted that in the rhombohedral packing with high resolution (Table 4.1) there are relatively few pore throats (21 throats) with a radius of one pixel. These throats should belong to the group of throats that have a radius of two pixels; the error ultimately stems from the pixelization of the original spheres. This observation illustrates one of the significant problems in dealing with a digitized image of a continuum pore space. Also note, however, that the average throat radius becomes closer to the tessellation value at the higher resolution, indicating that higher resolutions do indeed improve the description in an average sense.

Table 4.1: Comparison between medial axis (MA) and Delaney tessellation (DT) based approaches on theoretical packings.

	<b>Cubic Packing<sup>(1)</sup></b>		<b>Rhombohedral<sup>(2)</sup></b>		<b>Rhombohedral<sup>(3)</sup></b>	
<b>Method</b>	<b>MA</b>	<b>MDT</b>	<b>MA</b>	<b>MDT</b>	<b>MA</b>	<b>MDT</b>
<b>Pore Properties</b>						
Number of pores	343	343	871	871	871	871
Number of matches	343		871		871	
Max. inscribed radius (pixels)	9.0	9.13	4.0	5.17	10.0	9.4
Min. inscribed radius (pixels)	9.0	9.13	1.0	2.8	3.0	5.1
Ave. inscribed radius (pixels)	9.0	9.13	2.62	3.59	5.7	6.5
Distance between matched pores from each method (center to center) (min/max/ave) (pixels)	1.00 : 1.00 : 1.00		0.0 : 3.32 : 1.7		0.0 : 5.0 : 2.19	
<b>Throat properties</b>						
Max. coordination number	6	6	8	8	8	8
Min. coordination number	6	6	3	4	4	4
Avg. coordination number	6	6	5.22	5.4	5.3	5.4
Max. inscribed radius (pixels)	4.0	5.2	3.0	1.93	5.0	3.52
Min. inscribed radius (pixels)	4.0	5.2	1.0	1.93	1.0	3.52
Ave. inscribed radius (pixels)	4.0	5.2	1.58	1.93	3.76	3.52

(1) Diameter of spheres = 25 pixels, 3D size = 175x175x175 pixels

(2) Diameter of spheres = 25 pixels, 3D size = 175x148x138 pixels

(3) Diameter of spheres = 45 pixels, 3D size = 319x270x252 pixels

Table 4.2: Comparison between medial axis (MA) and modified Delaney tessellation (MDT) based approaches on random packing

<b>Method</b>	<b>MA</b>	<b>MDT</b>
Number of pore bodies	1980	1838
Number of matches	1039	1124
% Matches	66.7	73.61
% of void space	17.22	29.21
% aspect ratio > 0.9	28.1	6.0
% aspect ratio > 0.8	29.8	18.8
% aspect ratio > 0.7	39.39	34.8
Max distance apart	16.7	
Min distance apart	0.0	
Avg. distance apart	5.26	
Max. coordination number	7	16
Min. coordination number	2	2
Avg. coordination number	3.7	5.54
Max. pore body radius (pixels)	12	11.43
Min. pore body radius (pixels)	1.0	2.86
Avg. pore body radius (pixels)	4.14	5.15

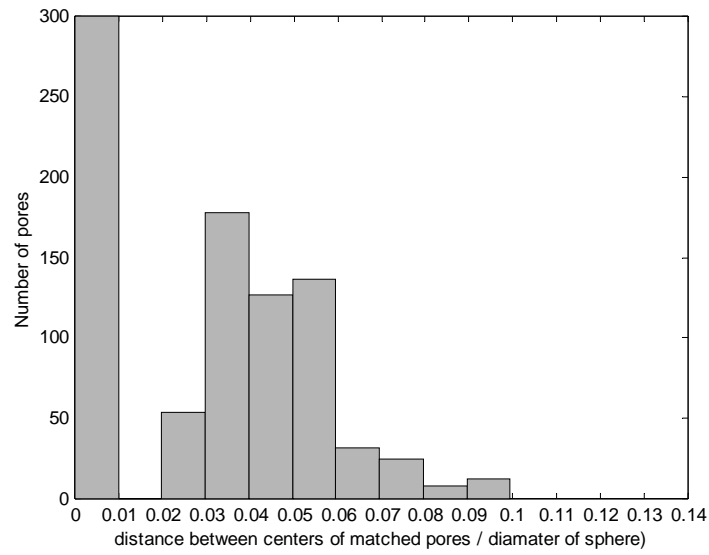
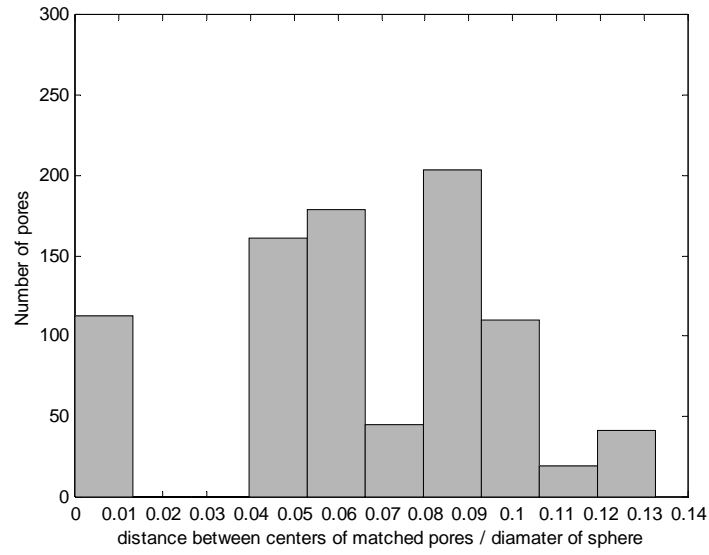


Figure 4.28: Distance distribution for the Rhombohedral packing, upper figure (diameter of spheres = 25 pixels), lower figure (diameter of spheres = 45 pixels)

In the following figures, which are images of pore cross sections, the gray spheres are the grains, the dashed lines are the pore bodies obtained from the MDT-method, and the solid lines are the pore bodies obtained from the MA- method. In the cases shown in Figure 4.29, the pore bodies are considered to be a good match because of their overlap.

Two different situations are illustrated in Figure 4.29. First, a case where both methods define two pores within the void space shown (pores from each method did not get merged because there is no overlap). Second, both methods define only a single pore in the void space. On the other hand, Figure 4.30 illustrates a situation where there is no match between the pore bodies defined by the respective methods. While each method correctly represents the pore body at the local minima, the fact that there is no overlap between pores from both methods classifies this case as non-match. This situation explains two features appearing in Table 4.2. First, there are approximately 30% non-matches from each method. Second, there is a discrepancy in the percentage of the void space occupied by pore bodies produced by each method.

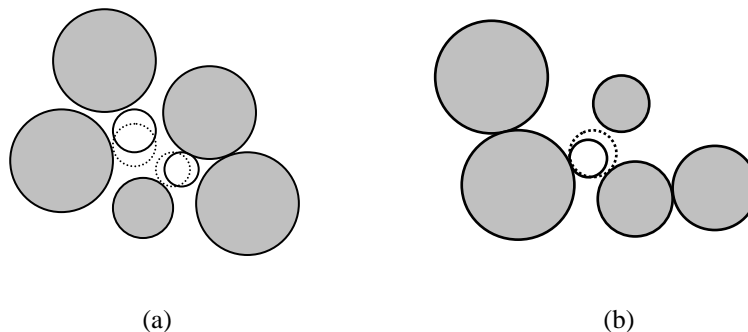


Figure 4.29: A case of match between pore bodies from MA and MDT methods

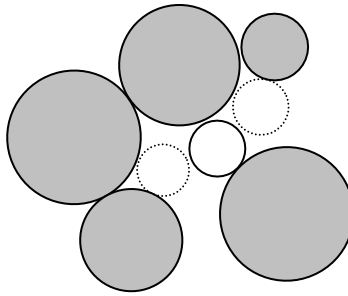


Figure 4.30: A case where there is no match between pore bodies from MA and MDT methods

Figure 4.31 shows the distribution of distances between the centers of the matched pore bodies from the two methods. The large distances are associated with matches between large pore bodies from both methods. The number of pore bodies from both methods that are separated by a distance larger than 10 pixels (i.e., 0.2 sphere diameter) is 156 pore bodies, or approximately 15%.

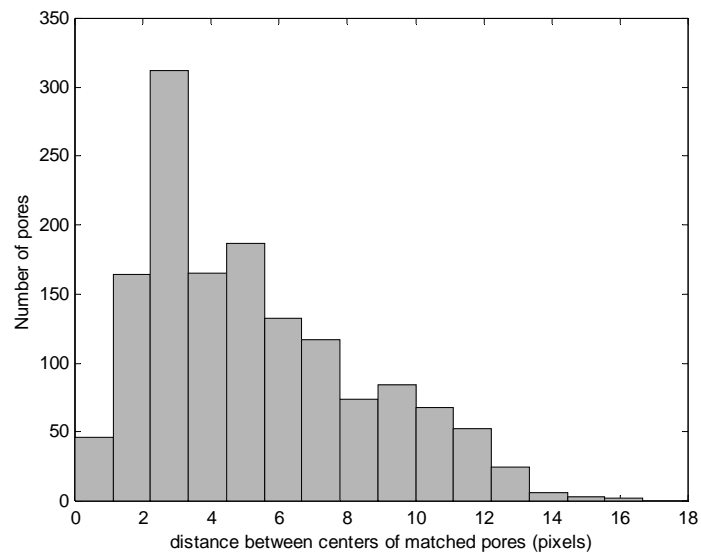


Figure 4.31: Distribution of the distance between the centers of matched pore bodies

#### 4.4.2 Pore-Network Structure Properties

This section summarizes results of the pore-network structure of the systems studied in this research (Table 3.1). Properties include, location of pore-bodies, location of pore-throats, pore-body size distribution, pore-throat size distribution, average coordination number of the system (coordination number of each pore-body is calculated by counting the number of throats connected to that pore-body and the average coordination number of the system is considered as the average coordination number of all pore-bodies), and average aspect ratio of the system (average aspect ratio of each pore-body is calculated and then the average aspect ratio of the system is considered as the average aspect ratio of all pore-bodies). Figure 4.32 shows three-dimensional and cross-sectional images depicting the locations of the pore bodies in the P\_B\_1. The glass beads are red and the pore bodies are depicted by the green spheres. The pore throats are not shown in the image for the sake of clarity.

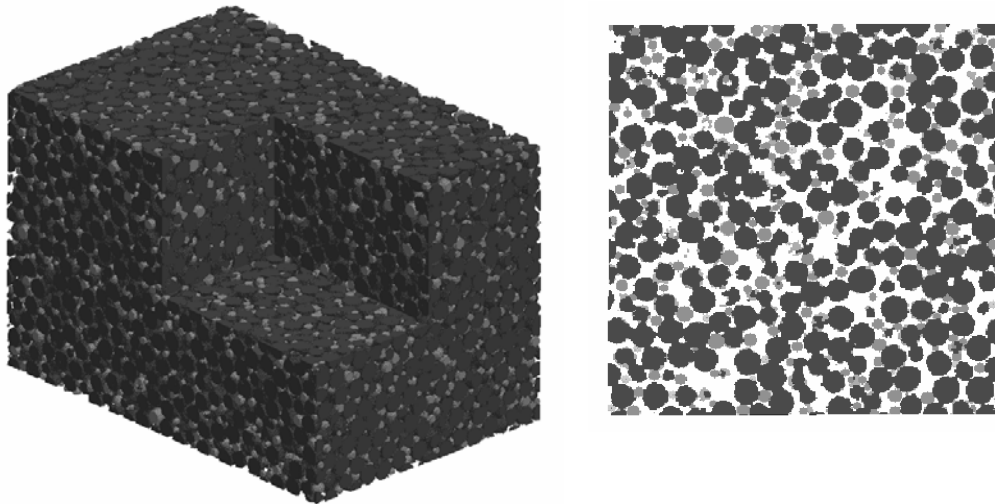


Figure 4.32: Three-dimensional and cross-sectional images show pore-body locations in P\_B\_1 system

Figure 4.33 shows a three-dimensional visualization of the pore network structure obtained from P\_B\_1 system. It should be mentioned that this research extracts the pore network structure in a form as shown in Figure 4.33.

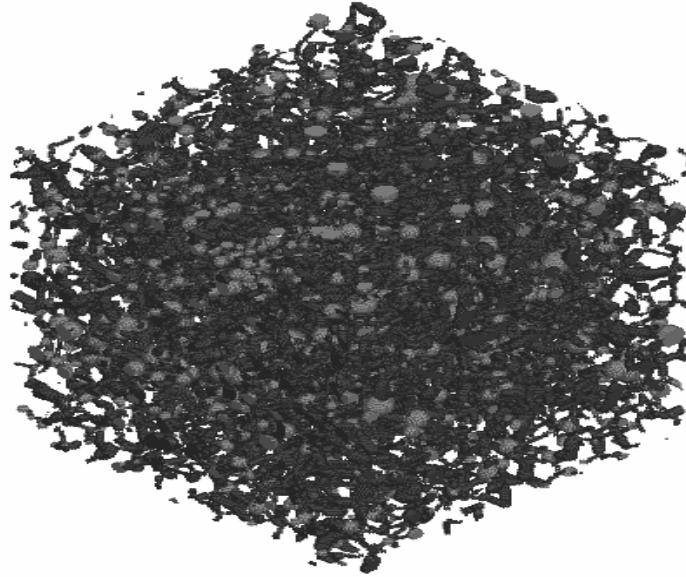


Figure 4.33: An example of three-dimensional pore-network structure obtained from P\_B\_1 system

Figures 4.34 – 4.41 show the pore-body and pore-throat size distributions for experiments X\_L\_B, L\_B, M\_B, and S\_B. These figures also show information about the distributions, i.e., the number of pores/throats, the maximum value, the minimum value, the average value, the coordination number, and the average aspect ratio. Note that the minimum size that can be determined is limited by the image resolution. It should be emphasized that the pore-network structure extraction algorithms developed in this research do not provide distributions of the sizes only; they also provide spatial three-dimensional distribution of the locations of pore-bodies and their connectivity.

The coordination number is calculated by calculating the average number of throats per pore-body and averaging of the entire system. Nodes on the medial axis that are connected to two paths are removed from the nodes list and considered as part of the medial axis. Therefore, the minimum coordination number in any system is 3. Very high coordination numbers are obtained when pore-body sizes and pore-throats lengths approach the resolution of the image. The coordination number ranges from 3.2 for X\_L\_B system (D=1.0 mm) to 5.17 for the L\_B system (D= 0.4- 0.6 mm), these values agree with the values documented in the literature (Dullien, 1992). There is no direct relation between the porosity and the coordination number of the systems investigated. Pore-size distributions obey different distribution and there is no general trend for the distributions. The coordination number ranges from 3.2 for X\_L\_B system (D=1.0 mm) to 5.17 for the L\_B system (D= 0.4- 0.6 mm). The aspect ratios range from 0.314 to 0.787. The average pore-body size of the systems is in the order of one-fourth of the  $d_{50}$  of the grains.

These results indicate that the morphology of the pore-space of system, even for similar types of systems, is different. Therefore, it is necessary to capture the exact morphology of the pore space to be partitioned into pore-network model elements. It is this morphology that when combined with the pore-space properties create a physically-realistic pore network structure.

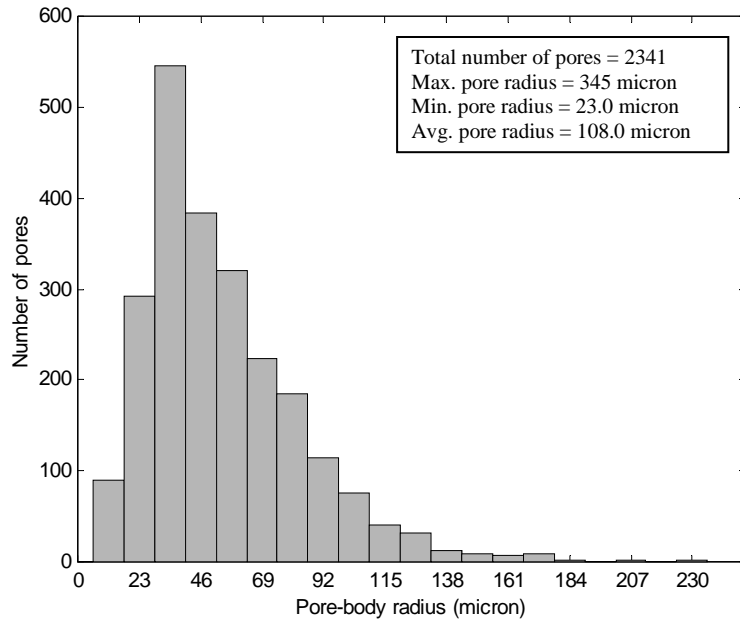


Figure 4.34: Pore-body properties of X\_L\_B system

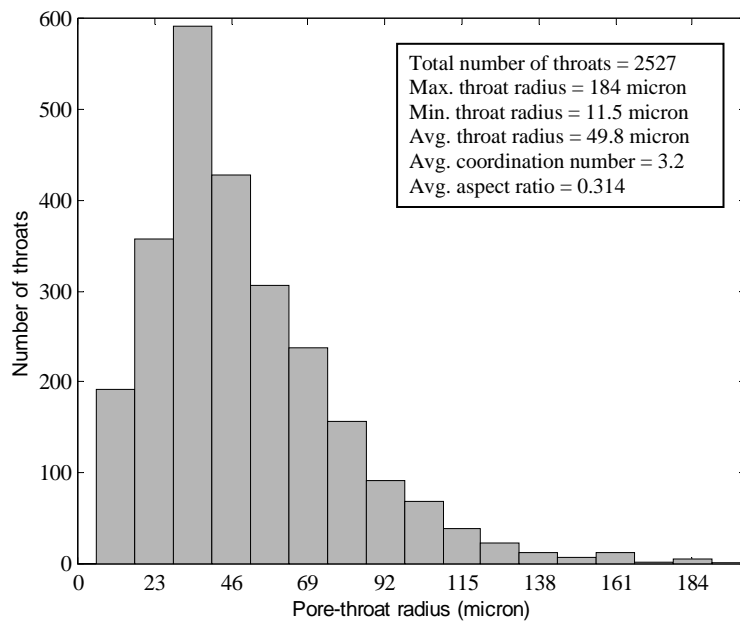


Figure 4.35: Pore-throat properties of X\_L\_B system

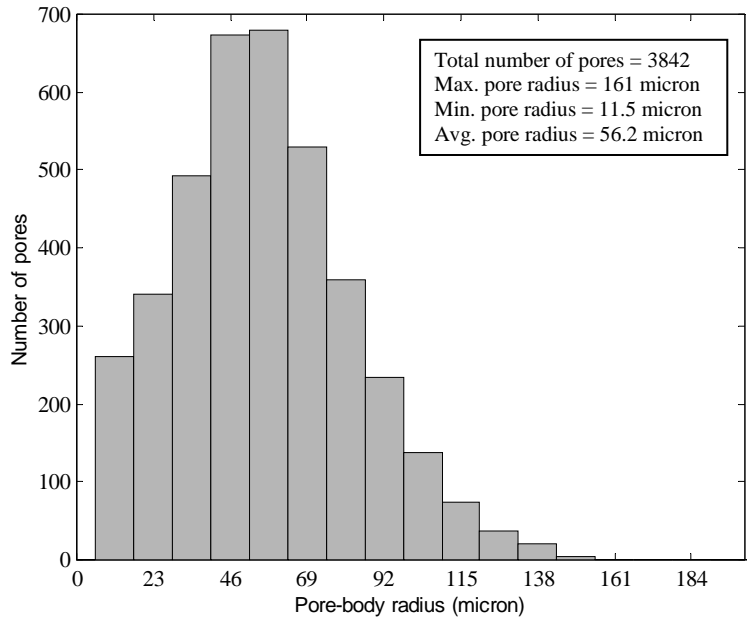


Figure 4.36: Pore-body properties of L\_B system

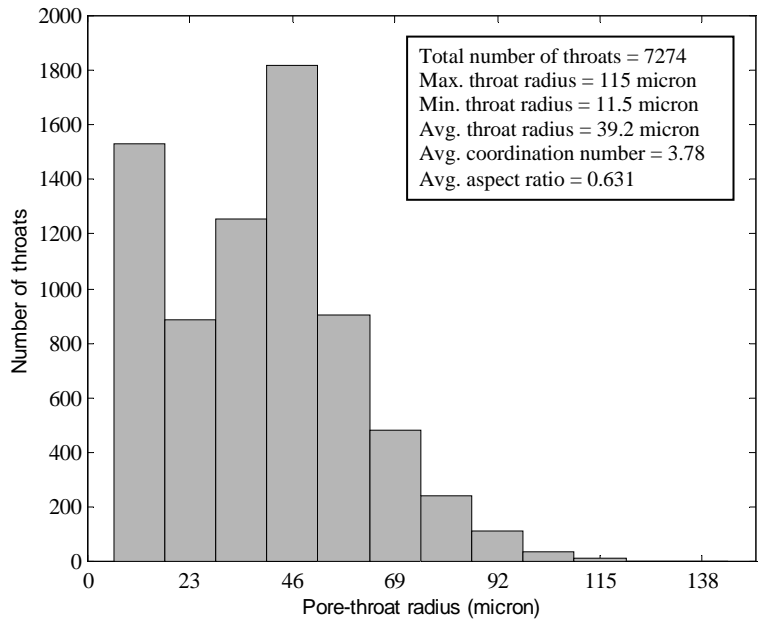


Figure 4.37: Pore-throat properties of L\_B system

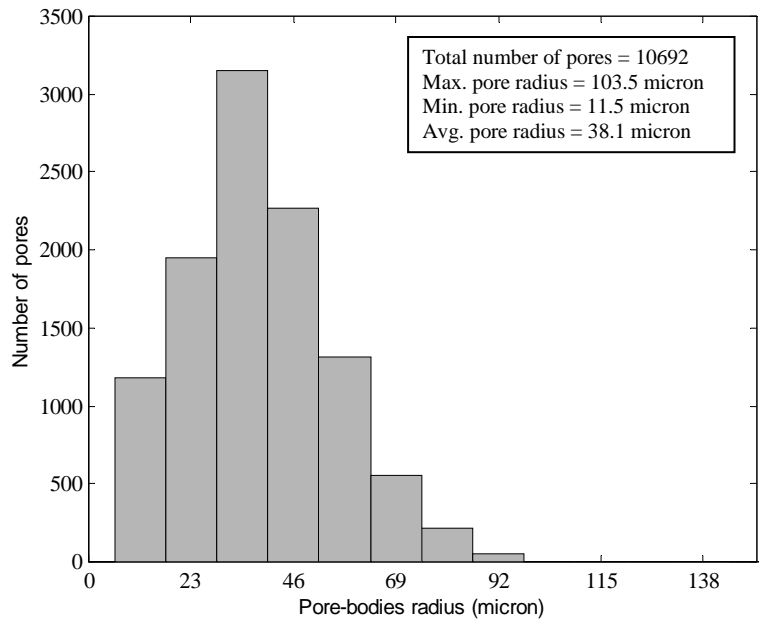


Figure 4.38: Pore-body properties of M\_B system

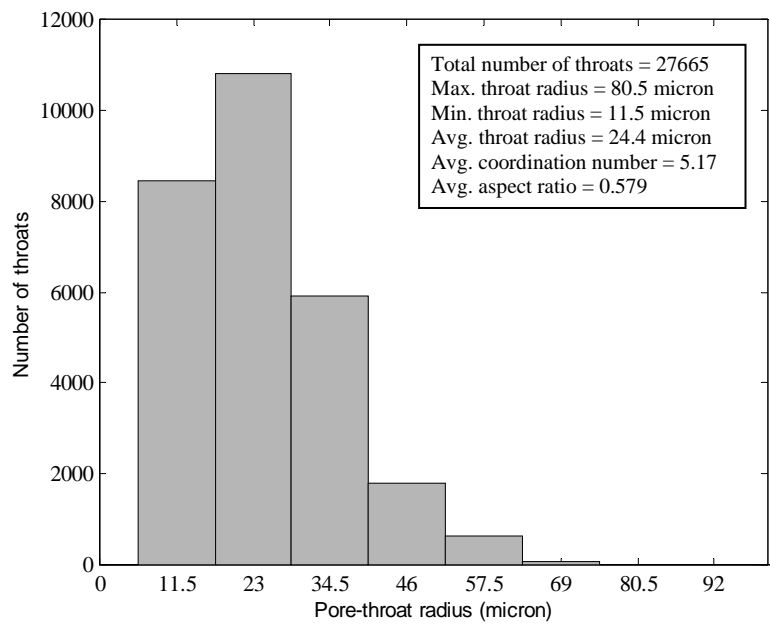


Figure 4.39: Pore-throat properties of M\_B

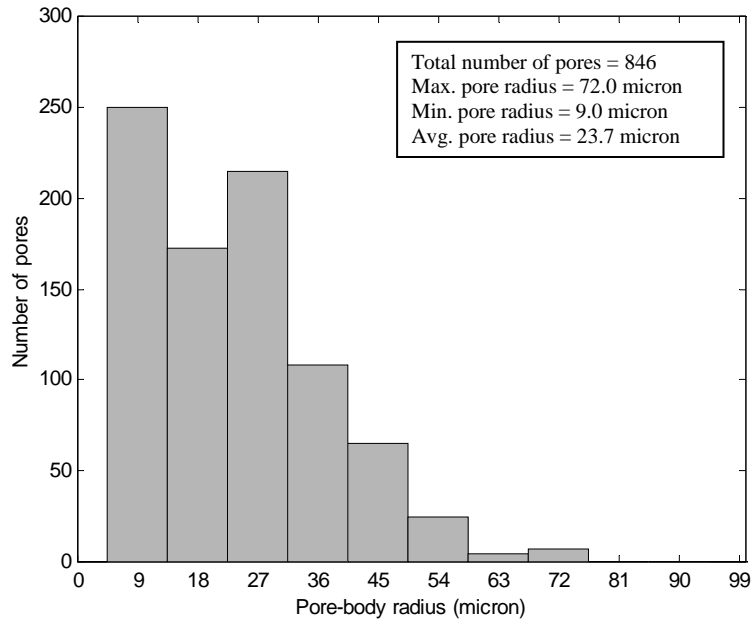


Figure 4.40: Pore-body properties of S\_B system

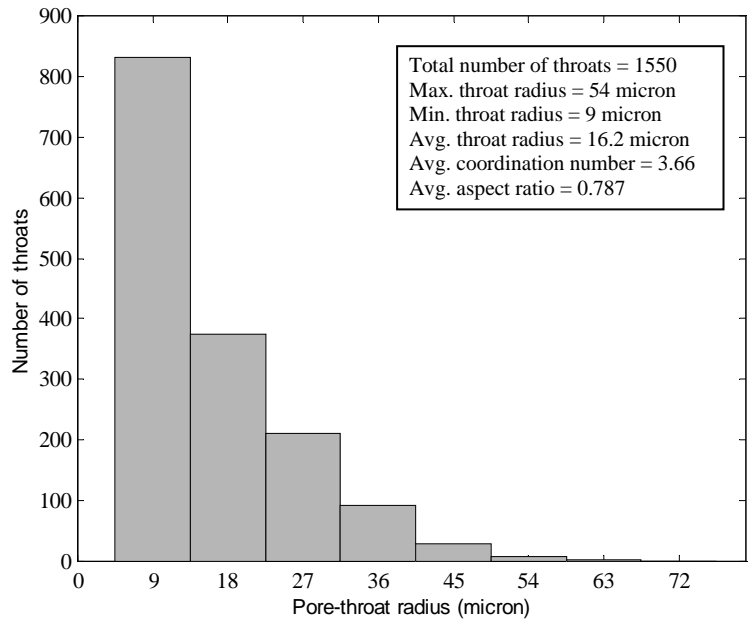


Figure 4.41: Pore-throat properties of S\_B system

#### **4.5 Impact of Image Resolution on Pore-Network Structure Properties**

To investigate the impact of image resolution on the pore-network structure properties, two porous media systems were analyzed at two different resolutions. The first system is the perfect glass beads shown as P\_B\_1 and P\_B\_2 in Table 3.1. The grain size diameter of these beads is 123 micron (+/- 6.2 micron) and the system was scanned at resolutions of 5.8 and 11.5 microns. The size of the analyzed subvolume is 300x300x450 pixels and 150x150x225 pixels for P\_B\_1 and P\_B\_2, respectively. These subvolume systems correspond to identically sized portions of the column.

The second system is the ooid sand sediment listed at O\_S\_1 and O\_S\_2 in Table 3.1. The resolutions of these images are 11.5 and 23.0 microns, while the sizes of the images are 375x400x475 pixels and 188\*200\*238 pixels for O\_S\_1 and O\_S\_2, respectively.

As can be shown in Figures 4.42 – 4.49, the resolution of the image has a significant impact on the calculated properties. For P\_B\_\* systems (P\_B\_1 and P\_B\_2) the number of pore-bodies changed from 13423 in the case of high resolution to 3519 in the case of low resolution. While the minimum pore-body and pore-throat sizes have values equal to the resolution of the image in each case (i.e., 5.8 and 11.5 micron for high and low resolution respectively), the maximum pore-body sizes showed a slight difference (i.e., the maximum pore-body radii are 52.2 and 46.0 microns for high and low resolution respectively), and the average pore-body values did not show a big difference (i.e., 18.9 and 14.2 microns for high and low resolution); the range of pore-body sizes that was resolved as discrete sizes differs dramatically in each resolution. This range is very important and controls many single and multiphase processes such as capillary

pressure- saturation relations and nonwetting phase entrapment in porous media systems. This example demonstrates the importance of resolution on obtaining physically-realistic pore-network elements. The same behavior can be noticed in the pore-throat data, the maximum pore-throat radii for the high and the low resolution images are 40.6 and 46.0 microns respectively. The coordination number and the aspect ratio are lower in the low resolution image. The coordination numbers are 4.94 and 9.4 and the aspect ratios are 0.616 and 1.0 for high and low resolution systems respectively. High aspect ratios (i.e., aspect ratio = 1.0) in the low resolution system occurs due to underestimating the sizes of pore bodies. It is the inability to resolve the discrete spectrum of pore-body and pore-throat sizes in the low resolution case that creates such a discrepancy in the coordination number and the aspect ratio between the two systems. As discussed in Chapter 2, the coordination number and the aspect ratio play an important role in single and multiphase processes, therefore, an accurate calculation of these values is required.

The resolution also has an impact on the ooid sand properties, although in different ways. The number of pore-bodies is reduced from 10,911 in the high resolution case to 4,977 in the low resolution case. The most significance difference between the two systems is in the maximum and average pore-body sizes and the average pore-throat size. The maximum and average pore-body sizes in the low resolution image are 161 and 68.7 microns compared to 126.5 and 45.8 microns for the high resolution image. While there is only a slight difference in the maximum pore-throat radius, the average pore-throat radius changes by over 50% (i.e., from 28.9 to 45.2 microns). The coordination numbers are 4.9 and 5.3 and the aspect ratios are 0.568 and 0.648 for high and low resolution systems respectively. The similarity in coordination numbers and aspect ratios

seems to indicate that the resolution has less of an impact on identifying the structure for the ooid systems.

A second point regarding the calculation of properties can be seen from this comparison. The grain size/resolution ratios for the P\_B\_\* systems are much less than in the O\_S\_\* systems. This affected the ability to resolve a wider range of sizes (i.e., discrete size classes) which, as a result, created discrepancy in the calculated aspect ratios and coordination numbers for the P\_B\_\* systems. On the other hand, less discrepancy is observed in the discrete pore-body and pore-throat sizes. Resolving discrete range of sizes, albeit different sizes, explains obtaining close estimates of coordination numbers and aspect ratios. The resolution affect the sizes of pore-body and pore-throats in the O\_S\_\*, given its grain diameter/resolution ratio, and created a big discrepancy.

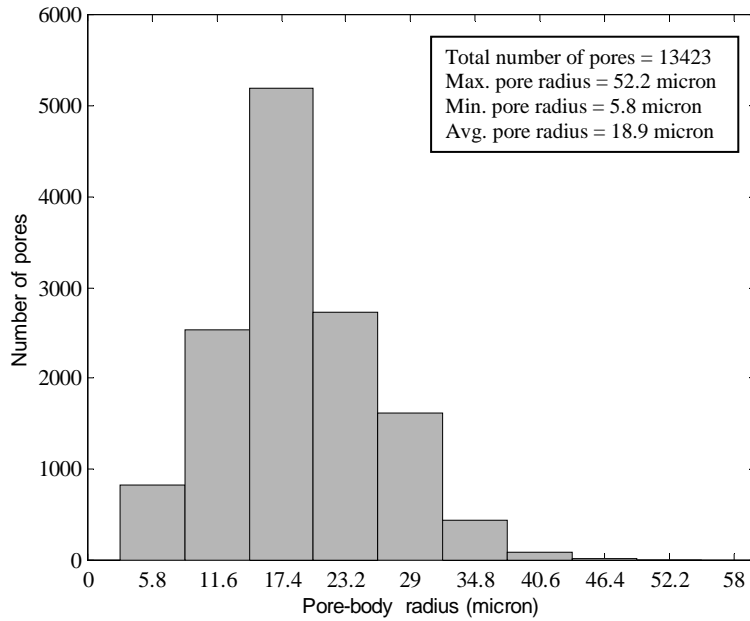


Figure 4.42: Pore-body properties of P\_B\_1 system

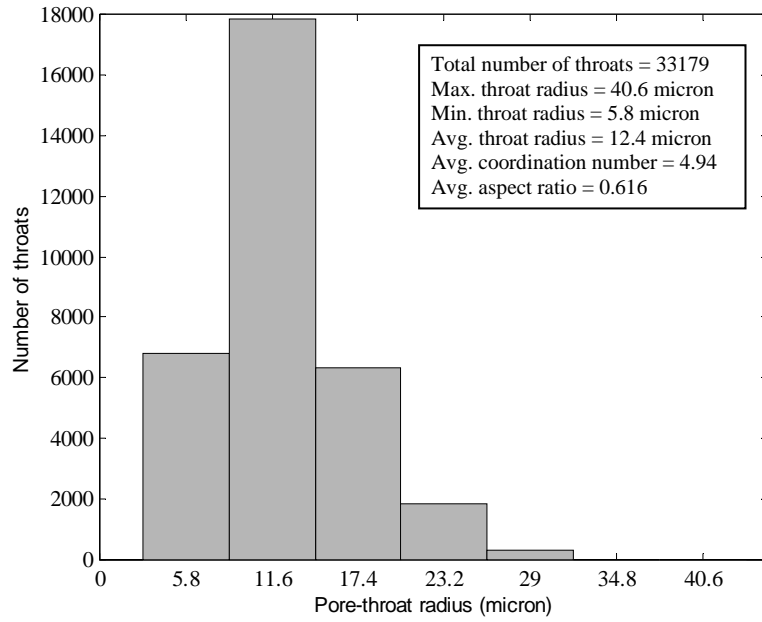


Figure 4.43: Pore-throat properties of P\_B\_1 system

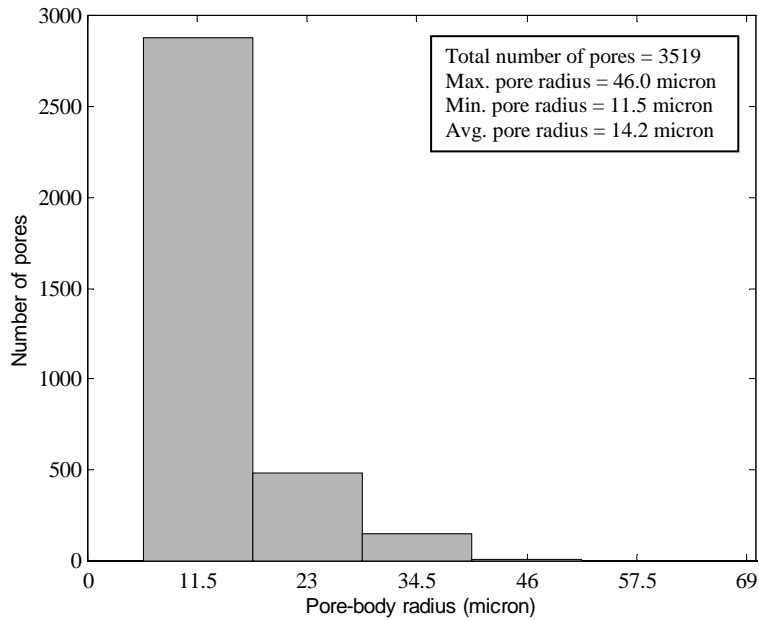


Figure 4.44: Pore-body properties of P\_B\_2 system

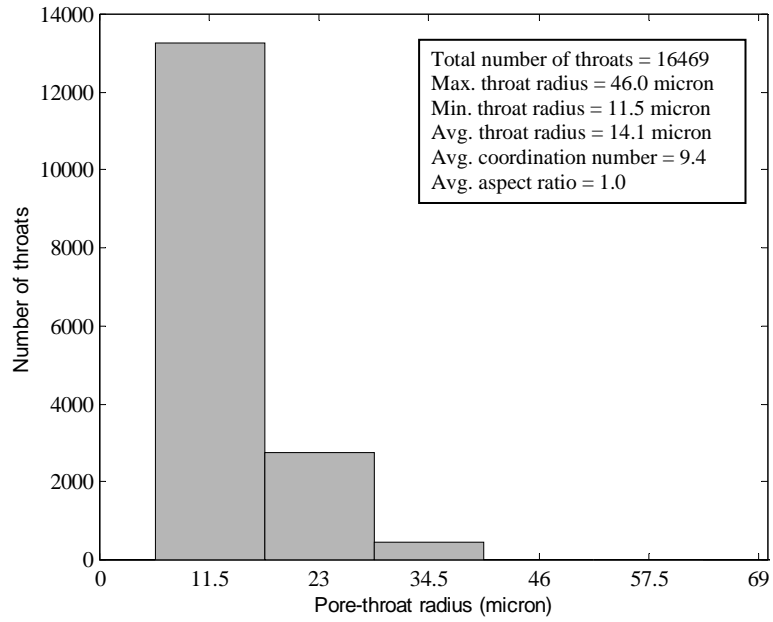


Figure 4.45: Pore-throat properties of P\_B\_2 system

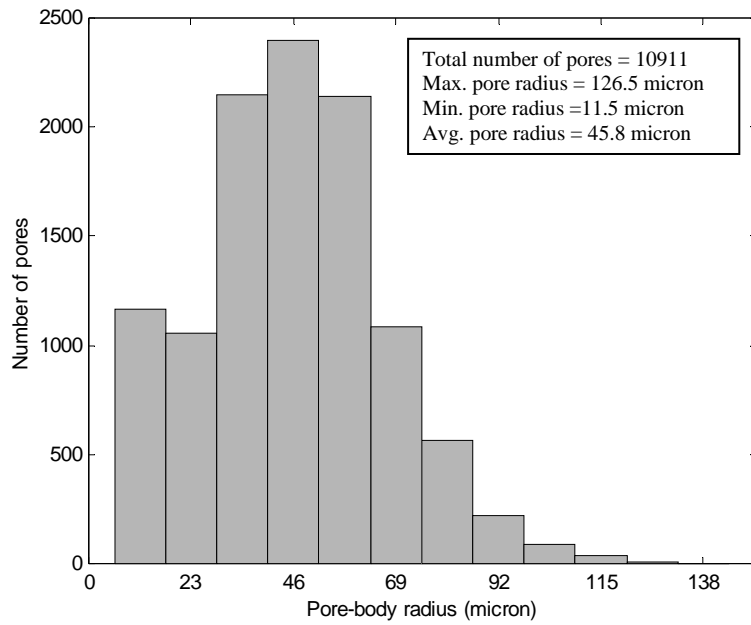


Figure 4.46: Pore-body properties of O\_S\_1 system

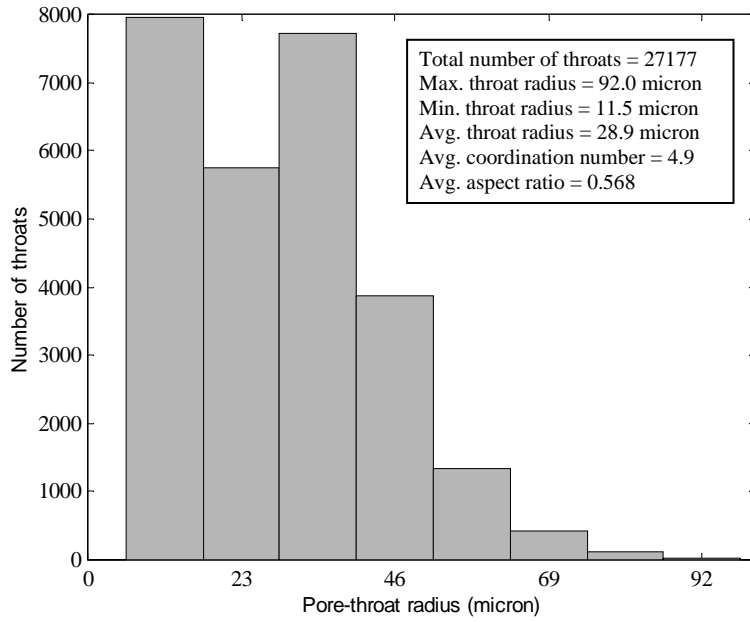


Figure 4.47: Pore-throat properties of O\_S\_1 system

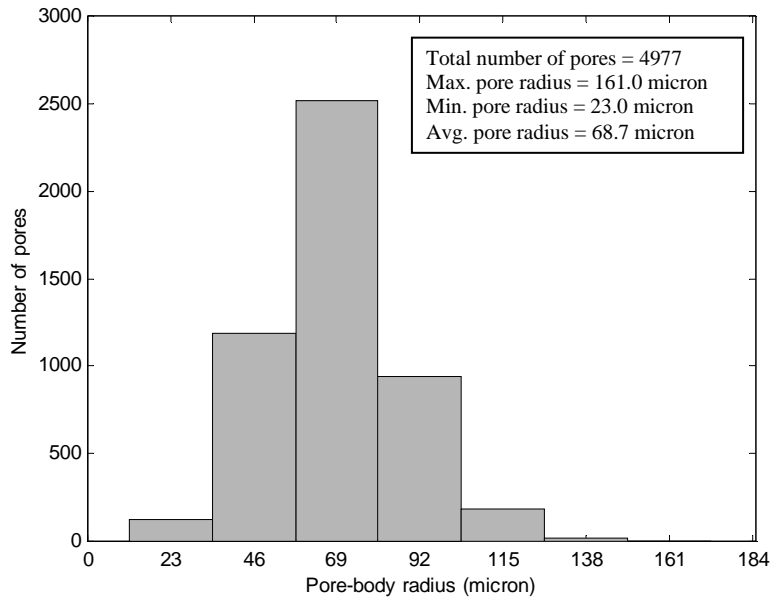


Figure 4.48: Pore-body properties of O\_S\_2 system

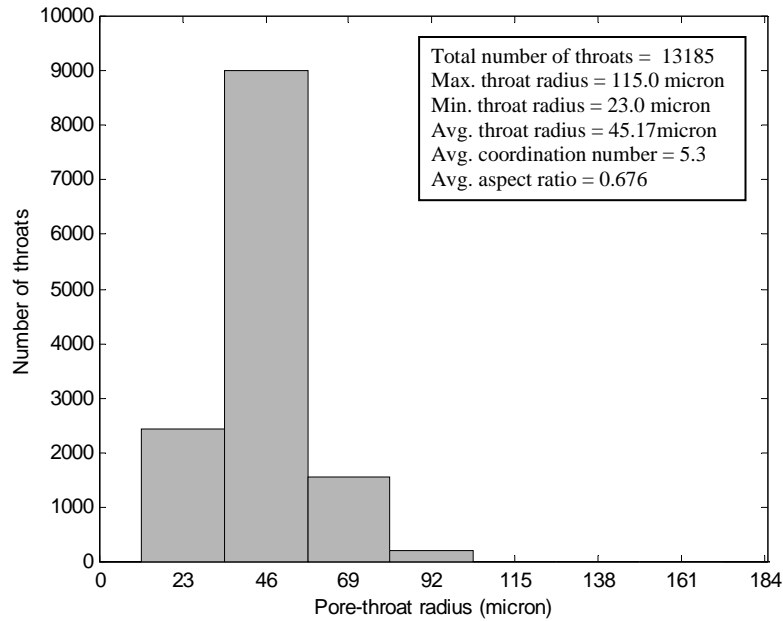


Figure 4.49: pore-throat properties of O\_S\_2 system

#### 4.6 Spatial Correlation of Pore-Network Structure

This section shows the correlation of pore-body sizes of each system based on semivariogram calculations discussed in section 3.10. Figures 4.50 - 4.57 show indicator semivariograms where the gray line depicts the variance of the system (pore-sizes are thresholded to either 0 or 1 based on the median value). The integral scale is used to provide a relative quantitative description of the correlation in the systems. Each semivariogram shows a typical behavior by its increase as the lag increases until it stabilizes at a certain level (i.e., the variance).

Figure 4.50 is the semivariogram of system X\_L\_B and shows that there is no correlation between pore-body sizes; this behavior is called pure nugget effect. This can be interpreted as the pore-bodies of same size are clustered together. This behavior could be attributed to the type of packing of this sphere size (i.e.,  $D = 1.0$  mm) in a column of a diameter of 5.0 mm. In addition, this system doesn't have REV for porosity within the

imaged volume. Figure 4.51 shows the indicator semivariogram of L\_B system ( $D = 0.4 - 0.6$  mm). The correlation between pore-body sizes extends to 9.1 jumps (2.1 mm), where each jump is defined as the median throat length. The semivariogram shows no nugget effect (i.e.,  $\gamma(h)$  at 0 starts at zero). This shows continuity and regularity of pore-body sizes. Also, the parabolic shape near the origin is associated with high regularity of pore sizes. Figure 4.52 shows the indicator semivariogram of M\_B system ( $D = 0.3 - 0.25$  mm). The extent of the correlation is 8.64 jumps (1.63 mm). This system shows a nugget effect at the origin of 0.0465. This implies that there is discontinuity and irregularity of pore-body sizes in the system. Figure 4.53 shows the indicator semivariogram of S\_B system ( $D = 0.25 - 0.177$  mm). While this system doesn't have an REV, it shows a correlation to 4.96 jumps (0.684 mm). The behavior of the semivariogram at the origin suggests a high degree of continuity and regularity of pore-body sizes. Figures 4.54 and 4.55 show the indicator semivariogram of P\_B\_1 and P\_B\_2 systems respectively. In the P\_B\_1 system, system of high resolution, the semivariogram has an integral length scale of 8.32 jumps (0.740 micron) and a nugget effect of 0.0624. The semivariogram of P\_B\_2, the same glass bead used in P\_B\_1 but imaged at low resolution, shows a length scale of 1.88 jumps (0.33 mm). The lack of correlation in P\_B\_2 system is mainly attributed to the narrow range of pore-body sizes. This is an example that shows the impact of resolution on the correlation between pore-bodies, where spatial correlation is different in the same sample imaged at different resolutions. The second system used to investigate the impact of resolution is ooid sand system (i.e., O\_S\_\*). Figure 4.56 shows the semivariogram of O\_S\_1 which shows that the nugget effect equals to 0.0445 and the integral scale length is 6.36 jumps (1.22 mm). Figure 4.57

shows the semivariogram of O\_S\_2 which shows no nugget effect and that the integral scale length is 8.85 jumps (2.8 mm).

Findings from this section indicate that pore-networks of porous media systems, even with almost similar properties (i.e., glass bead), have unique type and behavior of correlation among the pore-network element. Therefore, incorporating a general type of a correlation a priori in a pore-network may lead to inaccurate predictions or understanding of the problem being investigated.

These findings highlight the merits of this research by presenting a systematic methodology of extracting the physically-realistic pore-network structure of porous media systems based on the true morphology of these systems. This structure could be up-scaled to be incorporated into a pore-network model used to predict or understand macroscopic properties and phenomena from the microscopic level.

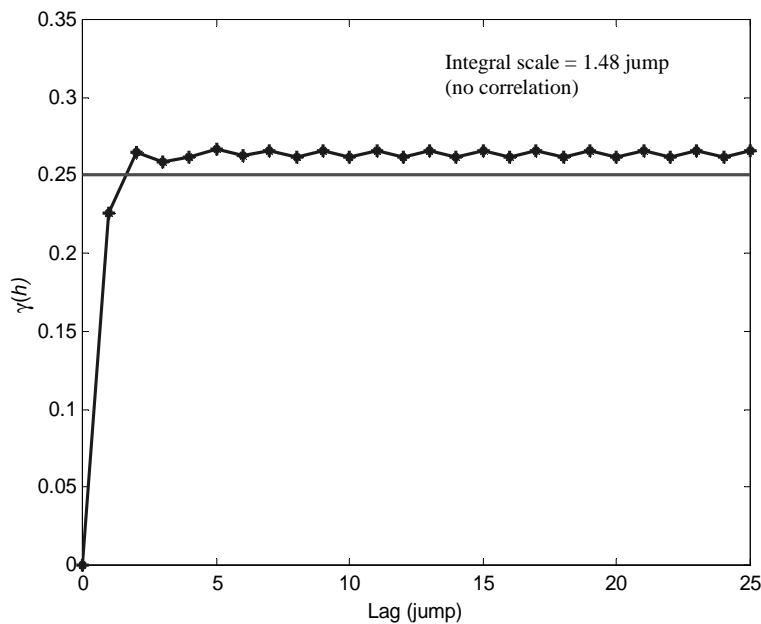


Figure 4.50: Indicator semivariogram of X\_L\_B system

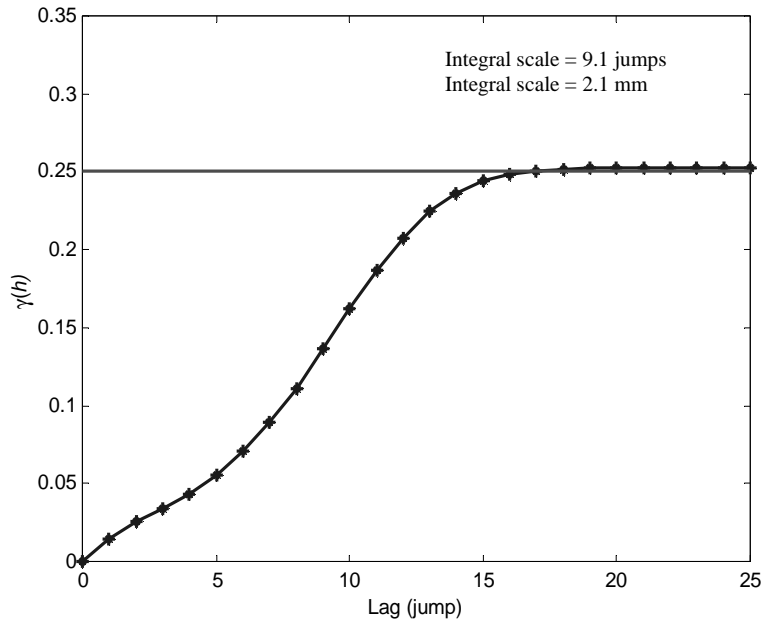


Figure 4.51: Indicator semivariogram of L\_B system

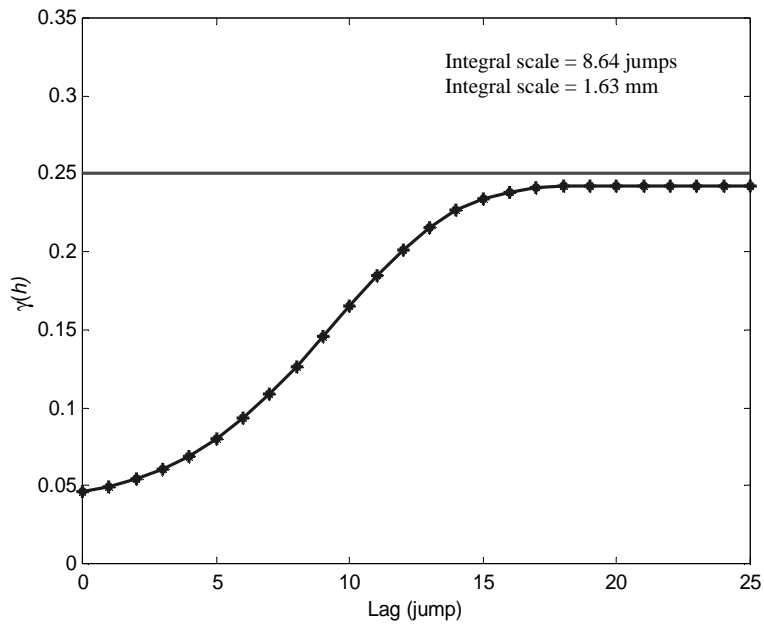


Figure 4.52: Indicator semivariogram of M\_B system

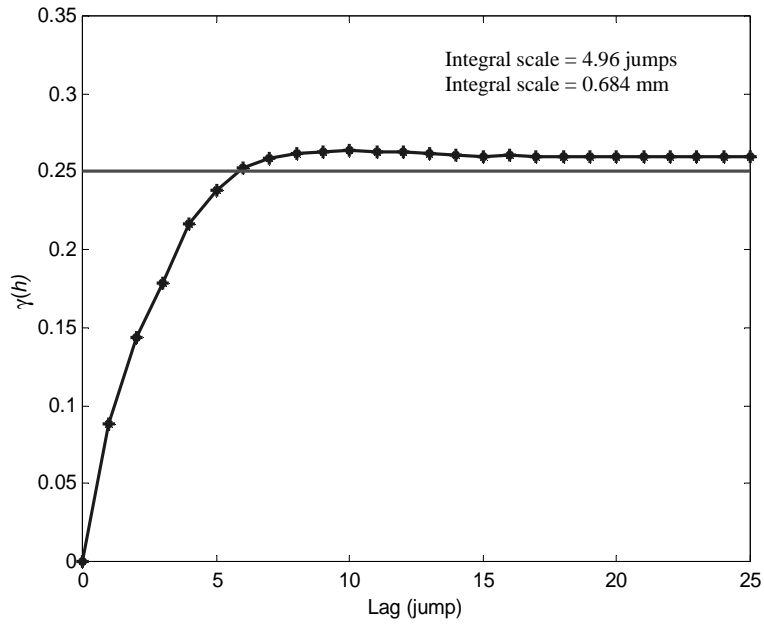


Figure 4.53: Indicator semivariogram of S\_B system

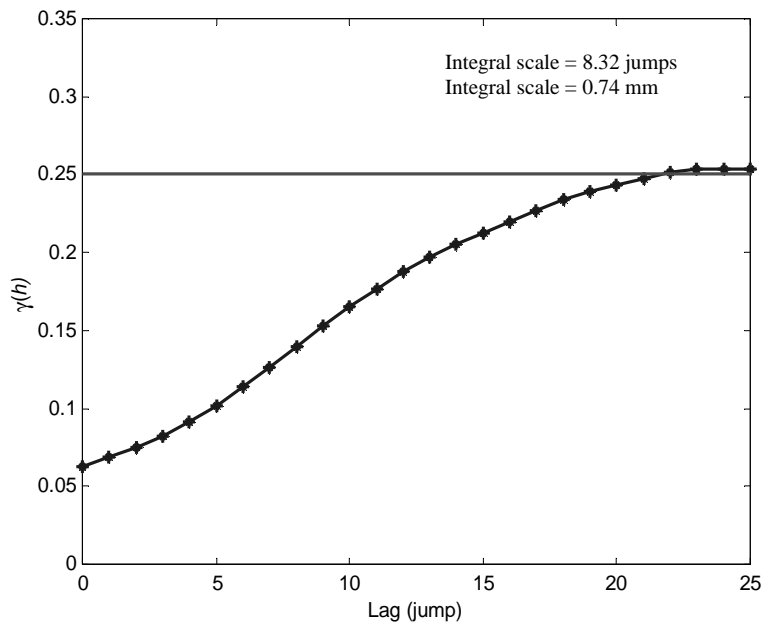


Figure 4.54: Indicator semivariogram of P\_B\_1 system

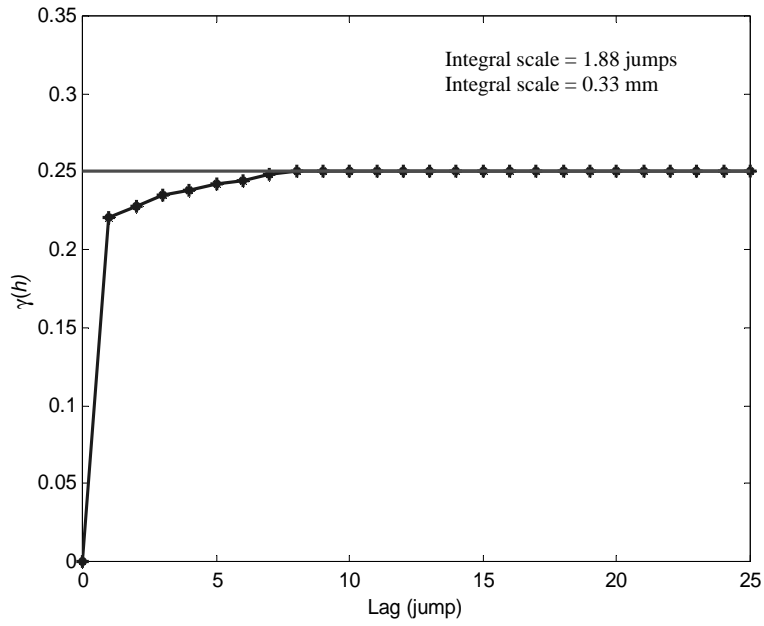


Figure 4.55: Indicator semivariogram of P\_B\_2 system

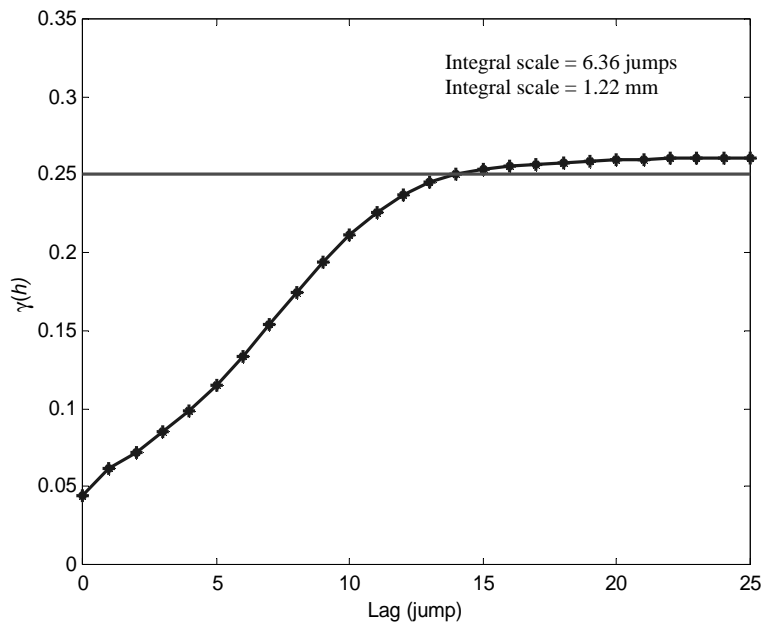


Figure 4.56: Indicator semivariogram of O\_S\_1 system

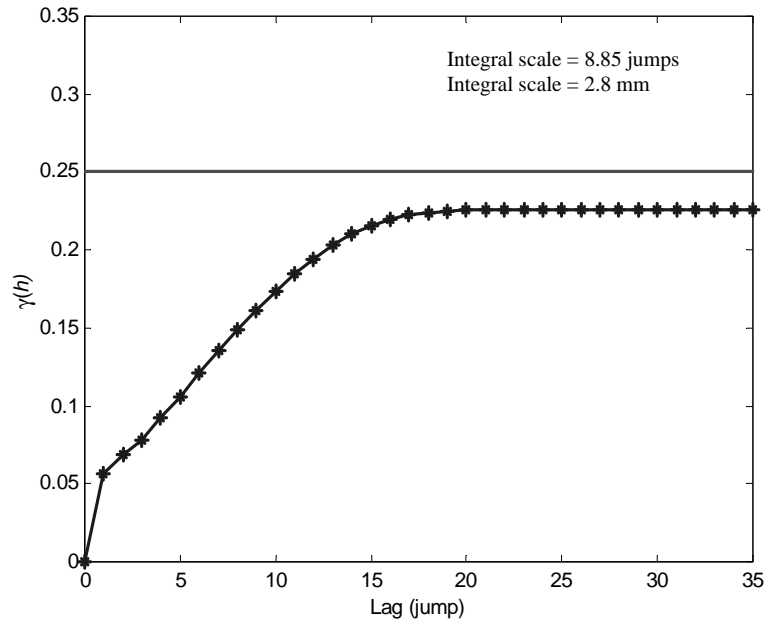


Figure 4.57: Indicator semivariogram of O\_S\_2 system

## 5. Conclusions and Recommendations

In this research, algorithms were implemented to obtain high resolution three-dimensional images using synchrotron microtomography. Image processing algorithms and techniques were used to enhance and visualize these images. Morphological algorithms were developed to extract pore-network structure from images of unconsolidated porous media systems. The algorithms are based on the three-dimensional skeletonization of the pore space in the form of nodes connected to paths. Dilation algorithms were developed to generate inscribed spheres on the nodes and paths of the medial axis to represent pore-bodies and pore-throats of the network, respectively. Theoretical packings were used to verify the algorithms. Pore-network structure is captured by three-dimensional spatial distribution (i.e., x, y, z coordinate) of pore-bodies and pore-throats, pore-body size distribution, pore-throat size distribution, and the connectivity. Systems of porous media and natural sand (oid sand) were used in this study to investigate the applicability of the algorithms. In addition to the pore network structure, geometrical properties (i.e., porosity and specific surface area) of these systems were calculated. REV analysis on the porosity was performed on the systems. The impact of resolution on the calculated properties was investigated using perfect glass bead and natural sand (oid sand) systems. Finally, semivariograms and integral scale concepts were used as a tool to investigate the spatial correlation of the network.

Results of this research showed that microtomography is an effective and efficient tool not only to nondestructively visualize the interior of the object, but can also provides the necessary resolution to quantitatively analyze many systems. The quality of the

datasets depends on photon energy, photon flux, size of the sample, type of the sample, and the number of projections. Optimization of these factors is necessary to obtain the resolution and contrast necessary to resolve the property(ies) of concern.

Analysis of the medial axes created from the regular packings showed that, even in these ideal cases, the reconstruction of the skeleton is sensitive to the resolution of the image. In addition, the non-uniqueness of the node to pore-body correlation can lead to an overestimate of the number of pores. To provide a more physical representation of the pore body locations, node merging algorithms were developed. Results also demonstrated that the pixelization effect (e.g., the finite size of the pixels) plays an important role for the construction of the medial axis and extraction of pore network parameters.

Verification of the algorithms on regular (i.e., cubic and rhombohedral) packings showed that the algorithms are able to obtain the correct pore network structure, including the number, size, and location of the pore bodies, the number, size, and location of the pore throats, and the connectivity. It was found that because the MA-based method is resolution-dependent and that precise voxel locations of nodes are non-unique, there are some slight differences from an analytically-based method (i.e., MDT). However, as the resolution of the image increases, the agreement between the two methods improves.

Implementation of the algorithms on real porous media systems (i.e., three-dimensional images obtained from synchrotron microtomography), demonstrated that the algorithms were able to partition the pore space into an equivalent network as interpreted from 3D visualization and/or examination 2D slices. Sources of uncertainty include: (1) pixelization at low resolution; (2) the arbitrary process of choosing the center of a pore body (i.e., node) from a group of voxels all having the same burn number; and (3) the

merging process of pore-bodies (i.e., if an overlap exists between two pore-bodies, the smaller pore-body is removed from the network).

The merging algorithm could be modified by replacing the overlapped pore-bodies by an equivalent pore-body located at the closest voxel on the medial axis to the center of gravity between the overlapped pore-bodies. In addition, the shapes of the pore-network elements are chosen to be circular cross-sections; however, pore-network elements can be given any other shape (e.g., triangular or square cross sections) to more accurately represent irregular pore spaces. Another modification can be performed on the dilation algorithm in which it proceeds in radial steps of unit-voxel length. This part of the medial-axis algorithm can be refined (at considerable computational expense) to provide more accurate values for the inscribed radii. Also, the effective radii of pore-network elements can be calculated to incorporate the total volume of the void space in the volume of the pore-network elements.

Results from the theoretical and real systems highlighted the difficulty in creating a unique network from a complex, continuum pore space. However, results showed that the algorithms developed are general in use and can be applied to any three-dimensional unconsolidated porous media system.

Semivariograms and integral scale concepts are easy and effective tools to describe and quantify the spatial correlation among pore-network structure elements. This correlation is important and controls many processes and phenomena in single and multiphase flow and transport problems such as the entrapment of nonaqueous phase liquid (NAPL) in porous media systems. In calculating the body-body spatial correlation, a fixed “jump” is used to calculate the semivariogram lag. In presenting the results, the

jump is set equal to the median length of pore-throat of the system. More accurate calculations of the “jump” can be performed by taking a physical distance instead of a jump and accounting for the pores that are located within this distance.

Results showed that the resolution does have a significant impact on the properties of the system being characterized. This impact varies in its significance based on the system (i.e., feature size) and the properties being calculated. Therefore, a thorough resolution sensitivity analysis should be carried out to determine the degree of error associated with a system imaged at a given resolution.

It should be emphasized here that glass bead systems analyzed in this research were not meant to be characterized, but were chosen to present and show a methodology of extracting physically realistic pore-network properties from porous media systems from high resolution three-dimensional images. In this regard, issues to be investigated are the reproducibility of results as a function of spatial distribution, REV of pore-network structure, and up-scaling the pore-network structure.

An important consideration that should be addressed is how the differences in network structure affect relevant flow and transport processes. The differences in pore sizes, pore size distributions, and their spatial correlations may have significant effects on multiphase simulations.

In conclusion, this research provides a methodology to extract physically-realistic pore network structures. This structure can be used to correlate pore-scale phenomena with the pore structure; for example, entrapment of non-wetting phase in the largest pore bodies or the relationship between non-wetting phase blob size and pore body correlation. The network structure can also be incorporated into a pore-network model to understand

or predict transport and flow processes and phenomena in complex porous media systems such as permeability, dispersivity, or pressure-saturation curve. In conjunction with microtomography, a corresponding physical experiment can be conducted to verify the developed pore-network model. This provides a unique opportunity to understand microscale processes and phenomena and develop better up-scaling techniques.

## References

- Adamson, A. W. 1982. Physical chemistry of the surfaces. 4th Ed. Wiley. New York.
- Al-Raoush, R., K. E. Thompson, and C. S. Willson. 2002. Comparison of Network Generation Techniques for Unconsolidated Porous Media Systems. submitted to Soil Science of America Journal.
- Annable, M. D., J. W. Jawitz, P. S. Rao, D. P. Dai, H. Kim, and A. L. Wood. 1998. Field evaluation of interfacial and partitioning tracers for characterization of effective NAPL-water content areas. *Ground Water*. 36(3): 495-502.
- Auzerais, F. M., J. Dunsmuir, B. B. Ferreol, N. Martys, J. Olson, T. S. Ramakrishnan, D. H. Rothman, L. M. and Schwartz. 1996. Transport in sandstone: a study based on three dimensional microtomography. *Geophysical Research Letters*. 23(7): 705-708.
- Avnir, D., D. Farin, and P. Pfeifer. 1984. Surface irregularity of particulate materials: A fractal approach. *Journal of Colloid and Interface Science*. 103:112-123.
- Baldwin, C. A., A. J. Sederman, M. D. Mantle, P. Alexander, and L. F. Gladden. 1996. Determination and characterization of the structure of a pore space from 3D volume images. *Journal of Colloid and Interface Science*, 181:79-92.
- Bear, J. 1972. Dynamics of fluids in porous media. American Elsevier. New York, NY.
- Bernabe, Y. 1991. Pore geometry and pressure dependence of the transport properties in sandstones. *Geophys*. 56:436-446.
- Berryman, J. G., 1985. Measurement of spatial correlation functions using image processing techniques. *Journal of Applied Physics*. 57 (7): 2374-2384.
- Berryman, J. G., and S. T. Blair. 1986. Use of digital image analysis to estimate fluid permeability of porous materials: Application of two-point correlation function. *Journal of Applied Physics*. 60(6): 1930-1938.
- Berryman, J. G., and S. T. Blair. 1987. Kozeny-Carman relations and image processing methods for estimating Darcy's constant. *Journal of Applied Physics*. 62(6): 2221-2228.
- Blunt, M. and P. King. 1990. Macroscopic parameters from simulations of pore scale flow. *Physical Review A*, 42 (8): 4780-4787.
- Blunt, M. and P. King. 1991. Relative permeability from two- and three-dimensional pore-scale modeling. *Transport in Porous Media*.6:407-433.

Bowen, D. K., J. S. Elliott, S. R. Stock, and S. D. Dover. 1986. X-ray microtomography with synchrotron radiation. *SPIE*. 691: 94-98.

Bradford, S. F., and F. J. Leij. 1995. Wettability effects on scaling two and three-fluid capillary pressure-saturation relations. *Environmental Science and Technology*. 29:1446-1455.

Bradford, S. F., and F. J. Leij. 1997. Estimating interfacial areas for multi-fluid soil systems. *Journal of Contaminant Hydrology*. 27:83-105.

Brandt, J. W. 1992. Describing a solid with three-dimensional skeleton. *SPIE. Curves and Surfaces in Computer Vision and Graphics III*. 1830:258-269.

Bryant, S. P., R. King, and D. W. Mellor. 1993. Network model evaluation of permeability and spatial correlation in a real random sphere packing. *Transport in Porous Media*. 11. 53-70.

Cary, J. W. 1994. Estimating the surface area of fluid phase interfaces in porous media. *Journal of Contaminant Hydrology*. 15: 243-248.

Cassel, D. K., Brown, J. M., and Johnson, G. A. 1990. Computer tomographic analysis of water distribution and flow in porous media. *Theoretical and Applied Climatology*, 42: 223-228.

Celia, M. A., P. C. Reeves, L. A. Ferrand. 1995. Recent advances in pore scale models for multiphase flow in porous media. *Reviews of Geophysics*. 33(2): PP 1049.

Chatzis I., and F. A. L. Dullien. 1977. Modeling pore structure by 2-D and 3-D networks with application to sandstones. *Journal of Canadian Petroleum Technology*. 16: 07-106.

Chiles, J-P., and P. Delfiner. 1999. *Geostatistics: Modeling spatial uncertainty*. John Wiley & Son, Inc.

Clausnitzer, V., and J. W. Hopmans. 1999. Determination of phase-volume fractions from tomographic measurements in two-phase systems. *Advances in Water Resources*. 22(6):577-584.

Coker, D. A., and S. Torquato. 1996. Morphology and physical properties of Fontainebleau sandstone via a tomographic analysis. *Journal of Geophysical Research*. 101(B8): 17497-17506.

Coker, D. A., and S. Torquato. 1995. Extraction of morphological quantities from a digitized medium. *Journal of Applied Physics*. 77 (12): 6087-6099.

Coles, M. E., R. D. Hazlett, P. Spanne, W. E. Soll, E. L. Muegge, and K. W. Jones. 1998. Pore level imaging of fluid transport using synchrotron X-ray microtomography. *Journal of Petroleum Science and Engineering*. 19:55-63.

Cousin I., P. Levtiz, and A. Bruand. 1996. Three-dimensional analysis of loamy-clay soil using pore and solid chord distributions. *Eur J Soil Sci*. 47: 439-452.

Crestana, S., S. Mascarenhas, and R. S. Pozzi-Mucelli. 1985. Static and dynamic three-dimensional studies of water in soil using computed tomographic scanning. *Soil Science*, 140 (1): 326-332.

Crestana, S., R. Cesareo, and S. Mascarenhas. 1986. Using a computed tomography miniscanner in soil science. *Soil Science*. 142 (1): 56-61.

Dias, M. M., and A. C. Payatakes. 1986. Network models for two-phase flow in porous media, 2, motion of oil ganglia. *J. Fluid Mechanics*. 164: 337-368.

Dias, C. E., I. Chatzis, and F. A. L. Dullien. 1987. Simulation of capillary pressure curves using bond correlated site percolation on a simple cubic network. *Transport in Porous media*. 2:215-240.

DiCarlo, D. A., T. W. J. Bauters, T. S. Steenhuis, J. Y. Parlange, and B. R. Bierck. 1997. High-speed measurement of three-phase flow using synchrotron X ray. *Water Resources Research*. 33 (4):569-576.

Dillard, L. A., and M. Blunt. 2000. Development of a pore network simulation model to study nonaqueous phase liquid dissolution. *Water Resources Research*. 36 (2): 439-454.

Dixit, A. B., S. R. McDougall, and K. S. Sorbie. 1998. A pore-level investigation of relative-permeability hysteresis in water-wet systems. *SPE Journal*. 3:115-123.

Dixit, A. B., S. R. McDougall, K. S. Sorbie, and J. S. Buckley. 1999. Pore-scale modeling of wettability effects and their influence on oil recovery. *SPE Reservoir Evaluation and Engineering*. 2:25-36.

Doughty, D. A., and L. Tomutsa. 1997. Imaging pore structure and connectivity in high resolution NMR microscopy. *Int. J. Rock. Mech. & Min. Sci.*, 34:3-4.

Doyen, P. M. 1988. Permeability, conductivity, and pore geometry of sandstone. *Journal of Geophysical Research*. 93:7729-7740.

Dullien, F.A.L. 1992. *Porous media: fluid transport and pore structure*. Academic Press, Inc., New York. NY

D'Hollander, E. H. 1979. Estimation of the pore size distribution from the moisture characteristic. *Water Resources Research*. 15:107-112.

Ebashi, S., M. Koch, and E. Rubinstein. 1991. Handbook on synchrotron radiation. North-Holland. Amsterdam.

Fenwick, D. H., and M. J. Blunt. 1998. Three-dimensional modeling of three-phase imbibition and drainage. *Advances in Water Resources*. 21 (2):121-143.

Ferrand, L. A., and M. A. Celia. 1992. The effect of heterogeneity on the drainage capillary pressure-saturation relation. *Water Resources Research*. 28 (3): 859-870.

Fisher, R., E. Wolfart, S. Perkins, A. Walker. 1997. Hypermedia image processing reference (Hipr). Wiley, John & Sons. Inc.

Fischer, U. and M. Celia. 1999. Prediction of relative and absolute permeabilities for gas and water retention curves using a pore-scale network model. *Water Resources Research*. 35 (4): 1089-1100.

Fredrich, J. T. 1999. 3D imaging of porous media using laser scanning confocal microscopy with application to microscale transport processes. *Phys. Chem. Earth (A)*, 24(7): 551-561.

Goldak, J. A., X. Yu, A. Knight, L. Doug. 1991. Constructing discrete medial axis of 3-D object. *International journal of computational geometry and application*. 1(3): 327-339.

Gonzalez, R. C. and P. Wintz. 1987. Digital image processing. Addison-Wesley publishing company.

Gvartzman, H., and P. V. Roberts. 1994. Pore scale spatial analysis of two immiscible fluids in porous media. *Water Resources Research*. 27(6): 1165-1176.

Ham K., J. Hua , R. Al-Raoush, X. Xie, L. S. Simeral, C. S. Willson, G. R. Byerly, L. S. Simeral, M. L. Rivers, R. L. Kurtz, and L. G. Butler. Three-dimensional imaging of polymer additive blends with synchrotron tomography at multiple x-ray energies: turning pretty movies into useful data”, to be submitted.

Harold, J., Vinegar, and S. L. Wellington. 1987. Tomographic imaging of three-phase flow experiments. *Review of Science Instruments*. 58 (1): 96-107.

Hassanizadeh, S. M., and W. G. Gray. 1990. Mechanics and thermodynamics of multiphase flow in porous media including interphase boundaries. *Advances in Water Resources*. 13 :169-186.

Hassanizadeh, S. M., and W. G. Gray. 1993a. Thermodynamic basis of capillary pressure in porous media .*Water Resources Research*. 29(10):3389-3405.

Hassanizadeh, S. M., and W. G. Gray. 1993b. Toward an improved description of the physics of two-phase Flow. *Advances in Water Resources*.16:53-67.

Hazlett, R. D. 1995. Simulation of capillary-dominated displacements in microtomographic images of reservoir rocks. *Transport in porous media*, 20: 21-35.

Herman, G. T. 1980. *Image reconstruction from Projections*. Academic press.

Hidajat, I., A. Rastogi, M. Singh and K. K. Mohanty. 2001. Transport properties of porous media from thin-sections. SPE 69623, SPE LACPEC, March 25-27.

Hilpert, M., and C. T. Miller. 2001. Pore-morphology-based simulation of drainage in totally wetting porous media, *Advances in Water Resources*. 24: 243-255.

Hsieh, H. T., G. O Brown, and M. L. Stone. 1998. Measurement of porous media component content and heterogeneity using Gamma ray tomography. *Water Resources Research*. 34(3): 365-372.

Hsieh, H.T., G. O. Brown, and M. L. Stone. 1998. Quantification of porous media using computerized tomography and a statistical segregation threshold. *American Society of Agricultural Engineers*. 41(6): 1697-1706.

Hubbell, J. H. 1969. Photon cross sections, attenuation coefficients, and energy absorption coefficients from 10 keV to 100 GeV, *Natl. Stand. Ref. Data Ser. 29*, Natl. Inst. of Stand. and Technol., Gaithersburg, MD.

Hunt, P. K., P. Engler, and C. Bajsarowicz. 1988. Computed tomography as a core analysis tool: applications, instrument evaluation, and image improvement techniques. *Journal of Petroleum Technology*. 1203-1210.

Imhoff, P. T., P. R. Jaffe, G. F. Pinder. 1994. An experimental study of complete dissolution of nonaqueous phase liquid in saturated porous media. *Water Resources Research*. 30 (2): 307-320.

Imhoff, P. T., M H. Arthur, and C. T. Miller. 1998. Complete dissolution of trichloroethylene in saturated porous media. *Environmental Science and Technology*. 32: 2417-2424.

Ioannidis, M. A., I. Chatzis, and A. C. Payatakes. 1991. A mercury porosimeter for investigation capillary phenomena and microdisplacement mechanisms in capillary networks. *Journal of Colloid and Interface Science*. 143(1):22-36.

Ioannidis, M.A., I. Chatzis, and E.A. Sudicky. 1993. The effect of spatial correlation on the accessibility characteristics of three-dimensional cubic networks as related to drainage displacements in porous media. *Water Resources Research*. 29(6): 1777-1785.

- Ioannidis, M. A., I. Chatzis. 2000. On the geometry and topology of 3D stochastic porous media. *Journal of Colloid and Interface Science*. 229:323-334.
- Jensen, J. L., L. W. Lake, P. W. M. Corbett, and D. J. Goggin. 2000. *Geostatistics for petroleum engineers and geoscientists*. 2<sup>nd</sup> edition. Elsevier.
- Jerauld, G. R., and S. J. Salter. 1990. The effect of pore-structure on hysteresis in relative permeability and capillary pressure: pore level modeling. *Transport in Porous Media*. 5:103-151.
- Kak, A., C. and M. Slaney. 1988. *Principles of computerized tomographic imaging*. IEEE press. New York, NY.
- Karkare, M. V., and F. Tomlinson. 1996. Determination of the air-water interfacial area in wet “unsaturated” porous media. *Journal of Colloid and Interface Science*. 12:2041-2044.
- Khalili, A., A. J. Basu, and U. Pietrzyk. 1998. Flow visualization in porous media via positron emission tomography. *Physics of Fluids*. 10(4): 1031-1033.
- Kinney, J. H. and M. C. Nichols. X-ray tomographic microscopy (XTM) using synchrotron radiation. *Annual Review of Materials Science*. 22:121-52.
- Klobes, P., H. Riesemeier, K. Meyer, and J. Geobbels. 1997. Rock porosity determination by combination of X-ray computerized tomography with mercury porosimetry. *Fresenius Journal of Analytical Chemistry*. 357:543-547.
- Knapp, G. S., M. A. Beno, and H. You. 1996. Hard x-ray synchrotron radiation applications in material science. *Annual Review of Materials Science*. 26:693-725.
- Kwiecien, M. J., I. F. Macdonald, and F. A. L. Dullien. 1990. Three-dimensional reconstruction of porous media from serial section data. *Journal of Microscopy*. 159 (3) 343-359.
- Kwok, P. C. 1988. A thinning algorithm by contour generation. *Commun ACM*. 31:1314-1324.
- Lenhard, R. J. 1992. Measurement and modeling of three-phase saturation-pressure hysteresis. *Journal of Contaminant Hydrology*. 9:243-269.
- Lenormand, R., C. Zarcone, and A. Sarr. 1983. Mechanism of the displacement of one fluid by another in a network of capillary ducts. *Journal of Fluid Mechanics*. 135:337-353.
- Li, D. C., and L. W. Lake. 1994. A moving window semi-variance estimator. *Water Resources Research*. 30:1479-1489.

- Li, Y., and N. C. Wardlaw. 1986a. The influence of wettability and critical pore-throat size ratio on snap-off. *Journal of Colloid and Interface Science*. 109:473-486.
- Li, Y., and N. C. Wardlaw. 1986b. Mechanisms of nonwetting phase trapping during imbibition at slow rates. *Journal of Colloid and Interface Science*. 109:461-472.
- Liang, Z. R., P. C. Phillippi, C. P. Fernandes, and F. S. Magnani. 1999. Prediction of permeability from the skeleton of three-dimensional pore structure. *SPE Reservoir Evaluation and Engineering*. 2 (2):161-168.
- Lindquist, W. B., and A. Venkatarangan. 1999. Investigating 3D geometry of porous media from high resolution images. *Phys. Chem. Earth. (A)*. 25(7): 593-599.
- Lindquist, W. B., S. Lee. 1996. Medial axis analysis of void structure in three-dimensional tomographic images of porous media. *Journal of Geophysical Research*. 101(B4): 8297-8310.
- Lohman, Gabrielle. 1998. *Volumetric image analysis*. John Wiley & Sons. New York, NY.
- Lowry, M. I. and C. T. Miller. 1995. Pore-scale modeling of nonwetting-phase residual in porous media. *Water Resources Research*. 31(3): 455-473.
- Lymberopoulos, D. P. and A. C. Payatakes. 1992. Derivation of topological, geometrical, and correlational properties of porous media from pore-chart analysis of serial section data. *Journal of colloid and interface science*. 150 (1):61-79.
- Mani, V. and K. K. Mohanty. 1999. Effect of pore-space spatial correlations on two-phase flow in porous media. *Journal of Petroleum Science and Engineering*. 23:173-188.
- Mardia, K. V. and T. J. Hainsworth. 1988. A spatial thresholding method for image segmentation. *IEEE transactions on pattern analysis and machine intelligence*. 10:919-927.
- Mayer, A. S. and C. T. Miller. The influence of porous medium characterization and measurement scale on pore-scale distributions of residual nonaqueous- phase liquids. *Journal of Contaminant Hydrology*. 11:189-213.
- McBride, J. F. and C. T. Miller. 1997. Entrapment of non-aqueous -phase liquids in a two-liquid porous media system: the residual-funicular NAPL-content relation. *EOS transactions*, 78, presented at the American Geophysical Union, fall meeting, San Francisco, CA. December 8-12.
- Mercer, J. W. and R. M. Cohen. 1990. A review of immiscible fluids in the subsurface: properties, models, characterization and remediation. *Journal of Contaminant Hydrology*. 6:107-163.

Miller, C. T., M. M. Poirier-McNeill, A. S. Mayer. 1990. Dissolution of trapped nonaqueous phase liquids: mass transfer characteristics. *Water Resources Research*. 26(11):2783-2796.

Miller, C. T., G. Christakos, P. T. Imhoff, J. F. McBride, J. A. Pedit, and J. A. Trangenstein, J.A .1998. Multiphase flow and transport modeling in heterogeneous porous media: challenges and approaches. *Advances in Water Resources*. 21 (2): 77-120.

Mishra, B. K., and M. M. Sharma. 1988. Measurement of pore-size distributions from capillary pressure curves. *American Institute of Chemical Engineers Journal*. 34(4):684-687

Mohanty, K. K., H. T. Davis, and L. E. Scriven. 1987. Physics of oil entrapment in water wet rock. *SPE Reservoir Engineering*. February, 113-128.

Montemagno, C. D., and W. G. Gray. 1995. Photoluminescent volumetric imaging: a technique for the exploration of multiphase flow and transport in porous media. *Geophysical Research Letters*. 22(4): 425-428.

National Institute of Standards and Technology. 1995. From factor, attenuation and scattering tables, NIST Stand. Ref. Database, 66, Gaithersburg, MD.

Nowicki, S. C., H. T. Davis, and L. E. Scriven. 1992. Microscopic determination of transport parameters in draying porous media. *Drying Technology*. 10 (4): 925-946.

Oh, W. and W. B. Lindquist. 1999. Image thresholding by indicator Kriging. *IEEE Transactions on Pattern Analysis and Machine Intelligence*. 21:590-601.

Parker, J. A., Kenyon, R. V., and Troxel, D. E, 1983. Comparison of Interpolation Methods for Image Resampling. *IEEE Transactions on Medical Imaging*, 2(1): 31-39.

Pauli, J., G. Scheying, C. Nugge, A. Zschunke, and P. Lorenz. 1997. Determination of the pore widths of highly porous materials with NMR microscopy. *Fresenius Journal of Analytical Chemistry*, 357:508-513.

Peters, E. J. and Hardham, W.D., 1990. Visualization of Fluid Displacements in Porous Media using Computed Tomography Imaging. *Journal of Petroleum Science and Engineering*, 4: 155-168.

Peters, E. J., Gharbi, R., and Afzal, N., 1996. A look at Dispersion in Porous Media through Computed Tomography Imaging. *Journal of Petroleum Science and Engineering*.15: 23-31.

Petrovic, A. M., J. E. Siebert, and P. E. Rieke. 1982. Soil bulk density in three dimensions by computed tomographic scanning. *Soil Science Society of America Journal*. 46(3): 445-450.

Peurrung, L., Rashidi, M., and Kulp, T., 1995. Measurements of porous medium velocity fields and their volumetric averaging characteristics using particle tracking velocitmetry. *Chem. Eng. Sci.*..50,2243.

Powers, S. E., Loureiro, C. O., L. M. Abriola, W. J. Jr. Weber. 1991. Theoretical study of the significance of nonequilibrium dissolution on nonaqueous phase liquids in subsurface systems. *Water Resources Research*. 27(4):463-477.

Powers, S. E., L. M. Abriola, W. J. Jr. Weber. 1992. An experimental investigation of NAPL dissolution in saturated subsurface systems: steady state mass transfer rates. *Water Resources Research*. 28(10):2691-2706.

Powers, S. E., L. M. Abriola, W. J. Jr. Weber. 1994. An experimental investigation of nonaqueous phase liquid dissolution in saturated subsurface systems: transient transfer rates. *Water Resources Research*. 30(2): 321-332.

Rajaram, H., L. A. Ferrand, and M. A. Celia, 1997. Prediction of relative permeabilities for unconsolidated soils using pore-scale network models. *Water Resources Research*. 33 (1): 43-52.

Rashidi, M., A. Tompson, T. Kulp, and L. Peurrung. 1996. 3-D microscopic measurement and analysis of chemical flow and transport in porous media. *Trans. ASME. J. Fluid Eng.* 118: PP 470.

Reed, A. H., R. Al-Raoush, C. S. Willson, and J. E. Cable. 2002. Comparative differences of pore geometry from planar and volumetric computer tomography images of marine sands. presented at the American Geophysical Union Spring Meeting, Washington, DC, May 28-31, 2002.

Reeves, P. C. and M. A. Celia. 1996. A functional Relationship between capillary pressure, saturation, and interfacial areas as revealed by a pore-scale network model. *Water Resources Research*. 32(8): 2345-2358.

Rintoul, M. D., S. Torquato, C. Yeong, D. T. Kaene, S. Erramilli, Y. N. Jun, D. M. Dabbs, and I. A. Aksay. 1996. Structure and transport properties of a porous magnetic gel via X-ray microtomography. *Phys Rev E*. 54:2663-2669.

Rivers, M. L., S. R. Sutton, and P. Eng. 1999. Geoscience applications of x-ray computed microtomography. *Proc. of the SPIE Conference on Developments in X-ray Tomography II*, Denver, CO. 3772:78-86

Rivers, M. L. 2002, <http://cars.uchicago.edu/software/tomography.html>

Roof, J. G. 1970. Snap-off of oil droplets in water wet porous media. *Society of Petroleum Engineering Journal*, March, 85-90.

- Russ, J. C. 1999. The image processing handbook. CRC press.
- Saripalli, K. P., P. S. Rao, and M. D. Annable. 1997. Estimation of non-aqueous phase liquid-water interfacial areas in porous media following mobilization by chemical flooding. *Environmental Science and Technology*. 31:3384-3388.
- Saripalli, K.P., P. S. Rao, and M. D. Annable. 1998. Determination of specific NAPL-water interfacial areas of residual NAPLs in porous media using the interfacial technique. *Journal of Contaminant Hydrology*. 30:375-391.
- Schroth, M. H., S. J. Aheam, J. S. Selker, and J. D. Istok. 1996. Characterization of miller-similar silica sands for laboratory hydrologic studies. *Soil Science Society of America Journal*. 60:1331-1339.
- Soll, W. E., M. A. Celia, and J. L. Willson. 1993. Micromodel studies of three-fluid porous media systems: pore-scale processes relating to capillary pressure-saturation relationships. *Water Resources Research*. 29(9): 2963-2974.
- Solyman, M., and I. L. Fabricius. 1999. Image analysis and Estimation of porosity and permeability of Arnager Greensand, Upper Cretaceous, Denmark. *Phys. Chem. Earth. (A)*, 24(7): 587-591.
- Spanne, P., J. F. Thovert, C. J. Jacquin, B. W. Lindquist, K. W. Jones, and P. M. Adler. 1994. Synchrotron computed microtomography of porous media: topology and transports. *Physical Review Letters*. 73(14): 2001-2004.
- Silverstein, D. L., and E. Tomlinson. 1997. Studies in air-water interfacial area for wet unsaturated particulate porous media systems. *Langmuir*. 13:4758-4761.
- Sirjani, A., and G. R. Cross. 1991. On representation of a shape's skeleton. *Pattern Recognition Letters*. 12:149-154.
- Thompson, K.E., and H.S. Fogler. 1997. Modeling flow in disordered packed beds from pore-scale fluid mechanics. *AIChE J*. 43:1377-1389.
- Torquato, S., and G. Stell. 1982. Microstructure of two-phase random media. I. The n-point probability functions. *Journal of Chemical Physics*. 77(4): 2071-2077.
- Tsakiroglou, C.D. and A.C. Payatakes. 1991. Effects of pore-size correlations on mercury porosimetry curves. *Journal of Colloid and Interface Science*. 146(2): 479-494,
- Van Brakel, J., S. Modry, and M. Svata. 1981. Mercury porosimetry: State of the art. *Powder Technology*. 29:1-12.
- Vogel, H. J., and K. Roth. 1997. A new approach for determining effective soil hydraulic functions. *European Journal of soil sciences*. 49(4): 547-556.

Vogel H. J., 2000. A numerical experiment on pore size, pore connectivity, water retention, permeability and solute transport using network models. *European Journal of Soil Science*, 51: 99-105.

Vogel, H. J., and K. Roth. 2001. Quantitative morphology and network representation of soil pore structure. *Advances in Water Resources*. 24:233-242.

Wan, J., and J. L. Wilson. 1994. Colloid transport in unsaturated porous media. *Water Resources Research*. 30(4): 857-864.

Warner, G.S., J. L. Nieber, I. D. Moore, and R. A. Geise. 1989. Characterizing macropores in soil by computed tomography. *Soil Science Society of America Journal*. 53(3): 653-660.

Webster, R., and M. Oliver. 2001. *Geostatistics for environmental scientists*. John Wiley & sons, ltd.

Wong, P. 1999. *Methods in the physics of porous media*. 35. Academic press.

Yale, D. P. 1985. Recent advances in rock physics. *Geophys*.50: 2480-2491.

Zhao,H. Q., I. F. Macdonald, M. J. Kwiecien. 1994. Multi-orientation scanning: a necessity in the identification of pore necks in porous media by 3-D computer reconstruction from serial section data. *Journal of Colloid and Interface Science*. 162(2): 390-401.

Zolzer, U., and T. Boltze. 1994. Interpolation algorithms: theory and application. In *proceedings 97<sup>th</sup> AES*. *Journal of Audio Engineering Society*. 97, 3898.

## Appendix: Codes

To obtain the pore-network structure, run the following codes according to the following order:

1. Obtain three-dimensional image of the system. If the images are cross-sections, then run the following codes: (file names: `convert_small_slice1.m`, `small_volume_direct_abc1.m`).
2. Depending on the quality of the image, apply a smoothing filter on the image (file name: `read_smooth_right_volume.m`).
3. Segment the image(s) to obtain images(s) with two binary phases (3DMA: case 1.5). 3DMA can be downloaded from : `ftp: ams.sunysb.edu`
4. Run the burning algorithm, the backbone of the medial axis analysis (3DMA: case 2.2).
5. Get the medial axis of the binary image (3DMA: case 3.12). (put the nodes and the paths in different files).
6. Arrange the medial axis in the form of paths and nodes (file name: `read_cluster_modified_final.m`).
7. Put all the segmented files in the same directory and run (file name: `read_all_seg.m`).
8. Get the sizes and locations of pore-bodies (file name: `inscribed_sphere_pores.m`).
9. Get the sizes and locations of pore-throats (file name: `inscribed_sphere_throats.m`).
10. Get the pore-network statistics (file name: `network_info.m`).
11. Modify the pore-network (i.e., merge nodes, etc.) (file name: `merge_nodes.m`).
12. Get the aspect ratio (file name: `aspect_ratio.m`).
13. Get the coordination number (file name: `coord_number.m`).
14. Obtain pore- body-body correlation (file\_names: `unif_data.m` followed by `cor_b_b_krig.m`).
15. Plot the semivariogram (file name: `plot_vario.m`)

```

%%%%%%%%%%%%%%%%%%%%%%%%%%%%%%%%%%%%%%%%%%%%%%%%%%%%%%%%%%%%%%%%%%%%%%%%
%%%%%%%%
%%%%%%%% File name :convert_small_slice1.m
%%%%%%%%
%%%%%%%%%%%%%%%%%%%%%%%%%%%%%%%%%%%%%%%%%%%%%%%%%%%%%%%%%%%%%%%%%%%%%%%%

%make sure that no file name in this directoty starts with (slice_0)
%change dimentions if needed:
clear all

NX=250; % number of rows in the image
NY=250; % Number of columns in the image

all_files=dir;
[numberoffiles, lengtoffiles]=size(all_files);
slices_files=[];
small_slices_files=[];
for k=1:numberoffiles
    temp=all_files(k).name;
    temp=[temp,blanks(40)];
    if strmatch('slice_0',temp)
        slices_files=[slices_files;temp(1:10)];
    end
end

end
[NumberOfSlices,columns]=size(slices_files);
for k=1:length(slices_files)

small_slices_files=[small_slices_files;'small_slice_',num2str(slices_files(k,7:columns))];
    end
    %break

for k=1:NumberOfSlices
    %eval(['file_name = slice_0',num2str(i)]);
    file_name=slices_files(k,:);
    fid = fopen(file_name,'r');
    slice = fread(fid, 'float32');
    fclose(fid);
    %slice=reshape(slice,451,451); %%% the dimnesinos of the slice
    slice=reshape(slice,NX,NY);

    %slice=slice(1:350,26:375); %%%the new dimention
    slice=slice(1:NX,1:NY);

    small_file_name = small_slices_files(k,:)

    fid = fopen(small_file_name,'w');
    count = fwrite(fid,slice,'float32');
    count
    fclose(fid);

```

end

save slice\_maker

```
%%%%%%%%%%%%%%%%%%%%%%%%%%%%%%%%%%%%%%%%%%%%%%%%%%%%%%%%%%%%%%%%%%%%%%%%
%%%%%%%%
%%%%%%%%
%%%%%%%% End of convert_small_slicel.m
%%%%%%%%
%%%%%%%%%%%%%%%%%%%%%%%%%%%%%%%%%%%%%%%%%%%%%%%%%%%%%%%%%%%%%%%%%%%%%%%%
```

```
%%%%%%%%%%%%%%%%%%%%%%%%%%%%%%%%%%%%%%%%%%%%%%%%%%%%%%%%%%%%%%%%%%%%%%%%
%%
%%%%%%%%
%%%%%%%% file name: read_smooth_right_volume.m
%%%%%%%%
%%%%%%%%%%%%%%%%%%%%%%%%%%%%%%%%%%%%%%%%%%%%%%%%%%%%%%%%%%%%%%%%%%%%%%%%
%%%%%%%%
%this code reads a binary file resulted from the reconstruction,
% then smooth it by three different filters
% and then write it again to a binary file....
%this code contains three types of filters:
% 1- linear averaging filter
% 2 - nonlinear averaging filter
% 3- median filter
% modification of this file includes automation of the selection of the
filter and its size
%also automation of the selection of the file to be read
% this code might be added to the end of making a volume file!!!
% note that this file has a function (median3) which is the median
filter, this
% file must be at the same directory.....
%Riyadh AL-Raoush
```

```
file_name='volume_beads2.bin'           %% the name
of the original file
file_name_smoothed='volume_beads2_smooth.bin' %% the name
of the output(the smoothed file)
```

```
NX=250;
NY=250;
NZ=108;
```

```
fid=fopen(file_name,'r')
volume=fread(fid,'unsigned char');
fclose(fid)
```

```
volume=reshape(volume,NX,NY,NZ);
%%volume=volume(:,:,10:13);
volume=volume(:,:,1:NZ);
```

```

volume_dimension=size(volume);
index=1

%%% linear avereging filter

while index < 3
    index=index+1
    volume=smooth3(volume, 'box');
end

%% nonlinear averaging filter

while index < 6
    index=index+1
    volume=median3(volume, 'box');
end

size_volume=size(volume);

fid_volume=fopen(file_name_smoothed, 'a');
for i=1:size_volume(3)
    slice=volume(:, :, i);
    count=fwrite(fid_volume, slice, 'unsigned char');
end

fclose(fid_volume)

break

%%% the following is a median filter
%%%
while index < 7
    index=index+1
    for k=2:volume_dimension(3)-1
        for j=2:volume_dimension(2)-1
            for i=2:volume_dimension(1)-1

                kereneel=volume(i-1:i+1, j-1:j+1, k-1:k+1);
                pixel_value=median(kereneel(:));
                volume(i, j, k)=pixel_value;

            end
        end
    end
end

break
for i=1:108

    slice=volume(:, :, i);

    imagesc(slice);colormap gray;

end

```

```

%%%%%%%%%%%%%%%%%%%%%%%%%%%%%%%%%%%%%%%%%%%%%%%%%%%%%%%%%%%%%%%%%%%%%%%%
%%%%%%%%
%%%%%%%% End of : read_smooth_right_volume.m
%%%%%%%%%%%%%%%%%%%%%%%%%%%%%%%%%%%%%%%%%%%%%%%%%%%%%%%%%%%%%%%%%%%%%%%%

%%%%%%%%%%%%%%%%%%%%%%%%%%%%%%%%%%%%%%%%%%%%%%%%%%%%%%%%%%%%%%%%%%%%%%%%

%%%%%%%%%%%%%%%%%%%%%%%%%%%%%%%%%%%%%%%%%%%%%%%%%%%%%%%%%%%%%%%%%%%%%%%%
%%%%%%%%
%%%%%%%% file name: read_cluster_modified_final.m
%%%%%%%%
%%%%%%%%%%%%%%%%%%%%%%%%%%%%%%%%%%%%%%%%%%%%%%%%%%%%%%%%%%%%%%%%%%%%%%%%
%%%%%%%%%%%%%%%%%%%%%%%%%%%%%%%%%%%%%%%%%%%%%%%%%%%%%%%%%%%%%%%%%%%%%%%%
%this code reads the file that contains information about the
%medial axis and rearn information about pore and thtoat information
%given that the output of the cluster and paths are given
separeltly.....
%....
clear all

Nx=188;    %% number of rows in the image
Ny=200;    %% number of columens in the image
Nz=238;    %% number of slices in the volume

node_file_name='node_all.txt';    %% the name of file that has the nodes
path_file_name='path_all.txt';    %% the name of the file the has the
paths

line=[];
cluster_line=[];
path_length=[];
path_radius=[];
path_line=[];
real_path_line=[];
attList_line=[];
attclus_line=[];
cluster_id=[];
location_id=[];
bleft=[];
bright=[];
location_cluster=[];
location_path=[];
new_attached_path_size=[];
final_attached_path=[];
max_burn=[];
min_burn=[];
cluster_size=[];
temp_path_cluster=[];
cluster_x=[];
cluster_y=[];
cluster_z=[];

```

```

temp_cluster_x=[];
temp_cluster_y=[];
temp_cluster_z=[];
pore_radius=[];
throat_size=[];

all_file =
textread(node_file_name,'%s','delimiter','\n','whitespace','');

mark1='Cluster ';
mark2='attached list';
mark3=': ';
mark4='[';
mark5=']';
mark6='(';
mark7=)';
mark8='attached paths';
mark9='Path';
mark10='length';
mark11='attached clusters';
mark12='NULL';
mark13=', ';

for i=1:size(all_file,1)
    all_file_i=i
    eval(['line_' num2str(i) '=cell2mat(all_file(i));']);
    eval(['if isempty(findstr(line_' num2str(i) ',mark1))==0;
cluster_line =[cluster_line;i]; end ;']);
    eval(['if isempty(findstr(line_' num2str(i) ',mark2))==0;
attList_line =[attList_line;i]; end ;']);
end

for i=1:size(cluster_line,1)
    cluster_line_i=i
    eval(['location_id(i)=findstr(line_' num2str(cluster_line(i))
',mark3);']);

    eval(['cluster_id(i,:)= str2num(line_' num2str(cluster_line(i))...
'(location_id(i)+1:length(line_' num2str(cluster_line(i)) ')'-
1));']);
    eval(['burn_' num2str(i) '=[]; ']);
    eval(['allxyz_' num2str(i) '=[]; ']);
    eval(['xyz_' num2str(i) '=[]; ']);
    eval(['attached_path_' num2str(i) '=[]; ']);
end;

for i=1:size(cluster_line,1)
    second_cluster_line=i

```

```

for k=(cluster_line(i)+1):attList_line(i)-1
    eval(['bleft=findstr(line_'num2str(k) ',mark4);']);
    eval(['bright=findstr(line_'num2str(k) ',mark5);']);
    eval(['qlleft=findstr(line_'num2str(k) ',mark6);']);
    eval(['qright=findstr(line_'num2str(k) ',mark7);']);

    for m=1:length(bleft)

        eval(['burn_'num2str(i) '=[burn_'num2str(i)
';str2num(line_'num2str(k)...
        '(bleft(m)+1:bright(m)-1 )];']);

        eval(['allxyz_'num2str(i) '=[allxyz_'num2str(i)
';(line_'num2str(k)...
        '(qlleft(m):qright(m) )];']);

    end
end
eval(['MAXburn_' num2str(i) '=find(burn_'num2str(i)
'==max(burn_'num2str(i) ')');']);
eval(['xyz_'num2str(i) '=allxyz_'num2str(i) '(MAXburn_'num2str(i)
'(1),:);']);

end
%%%%%%%%%%%%%%%%%%%%%%%%%%%%%%%%%%%%%%%%%%%%%%%%%%%%%%%%%%%%%%%%%%%%%%%%
%%%%%%%%%%%%%%%%%%%%%%%%%%%%%%%%%%%%%%%%%%%%%%%%%%%%%%%%%%%%%%%%%%%%%%%%
clear allxyz* all_file MAXburn*
%%%%%%%%%%%%%%%%%%%%%%%%%%%%%%%%%%%%%%%%%%%%%%%%%%%%%%%%%%%%%%%%%%%%%%%%
%%%%%%%%%%%%%%%%%%%%%%%%%%%%%%%%%%%%%%%%%%%%%%%%%%%%%%%%%%%%%%%%%%%%%%%%

path_file =
textread(path_file_name,'%s','delimiter','\n','whitespace','');

for i=1:size(path_file,1)

    path_file_i=i
    eval(['line_' num2str(i) '=cell2mat(path_file(i));']);
    eval(['if isempty(findstr(line_' num2str(i) ',mark9))==0; path_line
=[path_line;i]; end ;']);
    eval(['if isempty(findstr(line_' num2str(i) ',mark11))==0;
attclus_line =[attclus_line;i]; end ;']);
end

for i=1:size(attclus_line,1)

    eval(['if isempty(findstr(line_' num2str(attclus_line(i)+1)
',mark12))==1; real_path_line =[real_path_line;i]; end ;']);
end

```

```

for i=1:size(real_path_line,1)
    real_path_one=i

eval(['temp_path_length=str2num(line_'num2str(path_line(real_path_line(
i))+1)...
    '(length(mark10)+1:length(line_'
num2str(path_line(real_path_line(i))+1) '));']);

    path_length=[temp_path_length; path_length];
end

%%%%%%%%%%

for i=1:size(real_path_line,1)

    eval(['path_burn_'num2str(i) '=[]; ']);
    eval(['path_allxyz_'num2str(i) '=[]; ']);
    eval(['path_xyz_'num2str(i) '=[]; ']);
end;

for i=1:size(real_path_line,1)
    real_path_two=i

    for
k=(path_line(real_path_line(i))+1):attclus_line(real_path_line(i))-1
        eval(['bleft=findstr(line_'num2str(k) ',mark4);']);
        eval(['bright=findstr(line_'num2str(k) ',mark5);']);
        eval(['qleft=findstr(line_'num2str(k) ',mark6);']);
        eval(['qright=findstr(line_'num2str(k) ',mark7);']);

        for m=1:length(bleft)

            eval(['path_burn_'num2str(i) '=[path_burn_'num2str(i)
';str2num(line_'num2str(k)...
                '(bleft(m)+1:bright(m)-1 )];']);

            eval(['path_allxyz_'num2str(i) '=[path_allxyz_'num2str(i)
';(line_'num2str(k)...
                '(qleft(m):qright(m) )];']);

        end
    end

    eval(['MINburn_'num2str(i) '=find(path_burn_'num2str(i)
'==min(path_burn_'num2str(i) '));']);
    eval(['minburn_'num2str(i) '=min(path_burn_'num2str(i) ');']);
    %eval(['path_xyz_'num2str(i) '=path_allxyz_'num2str(i)
'(MINburn_'num2str(i) '(1),:);']);

    %the following two lines give the midille value of the burn number
along the path

    eval(['path_xyz_'num2str(i)...

```

```

        '=path_allxyz_'num2str(i) '((round(length(MINburn_'num2str(i)
    ')/2)-1)+MINburn_'num2str(i) '(1),:);');
        eval(['path_cluster_'num2str(i) '=[;]');

        eval(['temp_path_cluster_'num2str(i) '=[;]');

        %eval(['clear allxyz_'num2str(i)
end

%for i=1:length(cluster_line)

    for k=1:length(real_path_line)

        real_path_line_i=k

eval(['comma_location=findstr(line_'num2str(attclus_line(real_path_line
(k))+1) ',mark13);']);

        eval(['close_cluster_1
=str2num(line_'num2str(attclus_line(real_path_line(k))+1)...
        '(1:comma_location-1 )');']);

        eval(['close_cluster_2
=str2num(line_'num2str(attclus_line(real_path_line(k))+1)...
        '(comma_location+1:length(line_'num2str(attclus_line(real_path_line(k))
+1) '))');']);

        % if close_cluster_1==cluster_id(i)
        % eval(['temp_attached_path_' num2str(i) '=k;']);
        % eval(['attached_path_' num2str(i) '=[temp_attached_path_'
num2str(i) ';attached_path_' num2str(i) '];']);

        % eval(['temp_path_cluster_' num2str(k) '=i;']);
        % eval(['path_cluster_' num2str(k) '=[temp_path_cluster_'
num2str(k) ';path_cluster_' num2str(k) '];'])
        %else

        % eval(['temp_attached_path_' num2str(i) '=[;]');
        %eval(['attached_path_' num2str(i) '=[temp_attached_path_'
num2str(i) ';attached_path_' num2str(i) '];']);

        % eval(['temp_path_cluster_' num2str(k) '=[];']);
        %eval(['path_cluster_' num2str(k) '=[temp_path_cluster_'
num2str(k) ';path_cluster_' num2str(k) '];'])

    % end

%%%%%% this is a modification of the above sectin

        aaa=find(cluster_id==close_cluster_1);
        eval(['temp_attached_path_' num2str(aaa) '=k;']);
        eval(['attached_path_' num2str(aaa) '=[temp_attached_path_'
num2str(aaa) ';attached_path_' num2str(aaa) '];']);

```

```

        eval(['temp_path_cluster_' num2str(k) '=aaa;']);
        eval(['path_cluster_' num2str(k) '=[temp_path_cluster_'
num2str(k) ';path_cluster_' num2str(k) '];']);

        %if close_cluster_2==cluster_id(i)
        % eval(['temp_attached_path_' num2str(i) '=k;']);
        % eval(['attached_path_' num2str(i) '=[temp_attached_path_'
num2str(i) ';attached_path_' num2str(i) '];']);

        %eval(['temp_path_cluster_' num2str(k) '=i;']);
        %eval(['path_cluster_' num2str(k)
'=[temp_path_cluster_' num2str(k) ';path_cluster_' num2str(k) '];'])

%     else

        bbb=find(cluster_id==close_cluster_2);
        eval(['temp_attached_path_' num2str(bbb) '=k;']);
        eval(['attached_path_' num2str(bbb) '=[temp_attached_path_'
num2str(bbb) ';attached_path_' num2str(bbb) '];']);
        eval(['temp_path_cluster_' num2str(k) '=bbb;']);
        eval(['path_cluster_' num2str(k)
'=[temp_path_cluster_' num2str(k) ';path_cluster_' num2str(k) '];'])

        % eval(['temp_attached_path_' num2str(i) '=[];']);
        %eval(['attached_path_' num2str(i) '=[temp_attached_path_'
num2str(i) ';attached_path_' num2str(i) '];']);

        %eval(['temp_path_cluster_' num2str(k) '=[];']);
%eval(['path_cluster_' num2str(k) '=[temp_path_cluster_' num2str(k)
';path_cluster_' num2str(k) '];'])

        end

    %end

%end

%=====
=====
clear path_line line_* path_allxyz* path_xyz*

%=====
=====

for i=1:length(cluster_line)

    eval(['location_cluster=[location_cluster;xyz_' num2str(i) '];']);
    eval(['new_attached_path_' num2str(i) '=attached_path_' num2str(i)
'(find(attached_path_' num2str(i) '>0));']);

```

```

eval(['new_attached_path_size=[new_attached_path_size;size(new_attached
_path_' num2str(i) ',1)];']);
end

for i=1:length(cluster_line)
    % eval(['all_attached_path_'num2str(i)
    '=zeros(1,max(new_attached_path_size));']);
    eval(['all_attached_path_'num2str(i)
    '=zeros(1,max(max(new_attached_path_size));']);
    eval(['all_attached_path_'num2str(i)
    '(1:length(new_attached_path_'num2str(i)...
    '))=new_attached_path_' num2str(i) ';']);
    eval(['final_attached_path=[final_attached_path;
all_attached_path_'num2str(i) '];']);
    eval(['max_burn=[max_burn; max(burn_'num2str(i) ')];']);

end

for i=1:length(cluster_line)
    temp_cluster_size=(max_burn(i)/sum(max_burn))*(Nx*Ny*Nz*.47);
    temp_pore_radius=(temp_cluster_size*3/(pi*4))^(1/3);
    cluster_size=[temp_cluster_size;cluster_size];
    pore_radius=[temp_pore_radius;pore_radius];

    eval(['comma_location1=findstr(xyz_'num2str(i) ',mark13);']);
    eval(['temp_cluster_x=str2num(xyz_'num2str(i)
    '(1,(2:comma_location1(1)-1));']);
    eval(['temp_cluster_y=str2num(xyz_'num2str(i)
    '(1,comma_location1(1)+1:comma_location1(2)-1));']);
    eval(['temp_cluster_z=str2num(xyz_'num2str(i)
    '(1,(comma_location1(2)+1):length(xyz_'num2str(i) ')-1));']);
    cluster_x=[temp_cluster_x;cluster_x];
    cluster_y=[temp_cluster_y;cluster_y];
    cluster_z=[temp_cluster_z;cluster_z];
end

%burn_voxel_ratio=pore_radius(1)/max_burn(1);

location_cluster_new=zeros(size(location_cluster,1),3);
for i=1:size(location_cluster_new,1)
    [x_limit]=findstr(location_cluster(i,:),mark13);
    location_cluster_new(i,1)=str2num(location_cluster(i,2:x_limit(1)-
1));

location_cluster_new(i,2)=str2num(location_cluster(i,x_limit(1)+1:x_lim
it(2)-1));

location_cluster_new(i,3)=str2num(location_cluster(i,x_limit(2)+1:size(
location_cluster,2)-1));
end

location_path_new=zeros(size(location_path,1),3);
for i=1:size(location_path_new,1)

```

```

[x_limit]=findstr(location_path(i,:),mark13);
location_path_new(i,1)=str2num(location_path(i,2:x_limit(1)-1));

location_path_new(i,2)=str2num(location_path(i,x_limit(1)+1:x_limit(2)-
1));

location_path_new(i,3)=str2num(location_path(i,x_limit(2)+1:size(location_
path,2)-1));
end

%%%%%%%%%%%%%%
clear line*
%%%%%%%%%%%%%%

number_find_close=[];
x_pore_new=[];
[x_neighbor y_neighbor]=size(final_attached_path);

pore_neighbor=zeros(x_neighbor,y_neighbor);

for i=1:x_neighbor
    number_find_close=[];
    x_pore_new=[];
    [find_close]=find(final_attached_path(i,:) >0 );

    for k=1:length(find_close)

number_find_close=[number_find_close,final_attached_path(i,find_close(k
))];
end

    for q=1: length(number_find_close)
        [x_pore J]=find(final_attached_path == number_find_close(q));
        x_pore_new=[x_pore_new;x_pore];
    end

    for g=1:length(x_pore_new)
        if x_pore_new(g)== i
            x_pore_new(g)=0;
        end
    end

    for h=2:length(x_pore_new)
        if x_pore_new(h)== x_pore_new(h-1)
            x_pore_new(h)=0;
        end
        x_pore_new=fliplr((sort(x_pore_new')));
    end

    pore_neighbor(i,1:length(x_pore_new))=x_pore_new;
end

```

```

    x_position=location_cluster_new(:,1);
    y_position=location_cluster_new(:,2);
    z_position=location_cluster_new(:,3);
    radius=pore_radius;

for i=1:length(real_path_line)

    eval(['location_path=[location_path;path_xyz_' num2str(i) '];']);
    %eval(['min_burn=[min_burn; min(path_burn_'num2str(i) ')];']);
    %temp_throat_size=min_burn(i)*3;
    %throat_size=[temp_throat_size;throat_size];
    eval(['path_length(i)=( (x_position(path_cluster_'num2str(i) '(1))-
x_position(path_cluster_'num2str(i) '(2)))^2'...
        '(y_position(path_cluster_'num2str(i) '(1))-
y_position(path_cluster_'num2str(i) '(2)))^2'...
        '(z_position(path_cluster_'num2str(i) '(1))-
z_position(path_cluster_'num2str(i) '(2)))^2)^(.5);']);

    end

%%%%%%this is the addition of the final version%%%%%%%%
location_path_new=zeros(size(location_path,1),3);

for i=1:size(location_path_new,1)
    [x_limit]=findstr(location_path(i,:),mark13);
    location_path_new(i,1)=str2num(location_path(i,2:x_limit(1)-1));

location_path_new(i,2)=str2num(location_path(i,x_limit(1)+1:x_limit(2)-
1));

location_path_new(i,3)=str2num(location_path(i,x_limit(2)+1:size(locati
on_path,2)-1));
end

location_path_new=uint16(location_path_new);
location_cluster_new=uint16(location_cluster_new);
final_attached_path=uint16(final_attached_path);
pore_neighbor=uint16(pore_neighbor);

save read_cluster_modified_final location_path_new
location_cluster_new pore_neighbor path_length final_attached_path

%%%%%%%%%%%%%%
%%
%%
%% End: read_cluster_modified_final.m

%%
%%%%%%%%%%%%%%

```

```

%%%%%%%%%%%%%%%%%%%%%%%%%%%%%%%%%%%%%%%%%%%%%%%%%%%%%%%%%%%%%%%%%%%%%%%%
%%%%%% file name: read_all_seg.m
%%%%%%%%%%%%%%%%%%%%%%%%%%%%%%%%%%%%%%%%%%%%%%%%%%%%%%%%%%%%%%%%%%%%%%%%

NumberOfrows=188;      %%% variable
NumberOfColumns=200;   %%% variable
NumberOfFiles=238;     %%% variable

file_name = 'oid_made_3D' % the output file--

%%%% note that the segmented files should be named: "seg1.01, seg1.02
,seg1.--"

volume2=uint8(zeros(NumberOfrows,NumberOfColumns,NumberOfFiles));

seg_files = []; zeros_string = '000';
for i = 1:NumberOfFiles
    temp = num2str(i);
    seg_files = [seg_files; 'seg1.',zeros_string(1:(3-
length(temp))),temp];
end;

for i=1:NumberOfFiles
    file_name=[seg_files(i,:)];
    fid = fopen(file_name,'r','b');
    [slice,elements] = fread(fid,'ubit1');

fclose(fid);
slicel=slice((elements-(NumberOfrows*NumberOfColumns)+1):elements,:);

eval(['slice'num2str(i)
'=reshape(slicel,NumberOfrows,NumberOfColumns);']);

%slice_new=reshape(slicel,NumberOfrows,NumberOfColumns);

eval(['volume2(:, :, i)=uint8(slice'num2str(i) ');']);

%imagesc(slice2);colormap gray; axis image;

end

fid_volume = fopen(file_name,'a');

for j = 1:NumberOfFiles
    data_format='unsigned char';
    eval(['count = fwrite(fid_volume, slice'num2str(j)
',data_format);']);
end;

fclose(fid_volume)

save make_spheres volume2

```

```

%%%%%%%%%%%%%%%%%%%%%%%%%%%%%%%%%%%%%%%%%%%%%%%%%%%%%%%%%%%%%%%%%%%%%%%%
%%
%% End of : read_all_seg.m
%%
%%%%%%%%%%%%%%%%%%%%%%%%%%%%%%%%%%%%%%%%%%%%%%%%%%%%%%%%%%%%%%%%%%%%%%%%

%%%%%%%%%%%%%%%%%%%%%%%%%%%%%%%%%%%%%%%%%%%%%%%%%%%%%%%%%%%%%%%%%%%%%%%%
%%
%% File name: inscribed_sphere_pores.m
%
%%%%%%%%%%%%%%%%%%%%%%%%%%%%%%%%%%%%%%%%%%%%%%%%%%%%%%%%%%%%%%%%%%%%%%%%
% this file calculates the pore-bodies in the network
%
%
%this file runs after: read_cluster.m
%%
%% input file: binary data of the volume (file name: make_spheres)
%
%=====
clear all;

%volume2 is the the binary granis volume
%
%
%nx,ny and nz are the sizes of the volume
%
%

load make_spheres
load read_cluster_modified_final

nx=300;    %%% Number of rows in the image
ny=300;    %%% number of columns in the image
nz=450;    %% number of slices in the image
resolution=1;
%%%%%%%%%%%%%%%%%%%%%%%%%%%%%%%%%%%%%%%%%%%%%%%%%%%%%%%%%%%%%%%%%%%%%%%%
x_position=location_cluster_new(:,1);
y_position=location_cluster_new(:,2);
z_position=location_cluster_new(:,3);

n=length(x_position);
pore_radius=zeros(n,1);
r=resolution*pore_radius;

a=uint8(zeros(nx,ny,nz));
n=length(x_position); %%

x_cor=double(x_position)+1;
y_cor=double(y_position)+1;

```

```

z_cor=double(z_position)+1;
%=====

test_location=0;

for m=1:n

    pore_number=m
    while max(max(test_location(:))) <2
        r(m)=r(m)+1;
        for k=0:r(m)
            for j=0:r(m)

                x=real(floor(sqrt(r(m)^2-(j^2)-(k^2))));

                for i=0:x

                    y=real(floor(sqrt(r(m)^2-(i^2)-(k^2))));

                    a1=x_cor(m)+i;
                    a2=y_cor(m);
                    a3=y_cor(m)+y;
                    a4=y_cor(m)-y;
                    a5=x_cor(m)-i;
                    a6=z_cor(m)+k;
                    a7=z_cor(m)-k;

                    if a1> nx %size(a,1)
                        a1=nx; %size(a,1);
                    end
                    if a3>ny %size(a,2)
                        a3=ny; %size(a,2);
                    end
                    if a4 <=0
                        a4=1;
                    end
                    if a5 <= 0
                        a5=1;
                    end
                    if a6>nz %size(a,3)
                        a6=nz; %size(a,3);
                    end
                    if a7<=0
                        a7=1;
                    end

                    a(a1,a2:a3,a6)=1;
                    a(a1,a4:a2,a6)=1;
                    a(a5,a2:a3,a6)=1;
                    a(a5,a4:a2,a6)=1;
                    a(a1,a2:a3,a7)=1;
                    a(a1,a4:a2,a7)=1;
                    a(a5,a2:a3,a7)=1;

```

```

a(a5,a4:a2,a7)=1;

end

end
end
test_location=double(volume2(:,:,a7:a6))+double(a(:,:,a7:a6));
end

a(:)=0;
test_location=0;
end
pore_radius=r;

save inscribed_sphere_pores pore_radius x_position y_position
z_position

%%%%%%%%%%%%%%%%%%%%%%%%%%%%%%%%%%%%%%%%%%%%%%%%%%%%%%%%%%%%%%%%%%%%%%%%
%
%
%
% end of inscribed_sphere_pores.m
%%%%%%%%%%%%%%%%%%%%%%%%%%%%%%%%%%%%%%%%%%%%%%%%%%%%%%%%%%%%%%%%%%%%%%%%5

%%%%%%%%%%%%%%%%%%%%%%%%%%%%%%%%%%%%%%%%%%%%%%%%%%%%%%%%%%%%%%%%%%%%%%%%
%
% File name: inscribed_sphere_throats.m
%
%%%%%%%%%%%%%%%%%%%%%%%%%%%%%%%%%%%%%%%%%%%%%%%%%%%%%%%%%%%%%%%%%%%%%%%%
% this file calculats the pore_throats of the pore_network
%
% This file runs after: read_cluster_modified_final.m
%
% input file: binry data of the volume (file name : make_spheres)
%
%
%
clear all;

%% nx,ny, and nz are the sizes of the volume

load read_cluster_modified_final
load make_spheres %volume2 is the the
binarty granis volume
load read_cluster_modified_final

```

```

nx=300;%Nx;
ny=300;%Ny;
nz=450;%Nz;
resolution=1;

%%this is in case of throats only-----
x_position=location_path_new(:,1);
y_position=location_path_new(:,2);
z_position=location_path_new(:,3);
%%%%%%%%%%%%%%%%%%%%%%%%%%%%%%%%%%%%%%%%%%%%%%%%%%%%%%%%%%%%%%%%%%%%%%%%

n=length(x_position);
pore_radius=zeros(n,1);
r=resolution*pore_radius;

a=uint8(zeros(nx,ny,nz));
n=length(x_position); %%

x_cor=double(x_position)+1;
y_cor=double(y_position)+1;
z_cor=double(z_position)+1;
%%%%%%%%%%%%%%%%%%%%%%%%%%%%%%%%%%%%%%%%%%%%%%%%%%%%%%%%%%%%%%%%%%%%%%%%

test_location=0;

for m=1:n

    throat_number=m

while max(max(test_location(:))) <2
    r(m)=r(m)+1;
    for k=0:r(m)
        for j=0:r(m)

            x=real(round(sqrt(r(m)^2-(j^2)-(k^2))));

            for i=0:x

                y=real(round(sqrt(r(m)^2-(i^2)-(k^2))));

                a1=x_cor(m)+i;
                a2=y_cor(m);
                a3=y_cor(m)+y;
                a4=y_cor(m)-y;
                a5=x_cor(m)-i;
                a6=z_cor(m)+k;
                a7=z_cor(m)-k;

                if a1> nx %size(a,1)
                    a1=nx; %size(a,1);
                end
                if a3>ny %size(a,2)
                    a3=ny; %size(a,2);
                end
            end
        end
    end
end

```

```

if a4 <=0
    a4=1;
end
if a5 <= 0
    a5=1;
end
if a6>nz %size(a,3)
    a6=nz; %size(a,3);
end
if a7<=0
    a7=1;
end

a(a1,a2:a3,a6)=1;
a(a1,a4:a2,a6)=1;
a(a5,a2:a3,a6)=1;
a(a5,a4:a2,a6)=1;
a(a1,a2:a3,a7)=1;
a(a1,a4:a2,a7)=1;
a(a5,a2:a3,a7)=1;
a(a5,a4:a2,a7)=1;

end

end
end
% test_location=double(volume2)+double(a);
test_location=double(volume2(:, :, a7:a6))+double(a(:, :, a7:a6));
end

a(:)=0;
test_location=0;
end

throat_radius=r;

save inscribed_sphere_throats throat_radius

%%%%%%%%%%%%%%%%%%%%%%%%%%%%%%%%%%%%%%%%%%%%%%%%%%%%%%%%%%%%%%%%%%%%%%%%
%
%
% end of inscribed_sphere_throats.m
%
%%%%%%%%%%%%%%%%%%%%%%%%%%%%%%%%%%%%%%%%%%%%%%%%%%%%%%%%%%%%%%%%%%%%%%%%
%%%%%%%%

```

```

%%%%%%%%%%%%%%%%%%%%%%%%%%%%%%%%%%%%%%%%%%%%%%%%%%%%%%%%%%%%%%%%%%%%%%%%
%
%%% file name: network_info.m
%%
%%%%%%%%%%%%%%%%%%%%%%%%%%%%%%%%%%%%%%%%%%%%%%%%%%%%%%%%%%%%%%%%%%%%%%%%
%%
%%% this codes gives the complete information about the network
%
% this file runs after : (1) read_cluster.m (2)
inscribed_sphere_pores.m (3) inscribed_sphere_throats.m
%
%

voxel_cut=5; %this is the cut arround the boundary----

load read_cluster_modified_final
load inscribed_sphere_pores
load inscribed_sphere_throats

%%%%%%%%
%%% the sizes of the volume
%%%%%%%%

Nx=300;
Ny=300;
Nz=450;

max_x_limit=Nx-voxel_cut;
max_y_limit=Ny-voxel_cut;
max_z_limit=Nz-voxel_cut;

for i=1:length(location_cluster_new)

    if location_cluster_new(i,1) <= voxel_cut
        location_cluster_new(i,:)=0;
    end

    if location_cluster_new(i,2) <= voxel_cut
        location_cluster_new(i,:)=0;
    end

    if location_cluster_new(i,3) <= voxel_cut
        location_cluster_new(i,:)=0;
    end

    if location_cluster_new(i,1) >= max_x_limit
        location_cluster_new(i,:)=0;
    end

    if location_cluster_new(i,2) >= max_y_limit
        location_cluster_new(i,:)=0;
    end

    if location_cluster_new(i,3) >= max_z_limit
        location_cluster_new(i,:)=0;
    end
end

```

```
end
```

```
for i=1:length(location_path_new)
```

```
%%%%%%%% all this below
```

```
    if location_path_new(i,1) <= voxel_cut
        location_path_new(i,:)=0;
    end
```

```
    if location_path_new(i,2) <= voxel_cut
        location_path_new(i,:)=0;
    end
```

```
    if location_path_new(i,3) <= voxel_cut
        location_path_new(i,:)=0;
    end
```

```
    if location_path_new(i,1) >= max_x_limit
        location_path_new(i,:)=0;
    end
```

```
    if location_path_new(i,2) >= max_y_limit
        location_path_new(i,:)=0;
    end
```

```
    if location_path_new(i,3) >= max_z_limit
        location_path_new(i,:)=0;
    end
```

```
end
```

```
%%% up to this point
```

```
%in case you want the whole domain just put "=" sign below and change  
the voxel_cut above to "0"
```

```
[wanted_pores]=find(location_cluster_new(:,1) >= voxel_cut );  
[wanted_throats]=find(location_path_new(:,1) >= voxel_cut );  
%%%%%%%%
```

```
[a_x b_y]=size(final_attached_path);  
%%%%%%%% also this
```

```
aaa=final_attached_path';  
bbb=reshape(aaa,1,a_x*b_y);
```

```
for i=1:length(bbb)  
    [change_throat]=find(wanted_throats==bbb(i));
```

```

        if length(change_throat) <1
            bbb(i)=0;
        end
    end
end

bbb=reshape(bbb,b_y,a_x);
final_attached_path=bbb';

%%%%% this is the extra%%%%%

extra_path_1=mean(path_length);
path_length=[extra_path_1;path_length];

location_cluster_new=location_cluster_new(wanted_pores,:);
pore_radius=pore_radius(wanted_pores,:);
pore_neighbor=pore_neighbor(wanted_pores,:);
final_attached_path=final_attached_path(wanted_pores,:);

location_path_new=location_path_new(wanted_throats,:);
throat_radius=throat_radius(wanted_throats,:);
path_length=path_length(wanted_throats,:);

%break

clear pore_info* throat_info*
pore_info.number=length(wanted_pores);
pore_info.location=location_cluster_new;
pore_info.radius_voxel=pore_radius;
pore_info.neighbor_pores=pore_neighbor;
pore_info.attached_path=final_attached_path;

throat_info.number=length(wanted_throats);
throat_info.number=length(location_path_new);
throat_info.radius_voxel=throat_radius;
throat_info.length=path_length;
throat_info.location=location_path_new;

save network_info_cut pore_info throat_info

%%%%%%%% %%%%%%%%%%%%%%%%%%%%%%%%%%%%%%%
%
% %
% end of network_info.m
%%%
%%%%%%%% %%%%%%%%%%%%%%%%%%%%%%%%%%%%%%%

```

```

%%%%%%%%%%%%%%%%%%%%%%%%%%%%%%%%%%%%%%%%%%%%%%%%%%%%%%%%%%%%%%%%%%%%%%%%
%%
%% file name: merge_nodes_new.m
%%
%%%%%%%%%%%%%%%%%%%%%%%%%%%%%%%%%%%%%%%%%%%%%%%%%%%%%%%%%%%%%%%%%%%%%%%%
load network_info

R_pores=double(pore_info.location);
R_radius=double(pore_info.radius_voxel);
R_conec=[];
remove_list=[];
neighbor_index=[];

pore_info.location=double(pore_info.location);
pore_info.radius_voxel=double(pore_info.radius_voxel);

for r=1:length(R_pores)

    temp_all_location=pore_info.location;
    %temp_all_location(r,:)=[];
    temp_all_radius=pore_info.radius_voxel;
    %temp_all_radius(r,:)=[];

    x_square=(pore_info.location(r,1)-temp_all_location(:,1)).^2;
    y_square=(pore_info.location(r,2)-temp_all_location(:,2)).^2;
    z_square=(pore_info.location(r,3)-temp_all_location(:,3)).^2;

    temp_dis=sqrt(x_square+y_square+z_square);
    temp_radius=pore_info.radius_voxel(r)+temp_all_radius(:);
    dis_radius=temp_dis-temp_radius;

    %remove_pores=find(dis_radius <= 0);    %%% choose this for the
overlap or touch

    remove_pores=find(temp_dis ==0);        %%% choose this if there is
pores at the same location ONLY..

    %%%%%%%%%%%%%%%%%%%%%%%%%%%%%%%%%%%%%%%%%%%%%%%%%%%%%%%%%%%%%%%%%%%%%%%%%
    % conditions:
    % <= 0 touch or overlap;;; remove_pores=find(dis_radius == 0);
    % = 0 remove pore from the same location;;;
remove_pores=find(temp_dis ==0);
    %%%%%%%%%%%%%%%%%%%%%%%%%%%%%%%%%%%%%%%%%%%%%%%%%%%%%%%%%%%%%%%%%%%%%%%%%
    %
    %

    removed_pores_radius=pore_info.radius_voxel(remove_pores);
    kept_pores=find(removed_pores_radius==max(removed_pores_radius(:)));
    remove_pores(kept_pores(1))=[];
    remove_list=[remove_list;remove_pores];

end

```

```

for k=1:length(remove_list)

    temp_neighbor_index=find(pore_info.neighbor_pores ==
remove_list(k));
    neighbor_index=[neighbor_index;temp_neighbor_index];

end

pores_index=pore_info.location;
pores_index(remove_list)=-11;
pores_index=find(pores_index == -11);

pore_info.neighbor_pores(neighbor_index)=0;
pore_info.location(pores_index,:)=[];
pore_info.radius_voxel(pores_index,:)=[];
pore_info.neighbor_pores(pores_index,:)=[];
pore_info.attached_path(remove_list,:)=[];
pore_info.number=length(pore_info.location);

for i=1:length(pores_index)
    temp_a=find(pore_info.neighbor_pores > pores_index(i));
    pore_info.neighbor_pores(temp_a)=pore_info.neighbor_pores(temp_a)-1;
end

save merge_nodes pore_info throat_info

%%%%%%%%%%%%%%%%%%%%%%%%%%%%%%%%%%%%%%%%%%%%%%%%%%%%%%%%%%%%%%%%%%%%%%%%
%%
%% end of: merge_nodes_new.m
%%
%%%%%%%%%%%%%%%%%%%%%%%%%%%%%%%%%%%%%%%%%%%%%%%%%%%%%%%%%%%%%%%%%%%%%%%%

%%%%%%%%%%%%%%%%%%%%%%%%%%%%%%%%%%%%%%%%%%%%%%%%%%%%%%%%%%%%%%%%%%%%%%%%
% file name: aspect_raio.m
%%%%%%%%%%%%%%%%%%%%%%%%%%%%%%%%%%%%%%%%%%%%%%%%%%%%%%%%%%%%%%%%%%%%%%%%
%
% this file calculates the aspect ratio of the system
%
% this file calcuates the aspet raio and runs after : network_info.m
%

load network_info

%voxel_cut=13;

```

```

%%% volume dimentions
%%%
nx=300;
ny=300;
nz=450;

aspect_ratios=[];

for i=1:length(pore_info.location)

    throat_index=(pore_info.attached_path(i,:)>0);
    throat_number=(pore_info.attached_path(i,throat_index));

    % for k=1:length(throat_number)

temp_aspect_ratios=throat_info.radius_voxel(throat_number)./pore_info.r
adius_voxel(i);
    aspect_ratios=[aspect_ratios;temp_aspect_ratios];

    end

    A_ratio=mean(aspect_ratios)

break

min_bin=min(min(aspect_ratios));
max_bin=max(max(aspect_ratios));
%incr_bin=(max_bin-min_bin)/100;
%binsize=min_bin:incr_bin:max_bin;
binsize=0:.25:5;
hist(aspect_ratios(:,1),binsize)
axis([0 5 0 2000])
h = findobj(gca,'Type','patch');
set(h,'FaceColor','g','EdgeColor','k')
xlabel('throat radius')
ylabel('number of throats')
title('DT (Random)')

load make_spheres

nx=size(volume2,1);
ny=size(volume2,2);
nz=size(volume2,3);

volume3=volume2(voxel_cut+1:nx-voxel_cut,voxel_cut+1:ny-
voxel_cut,voxel_cut+1:nz-voxel_cut);

porosity1=find(volume3==0);

%porosity=porosity/(size(volume3,1)*size(volume3,2)*size(volume3,3));

%%%
%%% this is to get the fraction of the total volume that is

```

```
%fraction=sum((4/3*pi).*pore_info.radius_voxel.^3)/(nx*ny*nz*porosity)
```

```
%%%%%%%%%%%%%%%%%%%%%%%%%%%%%%%%%%%%%%%%%%%%%%%%%%%%%%%%%%%%%%%%%%%%%%%%%  
%%  
%% end of aspect_ratio.m  
%%  
%%%%%%%%%%%%%%%%%%%%%%%%%%%%%%%%%%%%%%%%%%%%%%%%%%%%%%%%%%%%%%%%%%%%%%%%%
```

```
%%%%%%%%%%%%%%%%%%%%%%%%%%%%%%%%%%%%%%%%%%%%%%%%%%%%%%%%%%%%%%%%%%%%%%%%%  
%%  
%% file name: coor_number.m  
%  
%%%%%%%%%%%%%%%%%%%%%%%%%%%%%%%%%%%%%%%%%%%%%%%%%%%%%%%%%%%%%%%%%%%%%%%%%  
%  
% This code calculates the coordination number of the system  
%  
%  
% it runs after: network_info.m  
%%%%%%%%%%%%%%%%%%%%%%%%%%%%%%%%%%%%%%%%%%%%%%%%%%%%%%%%%%%%%%%%%%%%%%%%%
```

```
load network_info  
  
coor_matrix=[];  
  
for i=1:length(pore_info.attached_path)  
    temp_coor_matrix=find(pore_info.attached_path(i,:)>0);  
    coor_matrix=[coor_matrix,temp_coor_matrix];  
  
end
```

```
coor_number=length(coor_matrix)/i;  
  
%%%%%%%%%%%%%%%%%%%%%%%%%%%%%%%%%%%%%%%%%%%%%%%%%%%%%%%%%%%%%%%%%%%%%%%%%  
% end of coor_number.m  
%%  
%%%%%%%%%%%%%%%%%%%%%%%%%%%%%%%%%%%%%%%%%%%%%%%%%%%%%%%%%%%%%%%%%%%%%%%%%  
%
```

```
=====
```

```
%  
% Name of the file cor_b_b_krig.m  
%%  
% this code calculates the body-body spatial correlation (indicator  
semivariogram)  
%%  
%% this file runs after : (1) network_info.m (2) unif_data.m
```

```

%%
%
load network_info

lag_number=10;    %number of lages

pore_info.location=double(pore_info.location);
pore_info.attached_path=double(pore_info.attached_path);
pore_info.radius_voxel=double(pore_info.radius_voxel);

throat_info.location=double(throat_info.location);

load unif_data

gamma_value=zeros(1,lag_number);
lag_piars=zeros(1,lag_number);
k=1;

temp_neighbor_one=[];
temp_number_one=[];
number=0;
sum_diff_square=0;

for i=1:length(pore_info.location)
    if pore_info.radius_voxel(i) >=median(pore_info.radius_voxel)
        pore_info.radius_voxel(i)=1;
    else
        pore_info.radius_voxel(i)=0;
    end
end

for i=1:length(pore_info.location)

    pore_l=i

temp_neighbor=pore_info.neighbor_pores(i,find(pore_info.neighbor_pores(i
,:),>0));
    extra_pores=find(temp_neighbor<i);
    temp_neighbor(extra_pores)=[];
    temp_neighbor=temp_neighbor';
    temp_neighbor_one=[temp_neighbor_one;temp_neighbor];
    temp_number=length(temp_neighbor);
    temp_number_one=[temp_number_one;temp_number];
    left_side=pore_info.radius_voxel(temp_neighbor);
    diff_square=(pore_info.radius_voxel(i)-left_side).^2;
    temp_sum_diff_square=sum(diff_square);
    sum_diff_square=temp_sum_diff_square+sum_diff_square;
    temp_number=length(temp_neighbor);
    number=temp_number+number;

```

```

end

gamma_value(1,1)=(sum_diff_square/(2*number));

%break

while k<lag_number;
    k=k+1;

    sum_diff_square=0;
    number=0;
    local_index=1;

    new_temp_neighbor_one=[];
    new_temp_number_one=[];

    for i=1:length(pore_info.location)

        pore_2=i

        %
temp_neighbor=pore_info.neighbor_pores(i,find(pore_info.neighbor_pores(i
, :)>0));

previous_neighbor=temp_neighbor_one(local_index:sum(temp_number_one(1:i))
);
        temp_neighbor=pore_info.neighbor_pores(previous_neighbor, :);

temp_neighbor=reshape(temp_neighbor,1,size(temp_neighbor,1)*size(temp_neig
bor,2));
        temp_neighbor=temp_neighbor(find(temp_neighbor>0));

        local_index=sum(temp_number_one(1:i))+1;

        for r=1:length(previous_neighbor)

temp_neighbor(:,find(temp_neighbor==previous_neighbor(r)))=0;
end

temp_neighbor(:,find(temp_neighbor==i))=0;
temp_neighbor=sort(temp_neighbor(:,find(temp_neighbor>0)));

        for p=1:length(temp_neighbor)-1
            if temp_neighbor(p)==temp_neighbor(p+1)
                temp_neighbor(p)=0;
            end
        end

        extra_pores=find(temp_neighbor<i);
temp_neighbor(extra_pores)=[];

```

```

new_temp_neighbor_one=[new_temp_neighbor_one;temp_neighbor'];
new_temp_number_one=[new_temp_number_one;length(temp_neighbor)];

left_side=pore_info.radius_voxel(temp_neighbor);
diff_square=(pore_info.radius_voxel(i)-left_side).^2;
temp_sum_diff_square=sum(diff_square);
sum_diff_square=temp_sum_diff_square+sum_diff_square;
temp_number=length(temp_neighbor);
number=temp_number+number;

end
gamma_value(1,k)=(sum_diff_square/(2*number));
lag_pairs(1,k)=number;
temp_neighbor_one=new_temp_neighbor_one;
temp_number_one=new_temp_number_one;

end

gamma_value=[0,gamma_value];
xxx=var(pore_info.radius_voxel);
var_value=zeros(1,length(gamma_value));
var_value(:)=xxx;
plot(0:lag_number,var_value,'r');
hold on
plot(0:lag_number,gamma_value);
axis auto
xlabel('lag (jumps)');
ylabel('semivariogram');

save cor_b_b_krig

%%%%%%%%%%%%%%%%%%%%%%%%%%%%%%%%%%%%%%%%%%%%%%%%%%%%%%%%%%%%%%%%%%%%%%%%
%%
%%  %%
%% end of cor_b_b_krig,m
%%
%%%%%%%%%%%%%%%%%%%%%%%%%%%%%%%%%%%%%%%%%%%%%%%%%%%%%%%%%%%%%%%%%%%%%%%%
%%

```

```

%%%%%%%%%%
%%
%% file name: unif_data.m
%%%%%%%%%%
%%
%%
% this codes asigne a unifrom distribution to the pore sizes:
%%
%% this file folloewd by : cor_b_b_krig.m
%%
load network_info

max_pore=max(max(pore_info.radius_voxel));
min_pore=min(min(pore_info.radius_voxel));
range_pore=min_pore:max_pore;

data_pore=[];

for k=1:length(range_pore)

    original_data=find(pore_info.radius_voxel==k);
    original_data=pore_info.radius_voxel(original_data);
    modified_data=random('Uniform',(min(original_data)-
.5),(.5+max(original_data)),1,length(original_data));
    a_index=find(modified_data<0);
    %modified_data(a_index)=[];
    modified_data(a_index)=abs(modified_data(a_index));

    data_pore=[data_pore,modified_data];
end

pore_info.radius_voxel=data_pore';

save unif_data

%%%%%%%%%%
%
%
%% end of unif_data.m
%
%%%%%%%%%%

%=====
%
% Name of the file cor_b_b_krig.m
%
%%%%%%%%%%
% this code calculates the body-body spatial correaltion (indicator
semivariogram)
%%
%% this file runs after : (1) network_info.m (2) unif_data.m
%%
%
load network_info

```

```

lag_number=10;      %number of lages

pore_info.location=double(pore_info.location);
pore_info.attached_path=double(pore_info.attached_path);
pore_info.radius_voxel=double(pore_info.radius_voxel);

throat_info.location=double(throat_info.location);

load unif_data

gamma_value=zeros(1,lag_number);
lag_piars=zeros(1,lag_number);
k=1;

temp_neighbor_one=[];
temp_number_one=[];
number=0;
sum_diff_square=0;

for i=1:length(pore_info.location)
    if pore_info.radius_voxel(i) >=median(pore_info.radius_voxel)
        pore_info.radius_voxel(i)=1;
    else
        pore_info.radius_voxel(i)=0;
    end
end

for i=1:length(pore_info.location)

    pore_1=i

temp_neighbor=pore_info.neighbor_pores(i,find(pore_info.neighbor_pores(i
,:),>0));
    extra_pores=find(temp_neighbor<i);
    temp_neighbor(extra_pores)=[];
    temp_neighbor=temp_neighbor';
    temp_neighbor_one=[temp_neighbor_one;temp_neighbor];
    temp_number=length(temp_neighbor);
    temp_number_one=[temp_number_one;temp_number];
    left_side=pore_info.radius_voxel(temp_neighbor);
    diff_square=(pore_info.radius_voxel(i)-left_side).^2;
    sum_sum_diff_square=sum(diff_square);
    sum_diff_square=temp_sum_diff_square+sum_diff_square;
    temp_number=length(temp_neighbor);
    number=temp_number+number;

end

gamma_value(1,1)=(sum_diff_square/(2*number));

```

```

%break

while k<lag_number;
    k=k+1;

    sum_diff_square=0;
    number=0;
    local_index=1;

    new_temp_neighbor_one=[];
    new_temp_number_one=[];

    for i=1:length(pore_info.location)

        pore_2=i

        %
temp_neighbor=pore_info.neighbor_pores(i,find(pore_info.neighbor_pores(i
,:),>0));

previous_neighbor=temp_neighbor_one(local_index:sum(temp_number_one(1:i))
);
        temp_neighbor=pore_info.neighbor_pores(previous_neighbor,:);

temp_neighbor=reshape(temp_neighbor,1,size(temp_neighbor,1)*size(temp_neig
bor,2));
        temp_neighbor=temp_neighbor(find(temp_neighbor>0));

        local_index=sum(temp_number_one(1:i))+1;

        for r=1:length(previous_neighbor)

temp_neighbor(:,find(temp_neighbor==previous_neighbor(r)))=0;
end

temp_neighbor(:,find(temp_neighbor==i))=0;
temp_neighbor=sort(temp_neighbor(:,find(temp_neighbor>0)));

for p=1:length(temp_neighbor)-1
    if temp_neighbor(p)==temp_neighbor(p+1)
        temp_neighbor(p)=0;
    end
end

        extra_pores=find(temp_neighbor<i);
temp_neighbor(extra_pores)=[];

        new_temp_neighbor_one=[new_temp_neighbor_one;temp_neighbor'];
        new_temp_number_one=[new_temp_number_one;length(temp_neighbor)];

```

```

    left_side=pore_info.radius_voxel(temp_neighbor);
    diff_square=(pore_info.radius_voxel(i)-left_side).^2;
    temp_sum_diff_square=sum(diff_square);
    sum_diff_square=temp_sum_diff_square+sum_diff_square;
    temp_number=length(temp_neighbor);
    number=temp_number+number;

end
gamma_value(1,k)=(sum_diff_square/(2*number));
lag_pairs(1,k)=number;
temp_neighbor_one=new_temp_neighbor_one;
temp_number_one=new_temp_number_one;

end

gamma_value=[0, gamma_value];
xxx=var(pore_info.radius_voxel);
var_value=zeros(1,length(gamma_value));
var_value(:)=xxx;
plot(0:lag_number,var_value,'r');
hold on
plot(0:lag_number,gamma_value);
axis auto
xlabel('lag (jumps)');
ylabel('semivariogram');

save cor_b_b_krig

%%%%%%%%%%%%%%%%%%%%%%%%%%%%%%%%%%%%%%%%%%%%%%%%%%%%%%%%%%%%%%%%%%%%%%%%
%%
%%  %%
%% end of cor_b_b_krig,m
%%
%%%%%%%%%%%%%%%%%%%%%%%%%%%%%%%%%%%%%%%%%%%%%%%%%%%%%%%%%%%%%%%%%%%%%%%%
%%

```

```

%%%%%%%%%%%%%%%%%%%%%%%%%%%%%%%%%%%%%%%%%%%%%%%%%%%%%%%%%%%%%%%%%%%%%%%%
%%
%% file name: plot_vario.m
%%
%%%%%%%%%%%%%%%%%%%%%%%%%%%%%%%%%%%%%%%%%%%%%%%%%%%%%%%%%%%%%%%%%%%%%%%%

load cor_b_b_krig

var_value(:)=0.25;
x1=0:lag_number;
y1=gamma_value;
y2=zeros(lag_number+1);

median_throat=16.4;

%h11 = line(x1,y1,'Color','b');
%h22=line(x1,var_value,'color','r');

set(gca,'YTick',[0:.05:.35])

plot(x1,y1,'color','b');
hold on
plot(x1,var_value,'color','r');

Xlabel('Lag (jump)')
Ylabel('\gamma(\ith)')
%Title('Lag (micron)');
%break

%ax1 = gca;
break
set(ax1,'XColor','k','YColor','k')

ax2 = axes('Position',get(ax1,'Position'),...
'XAxisLocation','top',...
'YAxisLocation','right',...
'Color','none',...
'XColor','k','YColor','k');

h12 = line(11.5*median_throat*x1,var_value,'Color','k','Parent',ax2);
%h22=line(x1,var_value,'color','r',ax2);

set(ax2,'YTick',[0:.05:.35])

Xlabel('Lag (micron)')

break

xlimits = get(ax1,'XLim');
ylimits = get(ax1,'YLim');
xinc = (xlimits(2)-xlimits(1))/5;
yinc = (ylimits(2)-ylimits(1))/5;

```

Now set the tick mark locations.

```
        set(ax1, 'XTick', [xlims(1):xinc:xlims(2)], ...  
              'YTick', [ylims(1):yinc:ylims(2)])  
break
```

```
%%%%%%%%%%%%%%%%%%%%%%%%%%%%%%%%%%%%%%%%%%%%%%%%%%%%%%%%%%%%%%%%%%%%%%%%  
%%  
%% end of : plot_vario.m  
%%  
%%%%%%%%%%%%%%%%%%%%%%%%%%%%%%%%%%%%%%%%%%%%%%%%%%%%%%%%%%%%%%%%%%%%%%%%
```

## **Vita**

Riyadh Al-Raoush was born on March 1, 1972, in Saudi Arabia. In 1994, he obtained a Bachelor of Science in Civil Engineering degree from Jordan University of Science and Technology, Irbid, Jordan. In 1997, he obtained a Master of Science in Civil Engineering degree from Jordan University of Science and Technology, Irbid, Jordan. He began his Doctoral study at Louisiana State University in August 1998 and successfully completed his degree requirements in December 2002.